# Thèse de Doctorat

*Thèse présentée à l'Université de Mons et l'Université Libre de Bruxelles*
*pour l'obtention du grade de*

## Docteur en Sciences de l'Ingénieur et Technologie

*par*

### Mateo Tunon de Lara

---

## Study and development of femtosecond pulses laser-produced Bragg grating sensors in bulk silica:

### Applications to instrumented compliant mechanisms

**Membres du Jury**

Président:      Prof. B. Scheid, Université Libre de Bruxelles, Belgique

Membres :       Prof. Y. Petit, Université de Bordeaux, France
externes        Prof J. Van Erps, Vrije Universiteit Brussel, Belgique

Membres :       Prof. C. Caucheteur, Université de Mons, Belgique
internes        Dr K. Chah, Université de Mons, Belgique
                Prof. P. Megret, Université de Mons, Belgique
                Prof. P. Lambert, Université Libre de Bruxelles, Belgique
                Prof. C. Collette, Université Libre de Bruxelles, Belgique

### July 2024

# Remerciements

Pour les remerciements, j'ai décidé de les faire dans ma langue maternelle afin de pouvoir m'exprimer du mieux possible et de la meilleure des manières.

J'aimerai tout d'abord remercier Pr. Yannick Petit et Pr. Jürgen Van Erps pour avoir accepté d'examiner mon manuscrit, pour les questions, les commentaires et discussions qui ont permis d'améliorer de manière significative la qualité scientifique de mon travail. J'aimerai également remercier Benoit Scheid, Karima Chah, Patrice Megret et Christophe Collette en tant que membres de mon comité de suivi mais également pour leurs conseils sur la rédaction de la thèse, les présentations ou les démarches scientifiques à réaliser pour le bon avancement du projet.

J'aimerai également remercier Pr. Christophe Caucheteur et Pr. Pierre Lambert pour votre aide durant ces quatre années : votre soutien, vos conseils et votre patience en tant que promoteurs. Je pense que je n'aurai pas pu tomber sur meilleurs promoteurs pendant ces quatres dernières années.

J'aimerai également remercier les créateurs de ChatGPT pour cette intelligence artificielle qui d'un côté est fort inquiétante et de l'autre m'a bien aidé lors de la rédaction de la thèse.

(Dr) Loic Amez-Droz, Dr. Jennifer Watchi, Dr. Vicente Lafarga vous avez été parmi les premiers à m'accueillir au sein du labo beams/tips en plein covid et en pleine période de confinement. Une période difficile pour la sociabilisation et pourtant je pense que c'est cette période qui nous a fait partir ensemble à Valence pour les fallas et j'espère de tout cœur repartir avec vous pour un autre voyage. Loic je te souhaite du courage parce que maintenant ça va être à ton tour de représenter Infuse. Jen je te souhaite beaucoup de bonheur à toi avec Boris dans votre vie et votre rôle de parents de Laslo. Por fin Vicente te deseo lo mejor para tu boda y tu vida con Esther.

Adam, j'aimerai te remercier pour ton aide sur globalement le fonctionnement de la salle blanche, de la Femtoprint ou sur toutes les questions possibles et existantes que j'ai pu te poser. Je ne serai pas aller loin dans la recherche sans ton aide.

Quand on fait une co-tutelle, on est dépendant de deux universités et ça fait deux fois plus de rencontres donc je voudrais aussi remercier tout ceux que j'ai rencontré durant ces quatres dernières années et avec qui j'ai pu échanger qu'il soit dépendant de l'ULB comme Clement, Gilles, Charlotte, Cecile, Jonas, Robin, Jean, Hervé, Manon, Margeaux ou qu'il soit dépendant de l'université de Mons comme Bastien, Hadrien, Fourier, Mederic, Thian bo, Corentin, Maxime, Damien, Marc ou Kevin.

J'aimerai aussi remercier Celine, Laurent, Lucyna et Mariline sans qui je pense je n'aurai pas tenu une année avec les différentes procédures administratives de réinscriptions, congés, congrès et encore la liste est longue.

Parce qu'une thèse de quatre ans, ce n'est pas que des expériences en laboratoire, j'ai aussi eu la chance de faire pleins de rencontres. Ce groupe de personnes avec qui j'ai eu la chance de passer ces quatre années qui m'ont aidé dans les bons et les mauvais moments, j'aimerai les nommer et les remercier.

Mathieu et Morgan, merci d'avoir eu un rôle de grand frère et grande soeur Bruxellois dans ce pays de fou, où le mot chocolatine n'existe pas. Merci aussi pour les moments de discussions sérieuses et foireuses, j'ai toujours pu compter sur vous et ça, ça fait plaisir.

Aurélien, merci pour ces soirées au pot VIE, les soirées Bokit, les soirées jeu twitter et les soirées dégustations de rhum. Bref beaucoup de soirées dont tu vas encore mettre trois jours à te remettre. Mais à côté de ça je te jure que tu es plus qu'un pote de soirée.

Marine, je te remercie pour nos discussions sur les séries de merde qu'on partage, j'ai beaucoup de respect pour toi notamment pour ton travail. J'espère que même si ton avenir est de s'implanter dans le sud tu trouveras toujours le temps de venir à Bruxelles fin novembre. (Merci aussi pour avoir relu les fautes dans les remerciements)

Nathan, je te remercie pour l'appartement rue du couloir, j'ai adoré franchement, mais aussi pour toutes les soirées au C12, y'en a eu qu'une seule mais ressenti vingt. Et si on doit être sérieux merci pour les

Charlotte, je te remercie pour ces discussions autour de Friends et pour les moments où on décidait juste de bitcher gratuitement sur les gens qui avaient trop bu. Je te souhaite beaucoup de courage pour la thèse même si je ne m'inquiète pas trop.

Edouard, je te remercie de m'avoir presenté a tout ce groupe avec qui je passe le plus clair de mes weekend, je tiens aussi a te souhaiter encore une fois beaucoup de bonheur dans ton mariage avec Aélis.

Seba, Julie, vous avez été mes premières rencontres sur Bruxelles. Je sais qu'aujourd'hui on se voit moins qu'à l'époque où on était colloc mais je vous remercie encore de m'avoir initié à l'amour de la bière de qualité, du 421 et du lexique du brusselaire. Brice, Cathy, je vous remercie de m'avoir accompagné dans plusieurs aventures, de m'avoir donné des conseils sur plusieurs choses. Je vous souhaite le meilleur en Suisse.

Maude, je te remercie pour ta ponctualité mais aussi pour tous les échanges qu'ils aient été sérieux ou non, toutes les soirées, et le soutien que tu m'as apporté. Pauline je te remercie pour m'avoir présenté au reste de la fanfare, j'espère pouvoir vite venir te voir à Berlin.

David, le jour où j'ai appris qu'on partageait la même passion des Legos je me suis de suite dit que t'étais quelqu'un de bien. Je te remercie pour avoir eu le courage de te lever tôt à Vienne avec moi pendant que les autres dormaient et je te souhaite du courage pour la fin de la thèse. Achille, je te remercie pour avoir eu la mauvaise idée de me suivre aux premiers entrainements de rugby chaque semaine jusqu'à ce

qu'on finisse par finalement s'inscrire. Je te souhaite aussi du courage pour la fin de la thèse.

Certains d'entres vous ne m'ont connu que en tant que doctorant mais il y a une personne qui me connait depuis bien longtemps. La première année d'étude supérieure (Bachelier première pour mes amis bruxellois) en 2015/2016 et qui très vite m'avait dit « Non mais c'est sur tu vas faire un doctorat » : Mr Hicham Mdarhri, on est en 2024 et presque 9 ans après notre rencontre tu avais bel et bien raison, j'ai fait un doctorat et sans toi et tous les lillois ça n'aurai pas été pareil donc merci à vous Cindy, Estelle, Julia, Adrian, Imade, Jo, Magloire et Nico.

J'aimerais aussi remercier mes amies chimistes avec qui j'ai réussi à garder une bonne relation malgré le temps et les différents parcours. Rim, même si Dubaï c'est très loin, on va pas se mentir, chacune de tes arrivées en Europe fait énormément plaisir et me redonne le sourire. Dr. Lily, maintenant que tu vas arriver dans la capitale bruxelloise, j'ai hâte de te voir plus souvent pour discuter et passer plus de temps ensemble. Juliette, toi qui as fait le choix de rester à Paris (grosse erreur selon moi), je viendrai quand même te rendre visite et sinon on se retrouvera aux anniversaires de notre cher chamou. J'aimerais vous remercier pour votre soutien qui a été différent mais tout aussi important.

J'aimerai aussi remercier des amis de longues dates, personnes que je connais maintenant depuis le lycée. Marie-lou, je te remercie pour ton écoute et ta patience sur des sujets pas toujours joyeux. Aurelia, je te remercie pour ton enthousiasme même si tu m'en veux qu'on ne se voit pas autant qu'avant. Flavie, je te remercie pour notre amitié aujourd'hui qui est importante à mes yeux. Oriane, je te remercie pour être venu à Brxeulles à plusieurs reprises même si ta venue la plus mémorable restera la première. Sofia, je te remercie pour ton soutien même si on n'a pas forcément beaucoup interagi ensemble ces dernières années. Loic, Quentin et Bastien j'aimerai vous remercier pour votre soutien, les soirées faites ensemble et par la même occasion je voudrais vous souhaiter bonne chance parce que vous allez pas tarder à être à ma place pour défendre votre recherche.

J'aimerai aussi remercier mes senseis Loic, Mickael, Alain, Sam et les autres membres du Dojo Bordeaux, Judo club Talence et du Royal Poseidon, qui même si je pense n'ont pas toujours compris comment se déroulait un doctorat me demandaient et prenaient des nouvelles à chaque entrainement. J'en profite au passage pour remercier la K3 du Kituro qui a bien dynamisé ma dernière année de thèse et avec qui en un an j'ai déjà passé de très bons moments. Merci à vous.

J'aimerai aussi remercier ma grand-mère, mes oncles, tantes, cousins, cousines mais plus particulièrement mes sœurs Nina et Sara dont je me suis toujours inspiré pour leurs parcours académiques et dont toutes les personnes cités précédemment dans ces remerciments ont entendu parler au moins une fois. Je vous remercierai jamais assez pour la relation d'adelphie que nous avons, qui a toujours été forte, j'ai aucune idée de ce que l'avenir me réserve mais je sais que je pourrais toujours compter sur vous. J'aimerai aussi remercier Théo, qui a integré officiellement la famille Tunon il y a 3 ans mais officieusement depuis bien plus longtemps, merci pour tes conseils en tant

que kiné et également merci du soutien que toi et sara m'avez apporté. J'en profite aussi pour remercier et souhaiter la bienvenue a ma future nièce, qui va rendre ses parents très heureux j'en suis sûr.

Enfin, j'aimerai remercier mes parents qui m'ont toujours encouragé tout au long de la thèse, qui ont lu un certain nombre de fois une thèse dans un domaine qui n'est pas le leur et ont pourtant toujours réussi à faire des critiques importantes. J'aimerai aussi les remercier pour leurs conseils, leur soutien et leur aide durant toutes les années d'études supérieures. Vous avez toujours été de très bons conseils, vous avez toujours su me calmer dans les moments où j'étais stessé pour des raisons qui n'étaient pas valables et ça depuis longtemps.

ii

# Abstract

This PhD thesis, conducted in co-tutelle between the Université de Mons and the Université Libre de Bruxelles in Belgium has focused on the study and development of waveguides and Bragg gratings in pure silica planar substrates entirely relying on a femtosecond pulses laser process. The inception of femtosecond laser pulses dates back to 1985 when Gerard Mourou and his team first observed their interactions with fibres. Since then, femtosecond lasers have emerged as a pivotal technology due to their unique precision, resolution, and capability to directly alter surfaces for creating micro-structures or optical configurations. The considerable advancements obtained in this ever growing field over the past decades has led to the development of a commercial device known as the Femtoprint machine, which integrates a femtosecond pulses laser focused through a microscope objective, a 3D axis moving plate boasting high resolution in the positioning and a computer-aided design software that drives the whole system.

Through refined studies and analyses in an optimization process, we have investigated the impacts of different parameters (pulse energy, repetition rate, writing speed, polarization ) of the Femtoprint process on the quality of engineered structures. Our primary research objective was to fabricate an optical waveguide encompassing a uniform Bragg grating within a flexible structure entirely engineered in a fused silica glass substrate. We had also to fabricate an optimized cavity to enable a good optical connexion between the femtosecond pulses laser-engineered waveguide and a connecting single-mode optical fibre. To achieve this, we conducted a thorough examination of all available parameters and assessed their suitability for the desired surface modifications. For quality characterization purposes, we employed methodologies including Digital Holographic Microscope (DHM) analysis, polarization-based amplitude spectral measurements and infrared camera imaging.

The in-built Bragg gratings were then characterized for sensing purposes. The impact of a temperature change from room temperature to 140 °C was first investigated. Then, mechanical characterizations were performed. Experimental set-ups have been progressively built and optimized to apply controlled axial strain, 3-point bending and flexure (cantilever beam) on the produced sensing platforms. Experimental sensitivities were determined in each case, with a good adequation with the expected values from the literature review. Some gratings were also produced close to the edge of the substrate, with the ambition to measure changes in the surrounding refractive index value.

This work opens doors for the advancement of sophisticated instrumentation, not only in fields like photonics and optomechanics but also in domains such as biomedical engineering and environmental monitoring. Furthermore, beyond their sensing capabilities, these monolithic structures showcase exceptional mechanical, thermal, and optical properties intrinsic to fused silica glass. This distinctive properties put them as optimal candidates for diverse applications, including precision instrumentation in demanding environments. Their capability to endure harsh conditions with high sensitivity and accuracy renders them interesting instruments for the future.

# Contents

# Chapter 1

# General Introduction

The current doctoral dissertation stands as a contribution to the Infuse project, a collaborative research programme engaging the intellectual resources of the University of Mons (UMONS), Université Libre de Bruxelles (ULB), and the University of Liege (UL). Guided by the expertise of my advisors, Christophe Caucheteur and Pierre Lambert, this research undertaking received recognition and financial support from the Belgian National Fund for Scientific Research (F.R.S.-FNRS). Launched in September 2020, this four-year initiative is committed to advancing cutting-edge sensor technologies by exploring optical responses within silica glass. With this introduction, we aim to carefully incorporate the story of the scientific setting at the start of this Ph.D.

## Context and Motivations

In the year 2020, at the inception of the Infuse project, ultra-short laser pulses, notably femtosecond pulses, are a key technology. This cutting-edge technology found diverse applications, ranging from its role as a precision tool in LASIK surgery [1, 2], consisting in modifying the retina of the eye for myopic individuals, to its utility in the realm of spectroscopic science [3]. Notably, the significance of ultra-short laser pulses was underscored by the awarding of the Nobel Prize in Physics in 2018 to Gérard Mourou for his pioneering work on chirped pulse amplification. Furthermore, the latest reward upon physicist Anne Huillier in 2023 for her groundbreaking contributions to attosecond laser research solidifies the ongoing dynamic nature of advancements in ultra-short laser pulses. These examples highlight the impact of femtosecond technology, not only in shaping the trajectory of scientific research but also in recognition at the highest echelons of the scientific community. In the global scientific context, the last decade has established ultra-short laser pulses as a new source of innovation, constantly pushing the boundaries of what is achievable in the realms of both fundamental research and applied technologies.

In the context of our research, the femtosecond laser assumes a role directed towards its capabilities to modify the properties of silica glass. Facilitating this goal we choose to use the Femtoprint machine, a sophisticated machine revealed by Yves

Bellouard in 2012 [4]. This system hosts a three-axis platform and is equipped with a femtosecond laser pulse source. The Femtoprint machine constitutes an automated tool, capable of offering several possibilities thanks to the high flexibility of the inscription parameters. This makes it possible to go from a simple increase in the refractive index to complex mechanical modifications. Throughout this thesis, we have produced a mix of simple components and complex systems thanks to mastery and a good balance of the different parameters. The examination and exposition of the processes, and their associated modifications, will be recurrent themes in this manuscript.

## Objective of the Work

In the course of our research, we have defined a series of objectives aimed at the realization of a strain sensor model entirely constructed from silica glass. First is the creation of a cutting-edge sensor, crafted through the precision of femtosecond laser printing technology. Our primary aim is to engineer a sensor capable of receiving optical inputs but also transmitting them efficiently, minimising signal loss.

This sensor will be completely created from a silica glass plate and it will then be manufactured with the femtosecond laser. The prototype is envisioned to encompass several optical modifications with an optical waveguide and a Bragg grating. This strategic addition serves a dual purpose: to characterise the sensor's optical response and to monitor signal evolution in response to fluctuations in its ambient environment. The integration of an optical Bragg grating represents an important step towards enhancing the sensor's functionality and adaptability.

In an ideal scenario, the sensors emerging from our research will not be confined by rigidity but rather showcase remarkable flexibility on multiple levels. This flexibility encompasses adaptability to diverse conditions and environments. The outcome of our efforts would be the creation of a silica glass-based sensor. It aspires to establish a multifaceted platform that exemplifies adaptability, sensitivity, and versatility in the face of varying environmental stimuli. The exploration and interpretation of these inherent sensitivities will emerge as a central theme in our investigation, unravelling profound insights into the efficacy and diverse potential applications of our pioneering sensor technology.

## Contributions

The femtosecond technology has witnessed large documentation over the past decade [5], especially in the realm of optical impacts and applications. The domain of mechanical deformation and flexible structures has undergone significant advancements. However, the contribution brought by the Femtoprint system lies in its precision and the liberty that we have for the creation of the optical waveguide and the mechanical structures.

This convergence of optical and mechanical functionalities represents an opportunity, offering the prospect of measuring mechanical deformation through optical responses. The ability to add these aspects within a single structure in a single operation paves the way for a new era in sensor design and fabrication.

To achieve this, we will begin with a silica glass plate of high purity (99.9998-99.99995 %). From this structure, we will first create cavities integrated into the substrate to host a standard optical fibre. Subsequently, we aim to construct an optical waveguide at the input of these cavities and along the substrate. Then, we will create a Bragg grating within this optical waveguide. The advantage of the Bragg grating structure is that it will reflect a signal that can be observed through an optical spectrum analyser. Once we have the entire optical structure and a functioning waveguide, we will be able to conduct an optical characterisation of the waveguide to determine its sensing response to temperature or mechanical deformations.

The creation of such integrated structures is suitable for measuring mechanical deformation through optical measurements but also paves the way towards constructing more intricate sensor architectures. This capability becomes a foundation, allowing the development of increasingly complex structures with finer resolutions. As we navigate this technological frontier, the prospect of achieving structures with enhanced resolution becomes conceivable, thereby unlocking the potential for detecting and quantifying minute modifications with unprecedented precision. In essence, the Femtoprint system not only represents a technological innovation but also a gateway to a realm where the fusion of optical and mechanical functionalities takes place. It propels the development of sophisticated sensor technologies, marking a notable leap forward in the landscape of structural and optical engineering. This thesis aims to address several critical questions regarding the quality and potential for innovation of this technology.

- Can we successfully inscribe a Bragg grating and an optical waveguide into a silica glass plate?

- Are we able to accurately characterise the sensitivity of the Bragg grating to its surrounding environment, particularly the effects of temperature and mechanical flexure on the overall structure?

- Can we identify and leverage this characterisation for future sensor applications?

## Structure of the Thesis

The remaining of the thesis manuscript is organized into 5 different chapters. The 2$^{nd}$ chapter, "Theoretical Background.", intends to provide a comprehensive overview of key concepts essential for a global understanding of the PhD manuscript. This includes the mechanisms underlying the impact of femtosecond laser pulses on the surface of bulk silica glass, the principles of Bragg Grating and the fundamental principles of the propagation of light through different media.

Next within the "State of the Art" chapter, we aim to provide a broader context by exploring the applications of femtosecond laser technology in other domains, elucidating the circumstances under which it is employed. This chapter is organized to provide a comprehensive exploration of the obtained results and their implications.

Chapter 4 is dedicated to the development and evolution of the structure housing the fibre, specifically focusing on the insertion of optical fibre in a cavity into the silica glass. It unravels the shaping of the physical foundation of the sensor, offering insights into the structural modifications and innovations that contribute to the efficiency of the system. It also presents a detailed examination of the optical outcomes derived from the sensor technology. This section encompasses the characterisation of optical responses, the methodologies employed in the inscription, and the various considerations and limitations inherent in the optical processes. This chapter aims to provide a comprehensive understanding of the optical facets of the developed sensor.

Chapter 5 focuses on the global characterisation of how the environment influences the optical signal. This encompasses an exploration of the impact of environmental variables, such as temperature or flexibility of the sensor structure. By studying the interaction between the sensor and its surroundings, this chapter offers a global understanding of the sensor's functionality in diverse conditions.

Chapter 6 serves as a conclusion, where we aim to address various scientific questions and summarize the different scientific achievements and future perspectives for our technology. This chapter will be followed by the literature references and appendices containing additional results.

If we were to summarize the Infuse project, it could be through the following application: the construction of instrumented flexible structures and instrumented surfaces within silica glass. To achieve these objectives, we need to fabricate optical inscriptions in a planar glass substrate. These inscriptions will include a fibre insertion interface, a waveguide, and a Bragg grating. Then, we will need to characterise the flexibility of the glass, the quality of the optical inscriptions, and the sensitivity of the Bragg grating to its surrounding environment. Once these steps are completed, we can consider potential mechanical or chemical applications. The various steps of the project are summarized in Figure 1.1.

**Objective**
Instrumented Flexible
Glass Structure

Surface Instrumented
Glass Sensors

**Fabrication**
Optical inscription in glass substrate
- Fibre insertion interface
- Waveguide inscription
- Bragg grating inscription

**Characterization**

Glass Flexure
Characterization
- Tensile Strength
- Bending Stength

BG Sensor Characterization
Temperature induced strain
Mechanical induced strain
- Pure tensile strain
- Pure bending strain
Chemical induced phenomenon

Optical Inscription
Characterization
Waveguide Light Transmission
Bragg grating
- Reflection
- Transmission

**Application**
Mechanical application
- Force sensor
- Inertial sensor

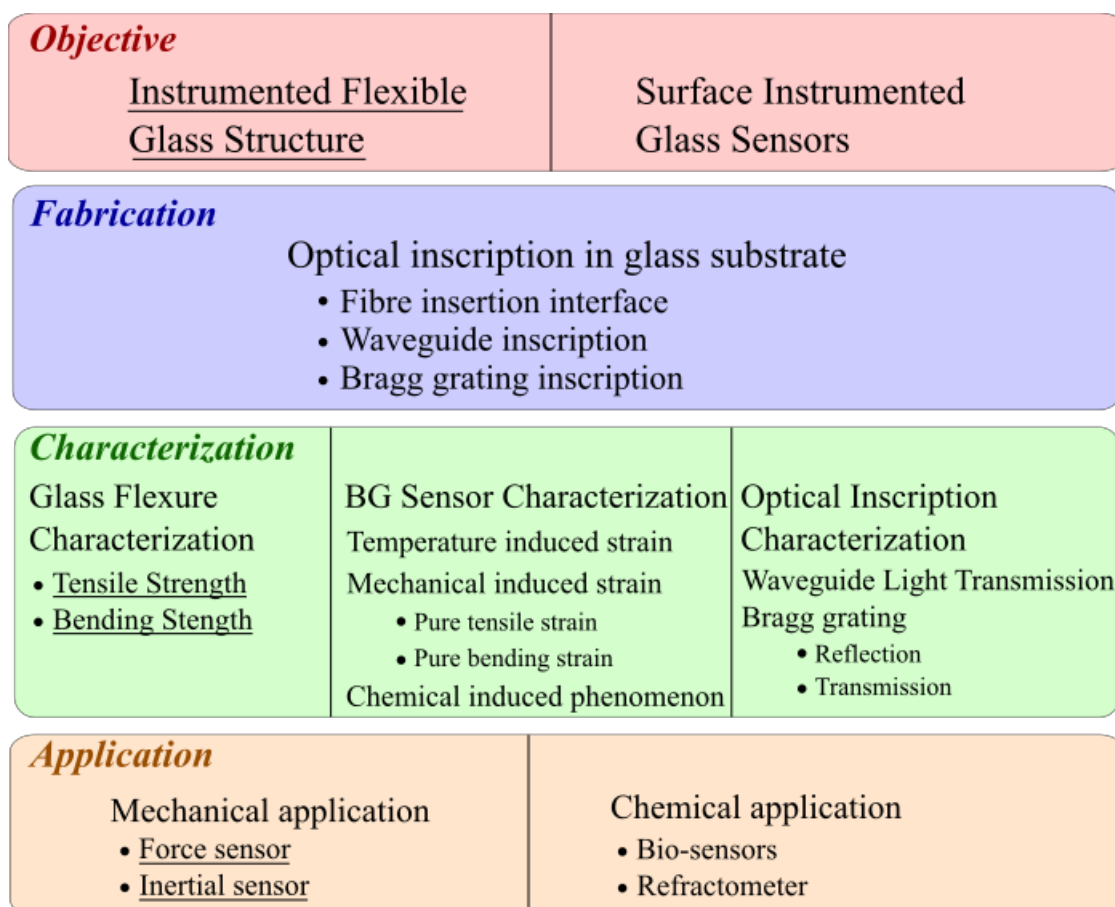Chemical application
- Bio-sensors
- Refractometer

Figure 1.1: Scheme summarizing the different objectives of the Infuse project. It is important to take into account that the underline part has been realised by the other worker of the PhD project.

# Chapter 2

# Theoretical Background

In this chapter, the objective is to cover fundamental concepts such as the basics of optics, including optical fibres and reflection angles. Next, we will explain in section 2 the principles of the induced modifications in silica glass by femtosecond laser pulses and their use to create an optical waveguide, there are other type of glass described in Appendix A. In section 3, our attention will shift to Bragg gratings and their operation principles, followed by a few examples of application types and the corresponding expected responses in section 4.

## 2.1 Optical Fibres

Optical fibres [6] technology, first patented in 1967 [7], is a well-established technology and widely used means of transmitting information and power using light beams. These optical fibre cables are known for their thin diameter and flexibility, their low loss enabling efficient data transmission over long distances with minimal signal and power degradation. As a result, internet service providers, cable TV companies [8], and telecommunications [9] carriers worldwide rely on optical fibre as the infrastructure for high-speed connectivity. Additionally, various industrial sectors depend on optical fibre for diverse applications, including monitoring [10] and data transfer. In summary, optical fibre technology has profoundly transformed our communication methods, and its ongoing development and adaptability continue to play a fundamental role in our increasingly interconnected world.

### 2.1.1 Characteristics of Optical Fibres

An optical fibre is a cylindrical cable typically made of fused silica glass, which is thin (250 µm for standard optical fibre) and flexible. It consists of several layers with different refractive indices. These parts are usually referred to as the core, the cladding, and the coating. They are illustrated in Figure 2.1 for a single-mode optical fibre. The multimode fibre is usually composed of the same layers, but the thickness of the layers is different (the core diameter is bigger)[11]. There are several types of fibres, including step-index fibres and graded index fibres. In this context,

we will focus on describing a single-mode-step-index fibre, as the most commonly used, because of its superior bandwidth, longer transmission distances, better signal quality, compatibility with advanced technologies, and potentially lower long-term costs.
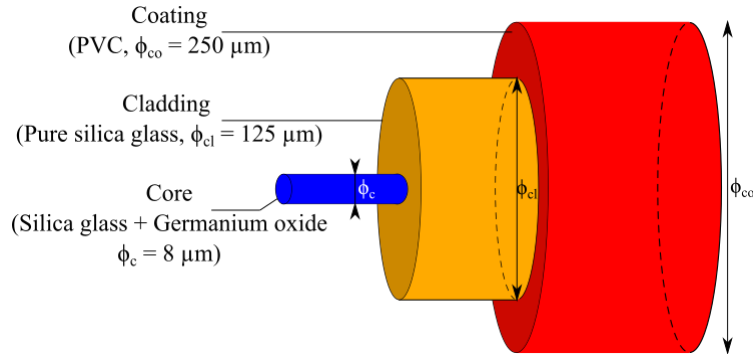


Figure 2.1: Isometrical scheme of an optical fibre and its different parts.

As the central section of the fibre the core is responsible for transmitting light signals. It is usually made out of silica ($SiO_2$) doped with germanium oxide to increase the refractive index. Surrounding the core is a layer of glass known as the cladding, made out of pure silica, which maintains the light signal within the core by reflecting it as its interfaces with the core. Lastly, the outermost layer, referred to as the coating, provides mechanical and chemical protection against external forces or agents that could potentially damage the fibre. It is usually made out of Polyvinyl Chloride (PVC). It is crucial to understand that the core and cladding of an optical fibre interact with light through well-established mechanisms and optical laws summarized hereafter.

## 2.1.2   Light Propagation in Optical Fibres

Snell's Law [12], also known as the law of refraction, describes the relationship between the reflection angle ($\theta_r$), the refraction angle ($\theta_2$) and the refractive index of the medium. When light passes from one medium to another, with a different refractive index, it separates into a reflected part and a refracted part. A schematic version of Snell's law is represented in Figure 2.2.
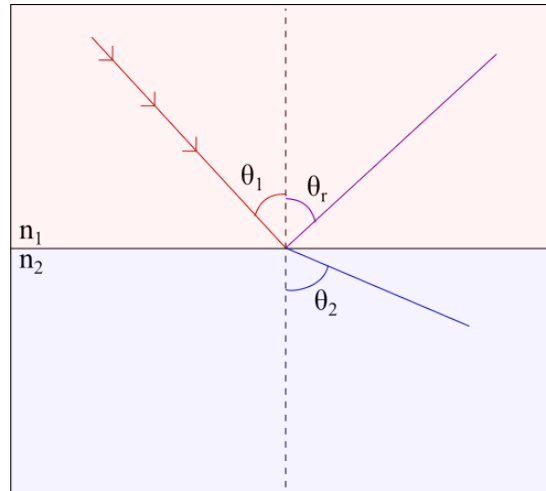
Figure 2.2: Geometrical representation of Snell's Law. $(n_1 > n_2)$

Snell's Law provides a way to calculate the angle of refraction, based on the refractive index of the two media.

$$\theta_1 = \theta_r \tag{2.1}$$

$$n_1 \sin \theta_1 = n_2 \sin \theta_2 \tag{2.2}$$

Snell's Law offers special cases that can be leveraged to direct light in distinct ways. One such case involves the critical angle. At a specific angle of incidence, named critical angle, the refracted ray cannot penetrate the second medium and instead travels at the interface between the two mediums and then light can not penetrate the second medium [13]. Above this critical angle value, the light is in a situation of total internal reflection. Taking into account the differences between the refractive index and the incident angle, light can simply be reflected at the surface between the two different media, both cases are explained in Figure 2.3. In the case of the total reflection $\theta_2 = \frac{\pi}{2}$. If we apply this to equation 2.2, we get the following:

$$n_1 \sin \theta_1 = n_2 \tag{2.3}$$

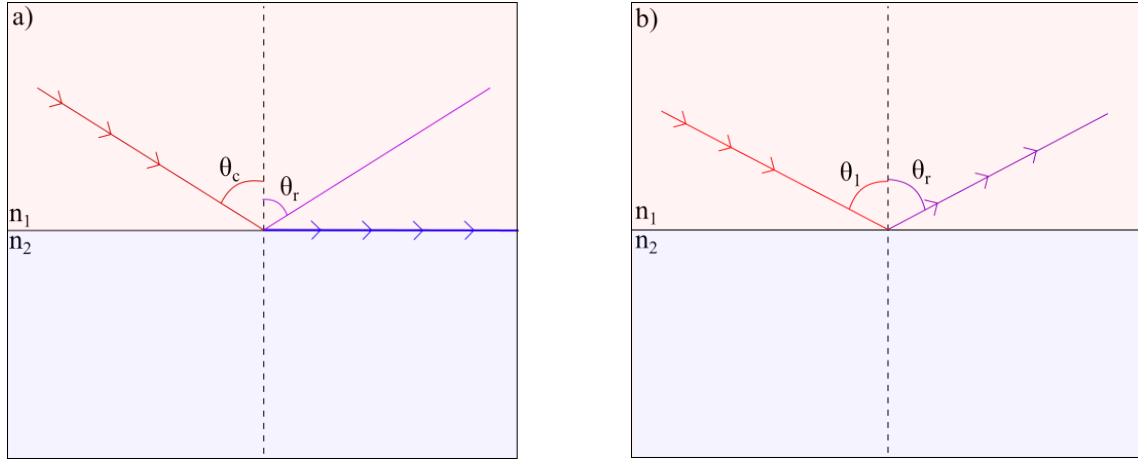$$\sin \theta_c = \frac{n_2}{n_1} \tag{2.4}$$

Figure 2.3: (**a**) Scheme representing the path of the light in the case where $\theta_1 = \theta_c$. (**b**) Scheme representing the path of the light in the case where $\theta_1 > \theta_c$.

This total internal reflection allows the light signal to travel long distances through the fibre with minimal loss of signal strength. For the optical fibre, the reason for the total reflection is due to the difference in refractive index as the refractive of the core is higher to the one of the cladding ($n_{core} > n_{cladding}$). It is linked to the chemical composition of the cladding and the core. We understand why the cladding of the optical fibre is made out of pure silica glass whereas the core is doped with germanium oxide [14].

An optical mode is a specific solution to Maxwell's equations [15], which describes the behaviour of light in a given medium. These solutions describe the various ways in which light can propagate in this medium. Each optical mode corresponds to a specific configuration of the electric and magnetic fields that determine the direction, polarization, and spatial distribution of light. In an optical fibre, for example, optical modes determine how light propagates inside the fibre. There are several possible optical modes, each corresponding to a different trajectory inside the fibre. In optical fibres, propagation modes can be described geometrically by the angles of incidence of light rays or wave-wise by solutions to Maxwell's equations, with each mode corresponding to a specific electromagnetic field distribution. There is a correspondence between these descriptions: the discretization of incidence angles matches the quantization of modes. When an optical fibre guides a single mode, it means there is only one permissible angle and one wave solution, typical of single-mode fibres, which reduces dispersion and maintains signal coherence. Optical modes can also have different properties in terms of polarization, propagation speed, and dispersion. These modes are referred to as characteristic waves of the structure because they satisfy the homogeneous wave equation. The wave equation in the three spatial dimensions is given by the following equation [16].

$$\frac{\partial u^2}{\partial t^2} = c^2 \left( \frac{\partial u^2}{\partial x^2} + \frac{\partial u^2}{\partial y^2} + \frac{\partial u^2}{\partial z^2} \right) \tag{2.5}$$

Each mode is characterised by an invariant transversal identity and an effective index. The propagation speed of each mode is determined by the speed of light divided by the effective index. Guided modes are waves that are reflected back and forth between the two interfaces. They can only exist when a transverse resonance condition is satisfied. The dimensions of the waveguide determine which modes can exist, and most waveguides support modes of two independent polarizations with a dominant magnetic or electric field.

The type of fibre is also significantly influenced by its Numerical Aperture (NA) and the V-Value. The V-value, also known as the normalized frequency, is determined by the equation involving the numerical aperture, wavelength, and core radius. Therefore, we can infer that for V-Values less than 2.405, the waveguide will be single-mode, while for V-Values greater than 2.405, the waveguide will be multimode. NA is a measure of the light-gathering ability of an optical system, such as a microscope objective lens or an optical fibre [17]. The numerical aperture is described in equations 2.6 and 2.7. Here, $d$ is the diameter of the lens, $f$ is the focal length and $\alpha$ is the angle of the cone.

$$NA = n \times \sin(\alpha) \tag{2.6}$$

In the current situation, we are working in the air so the refractive index is $n = 1$.

$$NA = \sin(\alpha) = \frac{d}{2f} \tag{2.7}$$

It describes the cone angle of light that can be collected by the optical system and determines the resolution and depth of field of the system.

Both single-mode and multimode fibres can be used for several applications, however, they can be subject to the phenomenon of birefringence.
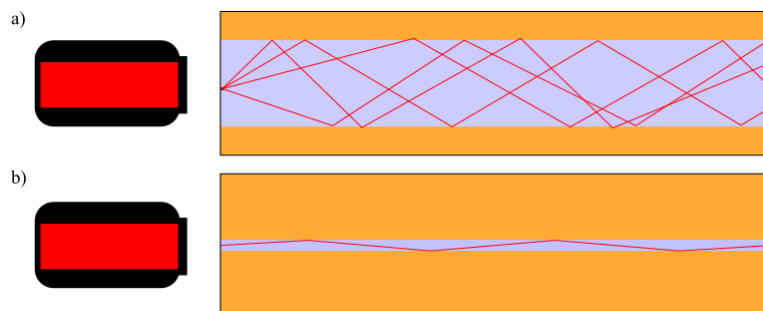


Figure 2.4: Schematic representation of the different types of fibres and the different paths of the light. **(a)** Scheme of a multimode step index fibre. **(b)** Scheme of a single mode optical fibre. The primary distinction between the two fibres lies in the core size, which subsequently leads to the generation of multiple modes.

### 2.1.3 Birefringence in Optical Fibre Systems

In an ideal single-mode fibre (SMF), we expect the propagation of two degenerate modes with orthogonal polarizations, which is only respected when the optical fibre has perfect circular symmetry. However, in practice, real optical fibres are never perfectly circular; they often exhibit small asymmetries, causing the core to be slightly elliptical. Additionally, internal stresses due to the manufacturing processes or non-homogeneous dopants can lead to differences in the refractive index for orthogonal polarization states, known as eigenmodes. This phenomenon is referred to as birefringence and describes how light propagates along the material. In a situation of birefringence, we have two different effective refractive indices along the two main axes, called the slow (y) and fast (x) axes. The effect of the birefrigence can be quantified thanks to equation 2.8.

$$\beta_{C_{xy}} = \beta_{C_y} - \beta_{C_x} = \frac{2\pi}{\lambda}(n_{\text{eff}_x} - n_{\text{eff}_y}) = \frac{\omega}{c}\Delta n \qquad (2.8)$$

Here $\lambda$ is the wavelength, $n_{\text{eff}_x}$, and $n_{\text{eff}_y}$ are the effective refractive indices of the fast and slow eigenmodes, $\omega$ is the angular frequency and c is the speed of light in the vacuum, $\Delta n$ is the refractive index difference. Uniform birefringence can be classified into two distinct types: linear birefringence and circular birefringence. Linear birefringence is characterised by linearly polarized eigenmodes, with the difference between these modes per unit length, known as linear birefringence ($\delta$), expressed in rad/m [18]. The orientation of the eigenmode is determined by the parameter $\theta$, which represents the azimuth of the fast polarization mode. On the other hand, circular birefringence involves circularly polarized eigenmodes, with one mode rotating clockwise and the other anti-clockwise. The difference between these modes arises from their respective speeds, and the circular birefringence is defined as $2\rho$. In the most general scenario, both linear and circular birefringences are simultaneously present, resulting in elliptically polarized eigenmodes.

Birefringence can be induced through different ways, quantified by the shift of polarization. The smallest birefringence is intrinsic birefringence that result from the creation of the substrate. It is characterised with a refractive index difference $\Delta n$ of the order of $10^{-7}$ typically for optical fibre. The next type is photo-induced birefringence, with a refractive index difference of about $\Delta n = 10^{-6} - 10^{-5}$. Mechanical birefringence is considered as a high birefringence level, inducing a refractive index difference of $10^{-4}$.

## 2.2 Bragg grating

### 2.2.1 Introduction to Bragg Gratings

A Bragg grating [19] is a spatial periodic modification of the refractive index along a waveguide. The Bragg grating reflects selectively wavelengths of light ($\lambda_{BG}$) while transmitting others, based on the principle of Bragg Law [20]. Bragg's law is a fundamental law of physics that describes the reflection of waves, such as light

waves or sound waves, from a crystalline lattice. It is named after the British physicists William Henry Bragg and William Lawrence Bragg who formulated it in 1913. Bragg's law states that when waves are reflected by a crystalline lattice, the difference in optical path length between two consecutive reflected rays is equal to an integer multiple of the wavelength of the incident wave. It is described in Figure 2.5.



$$n\lambda = d \, (\sin\theta'_1 + \sin\theta'_2)$$

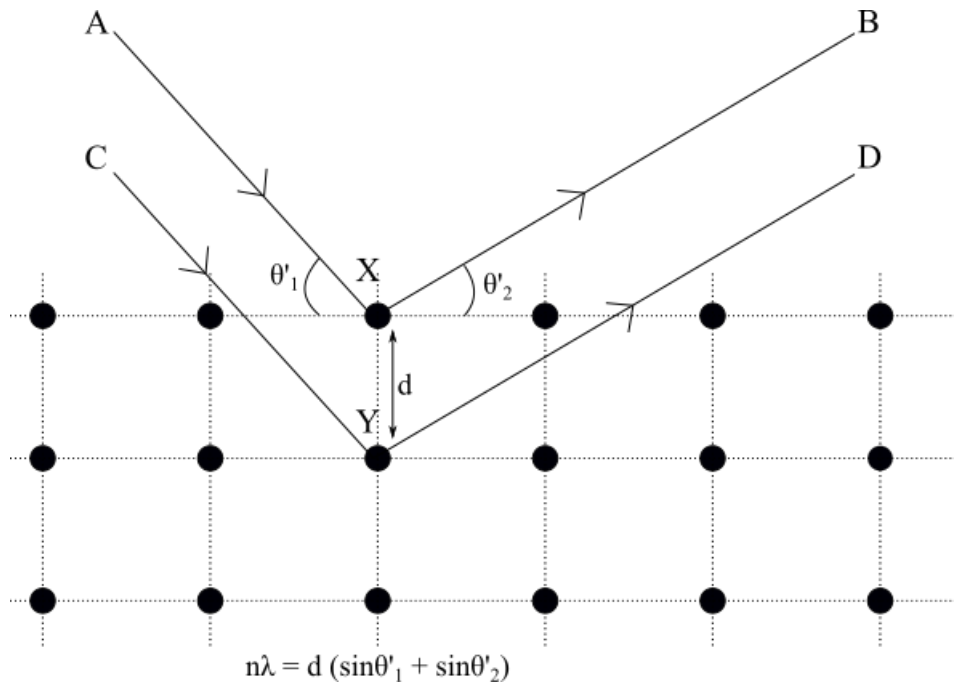Figure 2.5: Schematic representation of the Bragg Law.

When light propagates through a Bragg grating, it is scattered and reflected due to constructive interference between the waves that are diffracted by the grating. The wavelength of the reflected light is determined by the period of the refractive index modulations and the refractive index of the surrounding material (in the case of an optical fibre, the core).
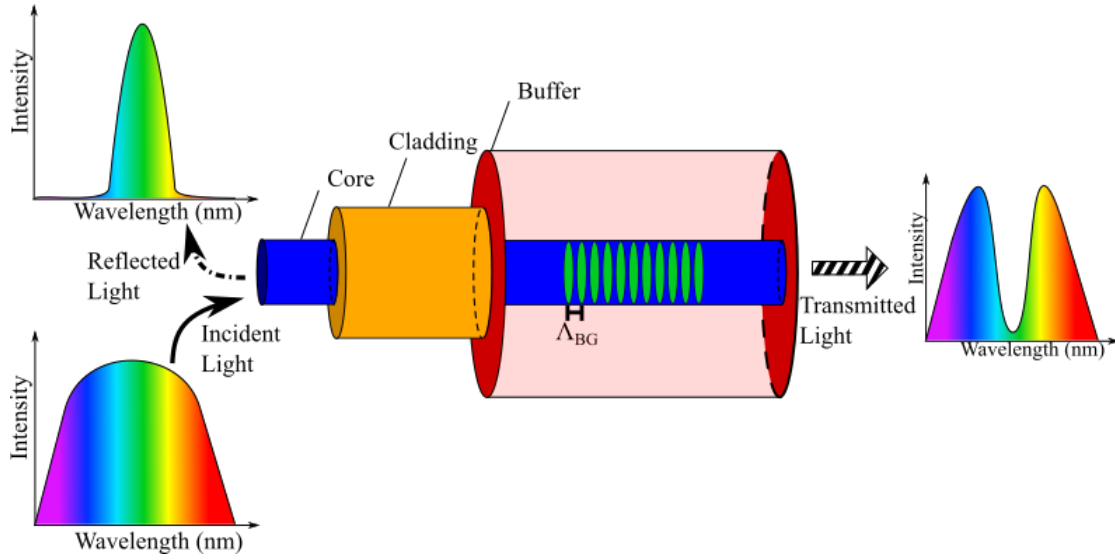
Figure 2.6: Scheme of a Bragg grating in optical fibre and the resulting spectrum both in reflection and transmission.

As a function of the period chosen, several orders (labelled with m =1,..., N) are possible. This equation can be used to predict the reflected Bragg wavelength [21]:

$$m\lambda_{\mathrm{BG}} = 2n_{\mathrm{eff}}\Lambda \tag{2.9}$$

Here $m$ is the order of the Bragg grating, $\Lambda$ is the period of the modification, $\lambda_{BG}$ is the wavelength of the Bragg grating and $n_r$ is the refractive index of the core. Basically fiber grating is an optical diffraction grating [22]. As sketched in Fig. 2.7 (a), for a light wave incident on the grating at an angle $\theta_1$ will diffract in several directions called diffraction orders. This phenomena is described by the well-known grating equation 2.10.

$$n \times sin(\theta_2) = sin(\theta_1) + m\frac{\lambda}{\Lambda} \tag{2.10}$$

In this equation, $\theta_2$ represents the angle of the diffracted wave, and the integer $m$ indicates the diffraction order. For a given wavelength and incidence ($\theta_1$) of a light beam, this equation allows to determine the directions $\theta_2$ into which constructive interference occurs. In the case of an optical fiber it allows to calculate the wavelengths at which a fibre grating most efficiently couples light between two modes. In Fiber Bragg gratings coupling occurs between modes traveling in opposite directions as shown in 2.7 (b). In this case $\theta_2 = -\theta_1$. Equation 2.10 becomes Equation 2.9 where $n_{\mathrm{eff}} = n \sin(\theta)$ is the effective refractive index of the mode.
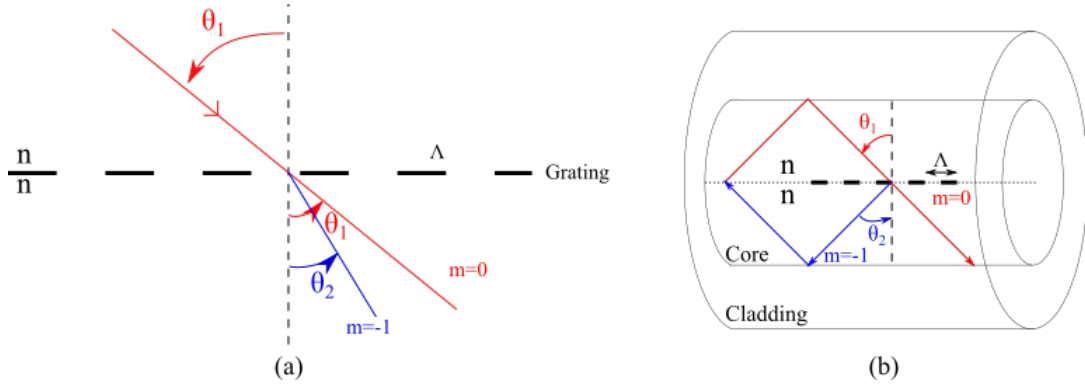
Figure 2.7: Schematic illustration of (a) the light diffraction by a grating in a medium of n refractive index (b) the core mode an optical fiber back reflected by the fiber Bragg grating.

This first aspect is important because it gives us an idea of where the Bragg wavelength is located. The next aspect is to simulate the shape of the Bragg spectrum. To do so we will apply the couple mode theory which is widely used in the design of optical devices, especially Bragg gratings [23]. This theory is based on the principle of coupling between different propagation modes of an electromagnetic wave in a periodic or non-periodic optical structure. In the context of Bragg gratings, the coupled mode theory describes how light propagates through a periodic refractive index variation. To optimize the efficiency of this simulation, it is imperative to take into account various parameters. Some of these parameters can be directly inserted from experimental data, and from the different studies we can simulate the shape of a Bragg grating [24]. These parameters encompass the wavevector detuning ($\delta$), linked to the detuning factor ($\sigma$), and the propagation constant of the fibre core ($\beta$). The wavevector detuning refers to the difference between the actual wavevector of a light wave and the expected or ideal wavevector in a given optical system. The detuning factor describes the difference between the actual frequency of the light wave and the system's resonance frequency, with both concepts being interconnected as they influence the resonance and interference patterns in optical systems.

$$\delta = \beta - \frac{\pi}{\Lambda_{\text{BG}}} = \frac{2\pi n_{\text{eff}}}{\lambda} - \frac{\pi}{\Lambda_{\text{BG}}} = \frac{2\pi}{\lambda}(n_{\text{eff}} - \frac{\lambda}{2\Lambda_{\text{BG}}}) \tag{2.11}$$

$$\sigma = \frac{2\pi}{\lambda}\delta n \tag{2.12}$$

Here, $\delta$n is the biggest refractive index variation possible that we fix at $1 \times 10^{-4}$, $\Lambda_{BG}$ represents the periodicity of the Bragg grating, $\sigma$ denotes the detuning factor, the modelling approach is grounded in the application of coupled-mode theory for the analysis of optical Bragg grating behaviour. Within this framework the Bragg grating structure is inducing an alteration in the effective refractive index it also represent the constant average contribution ($\Delta n_{\text{AC}}$) and the modulated index variation contribution ($\Delta n_{\text{DC}}$).
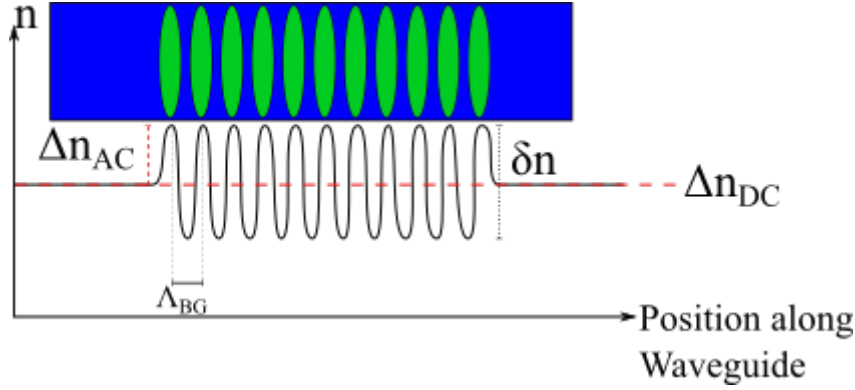
Figure 2.8: Representation of the evolution of the refractive index induced by the Bragg grating along the waveguide.

Through a comprehensive examination of this perturbation, we can ascertain the coupling coefficients of both forward and backward-propagating modes within the Bragg grating. More precisely, the coupling coefficient associated with the forward-propagating mode is commonly designated as the "ac" coupling coefficient, while the coupling coefficient governing the general "dc" coupling is symbolically represented as $\hat{\sigma}$.

$$\hat{\sigma}^2 = \delta + \sigma \tag{2.13}$$

$$K = \frac{\pi}{\lambda}\nu\delta n \tag{2.14}$$

$$\alpha = \sqrt{K^2 - \hat{\sigma}^2} \tag{2.15}$$

Here $\hat{\sigma}$ is the self-coupling factor, $K$ is the coupling coefficient between two modes propagating in opposite directions, and $\nu$ represents the visibility of the interference fringes, which in this context corresponds to the contrast between the reflected and transmitted light intensities. The equation of the reflection (R) and transmission (T) of a uniform Bragg grating of length (L) is depicted below :

$$R = |r^2| = \frac{K^2 \sinh^2(\alpha L)}{K^2 \cosh^2(\alpha L) - \hat{\sigma}^2} \tag{2.16}$$

$$T = |t^2| = \frac{\alpha^2}{K^2 \cosh^2(\alpha L) - \hat{\sigma}^2} \tag{2.17}$$

From this point, we can calculate the reflection and transmission of a uniform Bragg grating. The advantage of this simulation is that we can vary the different input parameters and anticipate the theoretical shape of the spectrum.

Considering that we realized this simulation upon a large number of wavelengths we are not able to give precise values of the used parameters because they are wavelength-dependent. But the following table summarizes each parameter and its associated formula.

| Name simulation | Name of the parameter | Unit | Formula |
|:---:|:---:|:---:|:---:|
| $\hat{\sigma}$ | Self coupling factor | No Unit | $\hat{\sigma}^2 = \delta + \sigma$ |
| $\sigma$ | Detunning factor | No Unit | $\frac{2\pi}{\lambda}\delta n$ |
| $\delta$ | Wavevector detuning | $m^{-1}$ | $\delta = \beta - \frac{\pi}{\Lambda} = \frac{2\pi n_{\text{eff}}}{\lambda} - \frac{\pi}{\Lambda}$ |
| K | Coupling coefficient | dB | $\frac{\pi}{\lambda}\nu\delta_n$ |
| $\lambda_{\text{BG}}$ | Bragg Wavelength | m | $\frac{2n_r\Lambda}{m}$ |
| $\nu$ | Visibility of the interference fringes | No Unit | No equation |
| $\delta_n$ | Biggest possible variation of refractive index | URI | No equation |
| $\alpha$ | Variable | | $\sqrt{K^2 - \hat{\sigma}^2}$ |

Table 2.1: List of the different parameters for the simulation.

The Bragg spectrum grating can change under several aspects, it can either be the shape or the length, meaning we can reproduce the same results in different ways. In the current case, we decided to observe the impact of the length ($L$) of the Bragg grating on the shape of the Bragg grating spectrum. So for the simulations, we used the same parameters ($n_{\text{eff}}$ = 1.45, $\Delta$n= 0.0001, $\Lambda$ = 530 nm, $\nu$ = 1) except the length of the Bragg grating. It was varied from 1 to 6 mm. In the following table, we summarized the simulation parameters.
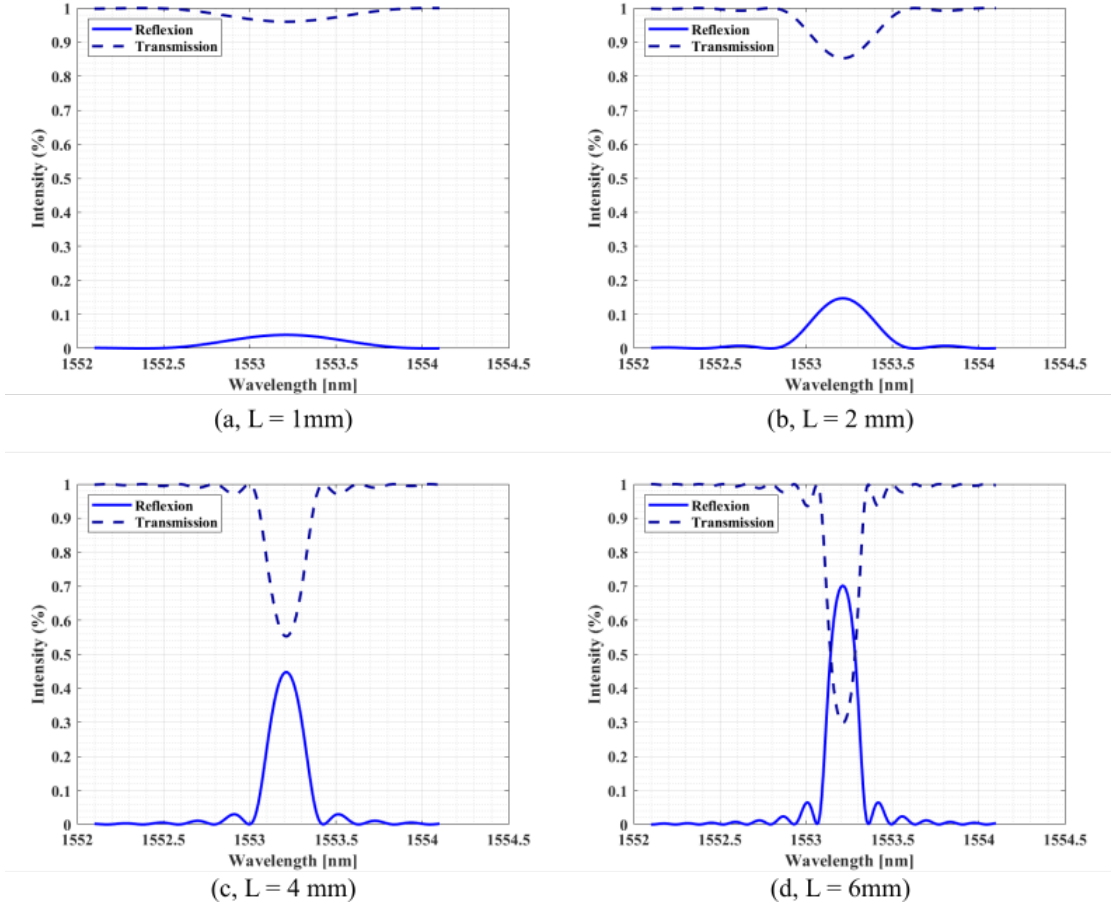
Figure 2.9: Calculation results obtained from the equation 2.16 and 2.17 with several different grating lengths: **(a)** 1 mm, **(b)** 2 mm **(c)** 4 mm **(d)** 6 mm. It is interesting to note that the longer the Bragg grating the narrower the reflected band.

The goal of this calculation presented in Figure 2.9 is to show the evolution of the spectrum in transmission and reflection as a function of the length of the uniform Bragg grating in a waveguide or in the core of an optical fibre. We can observe that the bandwidth decreases while the amplitude increases as a function of the length of the grating. Besides the length of the gratings, other parameters can influence the shape of the grating spectrum like the chirp (linear variation of the grating period), apodization (specific profile of the refractive index modification to remove the side lobes in the spectrum) or the birefringence. This latter effect can be manifested as a double peak of the Bragg wavelength.

In addition to the classical phase mask and interferometric techniques, Bragg gratings are also produced by the point-by-point technique [25] when using femtosecond laser pulses. Other direct inscription techniques are also used like the line-by-line [26, 27] or plane-by-plane [28]. Bragg grating inscribed with a femtosecond laser shows good resistance to high temperatures and harsh environments [29, 30]. Numerous companies developed femtosecond pulsed laser-induced FBGs nowadays.

Besides, the planar glass substrate processing by femtosecond laser has attracted the attention of researchers thanks to the many possibilities they offer for device integration [31, 32, 33]. Efforts have been made to optimize pulsed laser parameters [34, 35], beam shaping, waveguide design [36], and produce low-loss waveguides and waveguides-Bragg gratings [29, 37]. In the following we review the historical methods reported for fibre Bragg grating fabrications.

## 2.2.2 Traditional Methods for Bragg Grating Inscriptions

The principle of Bragg gratings in optical fibre was first introduced by Hill et al. in 1978 at the Canadian Communication Research Centre, Ottawa, Canada [38]. When Hill caused two laser beams to interfere in an optical fibre, he observed a loss of signal intensity which he attributed to the formation of a grating at the core of the fibre itself. His discovery laid the foundations for developing and understanding fibre Bragg gratings. It was not until 1988 that the work of Meltz and Morey [39] demonstrated the photo inscription of Bragg gratings induced by UV radiation directly inside the fibre core from the outside by transverse holographic method.

The principle of their method is shown in Figure 2.10, where the incoming laser beam is split into two beams of equal amplitudes via a beam splitter. These beams are then recombined forming an interference pattern in the core of an optical fibre, where the protective coating has been removed previously. Hence, a permanent refractive index modulation is induced in the fibre core. The periodicity of this refractive index modulation depends on the angle between the two beams, which can be adjusted by rotating the mirrors. The grating periodicity, which matches the periodicity of the interference fringe pattern, depends on both the radiation wavelength (UV) and the angle between the crossing light beams.
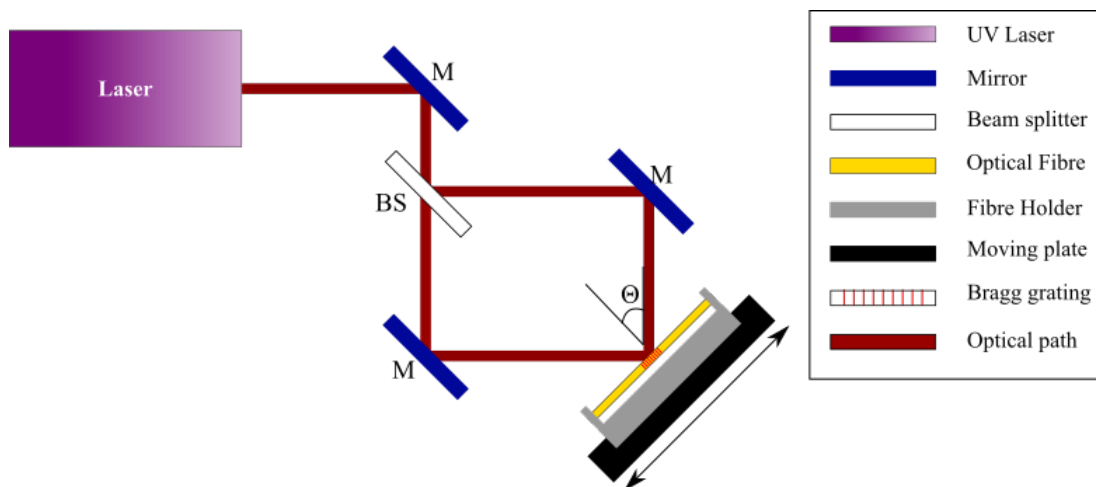


Figure 2.10: Scheme of an interferometric inscription setup of Bragg grating within an optical fibre.

The period of the Bragg grating depends on the laser wavelength and the angle of inscription ($\theta$) [40].

$$\Lambda = \frac{\lambda_{\text{laser}}}{2 \sin \theta} \tag{2.18}$$

$$\lambda_{BG} = \frac{n_{\text{eff}} \Lambda}{\sin \theta} \tag{2.19}$$

The advantage of this fabrication technique is its flexibility, i.e. the possibility to inscribe grating with different Bragg wavelengths. However, this method suffers from instability due to external perturbations (vibration, temperature changes...), moreover, it is limited by the rotation angle of the mirrors. Another technique called the phase mask inscription has been developed by Hill and his team in 1993 [41]. It has since become the most widely used in production because of its good reproducibility. This method is an amplitude-division interference system based on the use of a grating engraved on a silica plate (the mask) placed in quasi-contact with the fibre to be irradiated. The period of the grating is therefore defined by the period of the mask. The tunability of this method is very limited (a few nm by straining the fibre). To produce gratings with different Bragg reflections, one should use a set-up with different phase masks like the commercially available device Noria, a turn-key system proposed by NorthLab Photonics for FBGs inscription presented in Figure 2.11. It consists of an excimer laser from Coherent and a series of phase masks from Ibsen photonics arranged on a rotating stand.



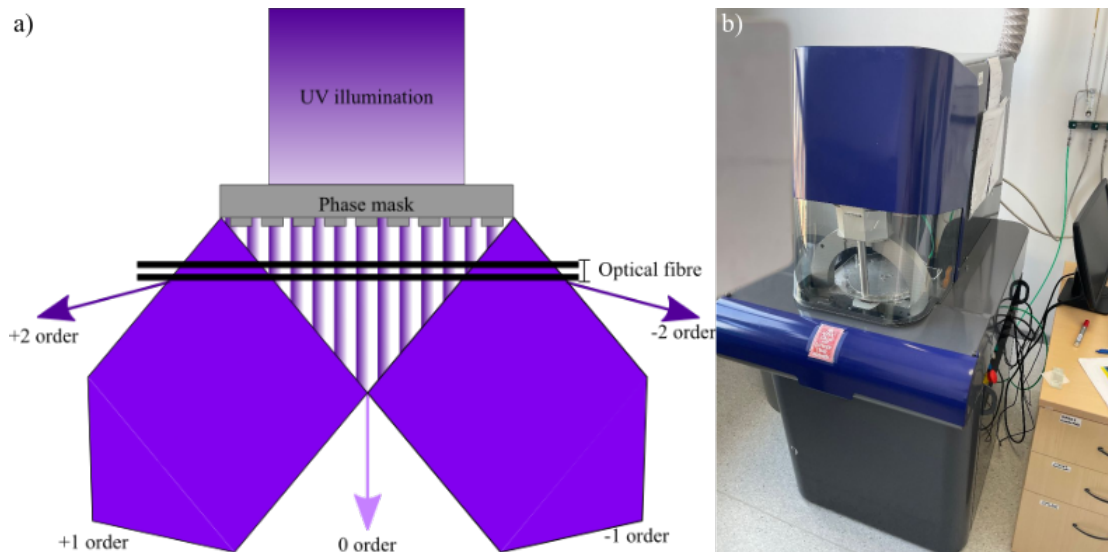Figure 2.11: **(a)** Scheme of a phase mask during the creation of a Bragg grating. **(b)** Picture of the Noria at the University of Mons working on the principle of the phase mask.

In conclusion, we reported two different methods mainly used for (FBGs) inscription in optical fibres: the interferometric and the phase mask methods. The interferometric method uses interference patterns created by splitting and recombining a

laser beam to induce a refractive index modulation in the fibre core. This method is tunable but requires high-vibration stability. Moreover, the used laser should have a high coherence length to ensure interference patterns when the optical path difference between the two interfering beams is high. Whereas the phase mask method is more stable, making it suitable for mass production of FBGs. However, its tunability is very low (few nm) and requires specialized phase masks, which can be expensive. Despite these challenges, the phase mask technique remains a popular choice for many applications. However, with the advancements in laser technology, direct inscription of Bragg gratings into the core of the waveguide has become increasingly prevalent. This method of direct inscription became more popular with the arrival of the femtosecond laser which offers distinct advantages such as enhanced control over the grating parameters and simplified fabrication processes. The details of this approach will be detailed in the next chapter.

## 2.3   Bragg Grating Sensors

These sensors serve as interfaces between the environment and the data acquisition and analysis. By converting physical changes into quantifiable electrical [42], optical, or other measurable signals. Sensors enable the accurate monitoring and characterisation of a wide range of parameters. With their ability to capture and quantify various aspects of the physical world, sensors have become indispensable in numerous fields, including physics, chemistry [43], biology [44], environmental science [45], medicine [46], industrial processes, and beyond. They offer a means to measure and assess factors such as temperature, pressure, humidity, light intensity, motion, acceleration, magnetic fields, chemical concentrations or biological signals. The advancements in sensor technology have led to the development of sensitive and miniaturized sensors that can operate in extreme conditions and offer enhanced precision and accuracy. Moreover, emerging technologies such as nanosensors [47], biosensors [48], and wearable sensors have opened up new avenues for real-time, non-invasive monitoring and personalized healthcare applications. In summary, the underlying principles governing sensors vary depending on their intended application and the specific physical phenomenon they are designed to detect. Common types of sensors use diverse transduction mechanisms, such as capacitive, inductive, piezo-electric, optical, or electrochemical effects, to convert the desired parameter into a measurable signal. This signal is subsequently processed, analysed, and utilized for various purposes, including scientific research, process control, environmental monitoring, medical diagnostics, and numerous other industrial and technological applications.

### 2.3.1   Temperature Response of Bragg Gratings

In the current context, our focus lies in understanding the diverse environmental influences on the Bragg grating phenomenon. The Bragg grating structure can undergo deformation due to various factors [49]. Notably, temperature variations exhibit a particular impact on Bragg grating behaviour. As demonstrated by previous studies [50], an increase in temperature induces material deformation impacting the Bragg

grating. The consequence is a Bragg wavelength shift. This phenomenon serves as a valuable means to characterise the temperature in the Bragg grating. Bragg gratings are sensitive to temperature but also to axial strain, the axial strain is defined as a deformation of the material under a mechanical strain. In the case of Bragg grating, the deformation $\Delta\epsilon$ induces a modification in the period $\Lambda$ of the grating such as : $\epsilon = \frac{\Delta\Lambda}{\Lambda}$ The Bragg wavelength is then shifted ($\Delta\lambda_{\mathrm{BG}}$) as a response to the strain. When both the strain and temperature vary, the induced Bragg wavelength shift is $\frac{\Delta\lambda_{\mathrm{BG}}}{\Delta T}$ and $\frac{\Delta\lambda_{\mathrm{BG}}}{\Delta\epsilon}$. The complete development can be found in [51].

$$\Delta\lambda_{\mathrm{BG}} = 2\left(\Lambda\frac{\mathrm{d}n_{\mathrm{eff}}}{\mathrm{d}T} + n_{\mathrm{eff}}\frac{\mathrm{d}\Lambda}{\mathrm{d}T}\right)\Delta T + 2\left(\Lambda\frac{\mathrm{d}n_{\mathrm{eff}}}{\mathrm{d}\epsilon} + n_{\mathrm{eff}}\frac{\mathrm{d}\Lambda}{\mathrm{d}\epsilon}\right)\Delta\epsilon \qquad (2.20)$$

$$\frac{\Delta\lambda_{\mathrm{BG}}}{\Delta T} = \lambda_{\mathrm{BG}}\left(\frac{1}{n_{\mathrm{eff}}}\frac{\mathrm{d}n_{\mathrm{eff}}}{\mathrm{d}T} + \frac{1}{\Lambda}\frac{\mathrm{d}\Lambda}{\mathrm{d}T}\right) \qquad (2.21)$$

$\frac{1}{n_{\mathrm{eff}}}\frac{\mathrm{d}n_{\mathrm{eff}}}{\mathrm{d}T}$ is the thermo-optic coefficient, whereas $\frac{1}{\Lambda}\frac{\mathrm{d}\Lambda}{\mathrm{d}T}$ is the thermal expansion coefficient, it is the rate at which a material expand itself with the increase of the temperature. In the case of a germanium-doped silica core optical fibre, the thermo-optic coefficient is about $8.6 \times 10^{-6}$ K$^{-1}$. It is the change in the refractive index with the response to the temperature. It also depends on the temperature of the material. Concerning the thermal coefficient, it is about $0.55 \times 10^{-6}$ K$^{-1}$ for silica. By employing the equation, we can subsequently deduce the theoretical displacement of the Bragg peak due to temperature changes represented in equation 2.21. Figure 2.12 portrays a characterisation curve that shows the relationship between the shift in wavelength and the corresponding temperature variations. The resolution of the wavelength will be dependent on the optical spectrum analyser. In the case of Bragg gratings, it is usually of the order of 5 pm.
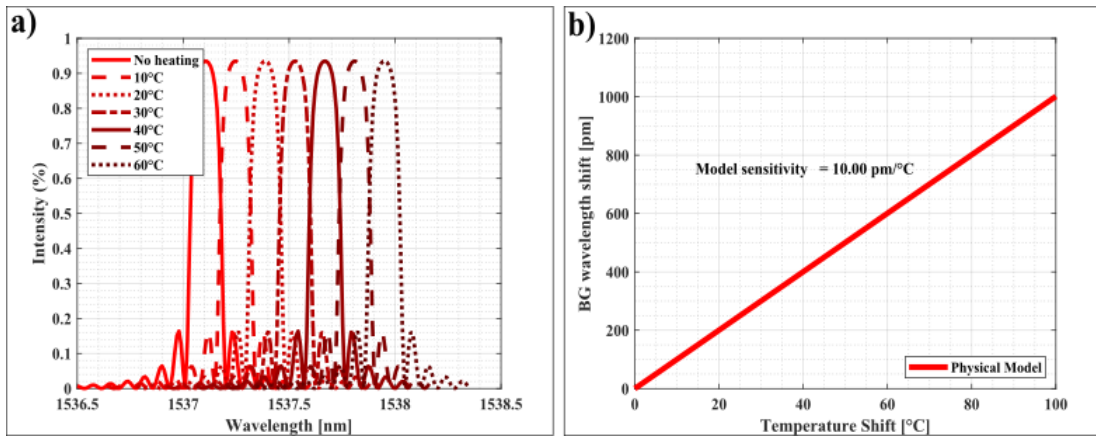


Figure 2.12: **(a)** Graphical representation of the evolution of the Bragg grating spectrum as a function of the temperature. **(b)** Calibration curve showing the evolution of the peak Bragg wavelength as a function of the temperature.

## 2.3.2 Mechanical Response of Bragg Gratings

The second component in Equation 2.20 represents the axial strain deformation. This deformation operates similarly to the temperature characterisation process. A strain is imposed on the Bragg grating, resulting in induced deformation. Various designs will be examined to assess their response to different strains. The quantification of strain applied to the structure and Bragg grating involves calculating the change in Bragg wavelength, which can be expressed as a function of the strain components along the principal axes of the fibre. The sensitivity of the Bragg grating to strain is defined as the change in Bragg wavelength per unit of strain and can be determined experimentally. The strain is strongly dependent on the geometry, the force applied and the position of the Bragg grating. In the current situation, we show three specimen geometries: pure axial strain, three-point flexure and a cantilever beam represented in Figure 2.13. It is important to notice that the deformation of the Bragg grating differs depending on its location compared to the neutral axis.
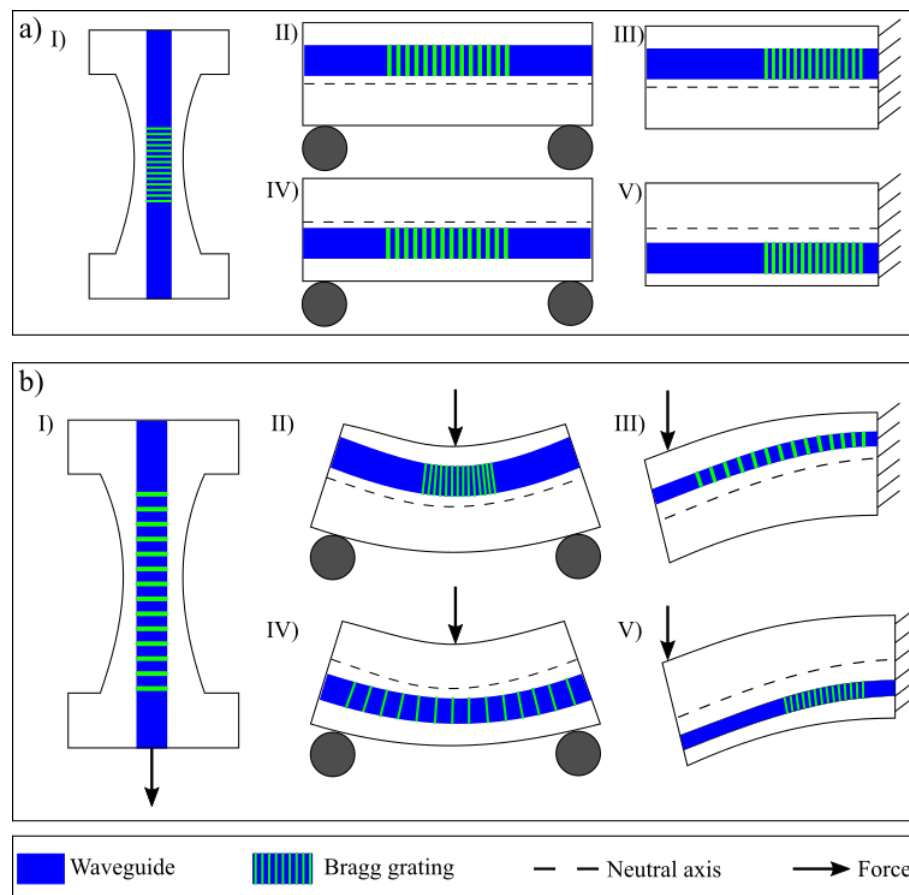
Figure 2.13: (**a**) Schematical representation of three geometries with a Waveguide and a Bragg grating within each structure. I) Axial strain, II) and IV) Three points bending when the Bragg grating is above and below the neutral axis and III) and V) Cantilever beam when the Bragg grating is above and below the neutral axis. (**b**) Same structure described before but under pressure.

The structures represented in Figure 2.13 all rely on the same theory. When these different structures are thin enough (thickness much smaller than length) the shear stress can be neglected compared to the normal stress, and the Euler-Bernoulli [52] equation relates the loading expressed in terms of bending moment $M$ to the geometrical deformation expressed by a local curvature radius $\rho$. Here $E$ is the Young modulus [53] (E = 70 GPa for glass, $E$ = 210 GPa for aluminum) and $I$ is the inertia of the considered section, $I = \frac{bh^3}{12}$ for a rectangular section ($h$ is the beam thickness, $b$ the beam width).
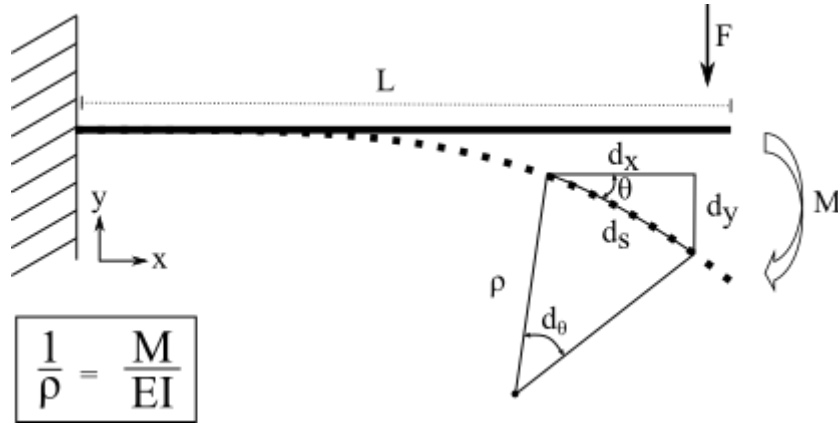


Figure 2.14: Schematic description of the relationship between the curvature radius and the bending moment in the case of the cantilever beam.

To describe the elasticity of the glass we use Hooke's Law [54] relating the stress, $\sigma$, and the strain, $\epsilon$, as represented in equation 2.22,2.23

$$\sigma = \frac{My}{I} \tag{2.22}$$

$$\epsilon = \frac{\sigma}{E} \tag{2.23}$$

The goal here is to study the evolution of bending under different types of stress (Three points, cantilever beam, cross pivot and axial strain). By doing so we will be able to create a link between the strain and the shift of the Bragg grating wavelength. According to the description of the curvature in cartesian coordinates, the complete development is described by Howell [55]. It is also written differently in the following equation where y is the transversal deflection and x is the coordinate along the undeflected beam.

$$\frac{d\theta}{ds} = \frac{d^2y/dx^2}{[1 + (dy/dx)^2]^{3/2}} \tag{2.24}$$

If we assume that the deflection is small, the square of the slope can be assumed to be small compared to the unity in the denominator, leading us to the following equation.

$$M = \frac{\sigma I}{y} = EI\frac{\epsilon}{I} = EI\frac{d^2y}{dx^2} \tag{2.25}$$

Then as a function of tested geometry and the loading conditions, the bending moment is expressed differently, for the cantilever beam:

$$M = F(L - x) \tag{2.26}$$

Here $F$ is the value of the vertical force and $L$ is the beam length, and $x$ is the variable representing the application point of the force. The beam angle is expressed as follows:

$$\theta = \frac{dy}{dx} \tag{2.27}$$

Then we can write M as

$$M = EI\frac{d\theta}{dx} \tag{2.28}$$

$$F(L - x) = EI\frac{d\theta}{dx}, \tag{2.29}$$

It is important to take into account for the next part of the development that if $x$ = 0, then the angle $\theta = 0$, which gives us one of the boundary conditions.

$$\int_0^\theta d\theta = \frac{F}{EI}\int_0^x (L - x)dx \tag{2.30}$$

$$\theta = \frac{F}{EI}(Lx - \frac{x^2}{2}) \tag{2.31}$$

$$\theta = \frac{dy}{dx} = \frac{Fx}{2EI}(2L - x) \tag{2.32}$$

$$y = \int \frac{Fx}{2EI}(2L - x)dx = \frac{F}{2EI}(Lx^2 - \frac{x^3}{3}) + C \tag{2.33}$$

C is found by applying the boundary condition that is $y = 0$ at $x = 0$. It means C = 0.

$$y(x) = \frac{Fx^2}{6EI}(3L - x) \tag{2.34}$$

Equation 2.34 describes the evolution of the strained structure as a function of the young modulus, the length and the strength applied. Then according to Hook's law, we know that the stress and the equation of the moment are strongly dependent from each other as referred in the following equations.

$$\sigma = \frac{My}{I} = \frac{F(l-x)y}{I} \tag{2.35}$$

$$\epsilon = \frac{\sigma}{E} = \frac{F(l-x)y}{EI} \tag{2.36}$$

From equations 2.35 and 2.36, we can deduce the strain applied to the structure. The following table summarizes the different equations in different structures we are interested in.

| Case | Moment | Displacement | Stiffness | Strain | Stress |
|------|--------|--------------|-----------|--------|--------|
| **Cantilevered beam** | $M(x) = F(L-x)$ | $y(x) = \frac{Fx^2}{2EI}(L-\frac{x}{3})$ $\delta = \frac{FL^3}{3EI}$ | $k_{F\delta} = \frac{3EI}{L^3}$ | $\epsilon(x,y) = \frac{F(L-x)y}{EI}$ | $\sigma_{\max} = \frac{3Eh}{2L^2}\delta$ |
| **3 points** | $M(x) = \frac{F}{2}x < \frac{L}{2}$ | $y(x) = \frac{F}{4EI}(\frac{x^3}{3} - \frac{xL^2}{4})$ $\delta = \frac{FL^3}{48EI}$ | $k_{F\delta} = \frac{48EI}{L^3}$ | $\epsilon(x,y) = \frac{Fxy}{2EI}$ | $\sigma_{\max} = \frac{6Eh}{L^2}\delta$ |

Table 2.2: Known geometries that will be developed for the result section of the manuscript.

The objective of this PhD is to leverage the elasticity properties of glass and apply them to the Bragg grating, resulting in a deformation of the Bragg grating through the silica glass structure. For the latest material, the strain-optic constant $p_e$ can be obtained from [51] as:

$$p_{\text{e}} = \frac{n_{\text{eff}}^2}{2}[p_{12} - \nu(p_{11} + p_{12})] \tag{2.37}$$

with $p_{11}$ and $p_{12}$, the elastic-optic independent coefficients for bulk silica ($p_{11} = 0.121$ and $p_{12} = 0.270$), listed in [56], $\nu$ and $n_{\text{eff}}$, respectively its Poisson's ratio and the effective refractive index ($\nu = 0.16$ and $n_{\text{eff}} = 1.45$). With the defined $\lambda_{\text{BG}} \approx 1589$ nm, it gives a theoretical sensitivity to an axial strain of 1.24 pm/µε, as represented in Figure 2.15.
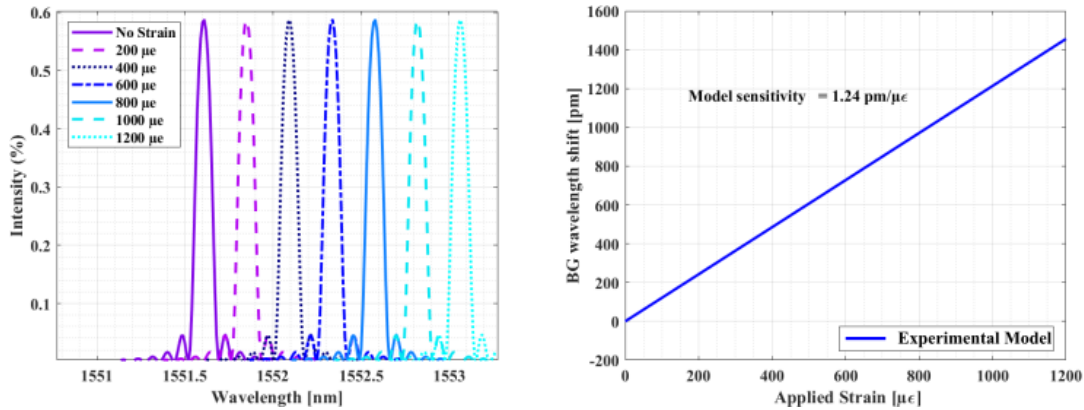


Figure 2.15: **(a)** Calibration curve showing the evolution of the Bragg wavelength as a function of the strain. **(b)** Graphical representation of the evolution of the Bragg grating spectrum as a function of the strain.

The research into the elasticity properties of glass, as explored in the previous section, has direct implications for the design and functionality of optical waveguides. Optical waveguides are crucial components in modern optics and photonics, relying on the manipulation of refractive indices to guide light. While various forms of waveguides exist, including optical fibres, planar waveguides, and integrated waveguides, they all operate on the fundamental principle of exploiting refractive index differences for light confinement and guidance.

## 2.4 Femtosecond lasers

Optical waveguides are essential components in modern optics and photonics, providing a means of confining and guiding light within a material with a higher refractive index than its surroundings. Waveguides can be realized in various forms, including optical fibres [14], planar waveguides [57], and integrated waveguides [58], and can be fabricated from a large range of materials such as silica glass [59], polymers [28, 60, 61], and semiconductors [62]. All these different optical waveguides rely on the same principle: a difference in refractive index to ensure light confinement and guidance. Waveguides exhibit variability not only in their mode but also in their chemical composition. Numerous methods exist for their fabrication. Instead of directly modifying the refractive index, one approach involves modifying the material composition through thin film deposition techniques. This process can be chemical, such as using the sol-gel method or Chemical Vapor Deposition (CVD), or physical, such as employing Radio Frequency Sputtering. These techniques enable precise control over the waveguide's properties, facilitating the creation of tailored optical structures for various applications.

Femtosecond lasers are ultrafast laser that emits extremely short pulses of light ($10^{-15}$ seconds). They are capable of producing high-energy pulses (J) that are useful for a wide range of scientific, industrial, and medical applications [33, 63]. One of the most significant applications of femtosecond lasers is precision material processing. The femtosecond laser will induce the deposition of a certain amount of energy [64, 65, 66]. This deposited energy density, $\Phi_d$ in J/m², has been quantified by Rajesh and Bellouard [67]:

$$\Phi_d = \frac{4E_p}{\pi w_{\mathrm{nl}}}\left(\frac{\Omega}{v}\right) \tag{2.38}$$

Here $E_p$ is the energy of the pulse, $\Omega$ the repetition rate, $v$ the inscription speed and $w_{\mathrm{nl}}$ the nonlinear absorption beam waist. According to the literature [68], the absorbed energy becomes narrower as the order of the multiphoton absorption increases, because the effective absorption cross-section for n-photon ($n_p$) absorption is proportional to the $n_p$-th power of the laser intensity following this equation, where $w$ is the effective beam size for n-photon absorption and $w_0$ is the actual spot size of the focused laser beam.

$$w = w_0/\sqrt{n_p} \tag{2.39}$$

Hence, by definition the non linear absorption will always be smaller or equal to the beam waist. According to Rajesh and Bellouard [65, 67], the deposition energy of a laser depends on various parameters [34, 66]. One such parameter is the pulse energy ($E_p$) in J, which represents the amount of energy, produced by each pulse for hundreds of fs (400fs). Another parameter is the repetition rate ($\Omega$) in Hz, which refers to the frequency of pulse production. The third parameter is the inscription speed ($v$) in m/s, which denotes the rate at which the laser translates through the material. All these parameters allow to control the deposition energy of the femtosecond laser and they can all be adjusted at different levels. Nevertheless, there is still the last parameter that depends on the microscope objective and its numerical aperture, it is the beam waist diameter, $w_0$ in m [69]. It is described in equation 2.40 :

$$w_0 = \frac{2M^2\lambda}{\pi NA} \tag{2.40}$$

Here $\omega_0$ is the linear beam waist diameter in m, $\lambda$ is the laser wavelength in m, M is the beam quality factor and NA is the numerical aperture. A higher numerical aperture indicates that more light can be collected, resulting in higher resolution and a shallower depth of field. The non-linear beam waist is different for each microscope objective due to their different numerical apertures. It is represented in Figure 2.16.
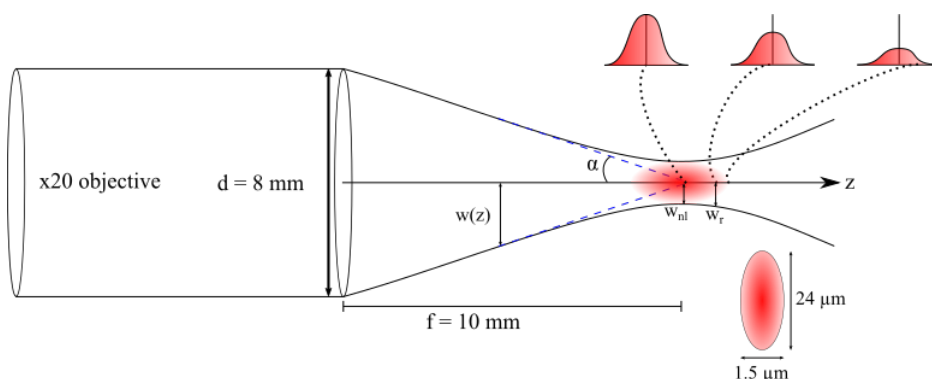


Figure 2.16: Schematic representation of the x20 (NA = 0.4) objective of the femtosecond laser with its linear beam waist and the Gaussian repartition of the signal.

Here $f$ is the focal length, $d$ the diameter of the lens, $w(z)$ the variation of the beam diameter in the beam waist region and $w_r$ the beam diameter associated to the Rayleigh range. It is defined as the value of $z$ where the cross-sectional area of the beam is doubled. Considering that $\lambda = 1030$ nm and assuming that the $M$ quality factor can be considered equal to M² = 1, we are now able to calculate an estimation of the deposited energy depending on the kind of modification we are having.

The ultrafast pulses allow for the precise ablation of material with minimal thermal damage to surrounding areas. This capability has made femtosecond lasers particularly useful in the manufacturing of microelectronic devices, where high precision and accuracy are essential. Scientists investigated the interaction between the ultra-short pulse laser and the surfaces of materials. Further on the principle of multi-photon absorption [64]. Every material exhibits a characteristic band gap (Eg), which is the energy difference between the valence band (VB) and conduction bands (CB) of the material, in the case of the silica glass Eg = 9 eV [70, 71].

$$E = \frac{hc}{\lambda} \tag{2.41}$$

Here $c$ is the speed of light in vaccuum and $h$ is the constant of Planck. It means that the energy to reach the valence band releasing a photon is dependent on the used wavelength. To obtain an energy of 9 eV we have to use a wavelength of 157 nm. In this wavelength range most of the oxides are highly absorbing (beyond the absorption edge). The wavelength of the femtosecond laser is 1030 nm, so to reach the conduction band the simultaneous absorption of 5 photon of identical frequencies via virtual states is required. Hence the multi-photon absorption [72] is an alternative to one-photon or two-step UV (where the defect real intermediate state in the band gap) inscription methods, this phenomenon is depicted in Figure 2.17.
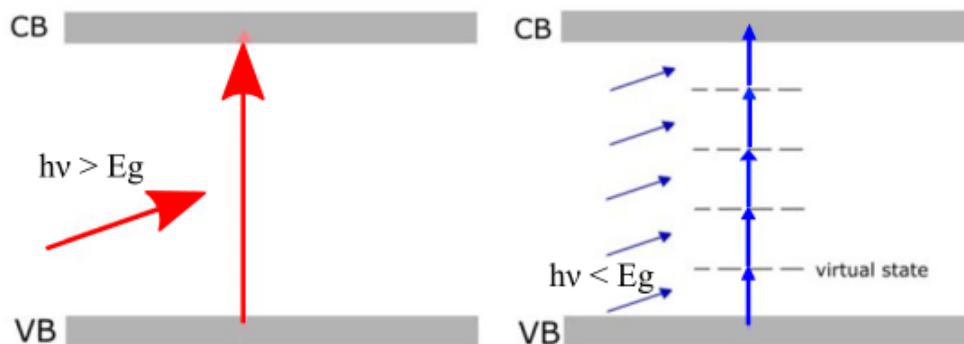


Figure 2.17: Schematic representation of the phenomenon of simple absorption and the phenomenon of multi-photon absorption. VB: Valence Band, CB : Conduction Band.

Several types of modification can emerge from the femtosecond laser pulses [34, 35, 73], the femtosecond laser can impact the silica glass through several types of modification, depending on the energy of the pulse involved. At low energy pulse, several nanojoules, the induced defect is a densification. It will increase the refractive index of the targeted area and then lead to the creation of optical waveguides [74, 75] it is developed in the state-of-the-art section.

If the energy pulse is increased even more the femtosecond laser will create nanograting, corresponding to a structural change of the material that usually takes the form of an alteration of fused silica [34]. Direct ablation, where the material is pushed out of the focal volume leaves a void in the sample [76, 77]. The same laser pulses energy as for the creation of nano-gratings can also be used to shape mechanical structures. Indeed, the glass material that has undergone laser modification is more sensitive to chemical attack than unmodified areas. There is an etching rate difference between the area that has undergone laser modification and the one that has not. This difference is about two orders of magnitude and provides etching selectivity. Accordingly, the laser pulses pattern the material to create a structure to be etched (removed chemically).
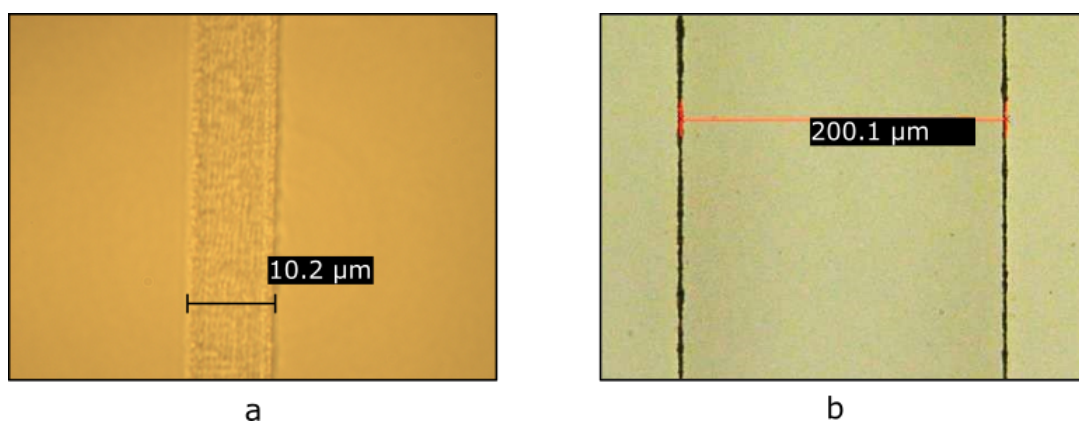


Figure 2.18: Microscopic picture of the different types of modification induced by femtosecond laser. **(a)** Small densification and increase of the refractive index of the silica glass (130 nJ). **(b)** Larger increase in the energy pulse (230 nJ), inducing the creation of nanograting before etching.

The etching process can be conducted in different types of solutions: KOH [78, 79] or HF [80] or NaOH [81], but due to the risk involved while manipulating HF and the selectivity of the etching (HF = 7 µm/h, NaOH = 300 µm/h) we have chosen the KOH. Figure 2.18. a is a picture of a silica glass plate after exposure to a low-energy femtosecond pulse, resulting in densification and an increase in the refractive index. In contrast, Figure 2.18. b is a picture of a silica glass plate after exposure to a higher-energy femtosecond pulse, leading to the creation of nanogratings and a subsequent increase in the refractive index. Due to densification, the refractive index can be increased and therefore waveguides and Bragg grating can be created. In summary, the key principle discussed in this chapter is that to create a waveguide, we need to slightly increase the refractive index by irradiating the silica glass plate with low pulse energy. Once the waveguide is created, we can proceed to create a Bragg grating. The periodic modification occurs when there is a higher increase in the refractive index, resulting in a signal with an associated Bragg wavelength ($\lambda_{BG}$). This wavelength is crucial as it can be predicted and aids in monitoring the signal's evolution under various circumstances, such as changes in polarization state, temperature, or mechanical deformation applied to the structure. The subsequent chapter, will delve deeper into the various concepts previously discussed.

# Chapter 3

# State of the Art Around Femtosecond Laser Technology : Origins, Waveguides, Bragg Gratings and Applications

In this chapter, we will develop the previously introduced concepts. We will start with the historical origins of the femtosecond laser. Then we will give an overview of the existing types of waveguides in various materials, locating our research within the landscape of current research. Then, we will explore the theory and history of Bragg gratings. Finally, we will explore the diverse applications of femtosecond lasers in various contexts.

## 3.1 Introduction

Femtosecond laser pulses have been developed with an increasing field of application in the last decades. The latter emerged 30 years ago and have been successfully applied to the micro-machining of various materials [32, 59, 76, 82, 83, 84, 85]. The first step of the femtosecond laser started in 1972 with Ippen, Shank and Dienes and their dye laser [86, 87]. They have managed to obtain a pulse width of 1.5 picoseconds. They were the group that paved the way toward the creation of femtosecond laser pulses. In 1985, Gerard Mourou and Donna Strickland [88] introduced a ground-breaking technique known as chirped pulse amplification (CPA). This innovation marked an advancement in laser technology, addressing the challenge of generating high-intensity laser pulses without damaging the amplifying medium [89]. Chirped pulse amplification involves several key stages. Initially, long laser pulses are generated, typically on the order of picoseconds ($10^{-12}$ seconds). These stretched-out pulses exhibit a gradually changing frequency profile, hence the term "chirped." This unique characteristic is crucial for preventing optical damage during the amplification process. The chirped pulse is then amplified using an amplifier, significantly boosting its energy without altering the pulse duration.

This stage is critical for achieving high-intensity laser pulses. Successful amplification requires careful control of parameters like pulse duration and energy. Following amplification, the chirped pulse undergoes compression. A specialised device or material introduces a controlled time delay among the different frequency components of the pulse. This deliberate manipulation of frequencies enables the pulse to be compressed in time maintaining its energy content. Mourou and his team applied chirped pulse amplification to a dye laser experiment, resulting in femtosecond laser pulses with durations as short as 500 femtoseconds and an energy of deposition of 1023 W/cm$^2$. This achievement marked a major milestone, enabling the exploration of ultrafast phenomena and applications. The impact of femtosecond laser pulses extends across various fields. Industries have leveraged these short, high-energy pulses for precision material processing, micromachining, and the creation of nanostructures. Additionally, femtosecond lasers have found applications in medical procedures like eye surgeries and microfabrication due to their precision and minimal thermal damage. The femtosecond laser has a very interesting specificity in its capabilities of inscribing on a wide range of various materials: glass, metals, polymers, and semiconductors.

## 3.2   Essential Principles of Femtosecond Laser Technology

As previously described, the notion of ultra-fast lasers originates from chirped pulse amplification (CPA). This process, which will be detailed in the following section of this review, represents an innovative approach. The creation of the femtosecond laser started in 1972 with the improvement of the dye laser. The latter is a laser that uses an organic dye (usually a liquid solution) as a lasing medium. The advantage of the dye laser results from its a broad band of diffuse energy rather than a set of discrete energy levels. The organic liquids are chosen because of their strong absorption band between Ultraviolet and Near Infrared (NIR). These special liquids contain a special system of conjugated bonds (alternating single and double). As depicted in Figure 3.1, the dye laser exhibits distinct energy levels. However, only a few of the possible configurations of the dye lasers possess the suitable arrangement to transform into practical dye lasers, enabling the generation of picosecond laser pulses. In the context presented by Ippen, the laser in use is an Argon laser, which is guided through the dyed solution. Within this setup, two distinct dyed solutions are employed. The initial solution, positioned at the output of the continuous Argon laser, comprises Rhodamine 6G ($4 \times 10^{-4}$ M in water with 5 % Ammonyx-LO), while the other end of the laser is a cell containing a solution of DODCI (diethyloxadicarbocyanine iodide) at a concentration of $2 \times 10^{-5}$ in methanol. In both cases, the solutions are subjected to filtration and then directed along the optical path. The excitation from the Argon laser propels the solutions into higher energy states, followed by their return to lower energy states, resulting in phosphorescence generation. These phosphorescent photons undergo amplification to avoid any loss in the compression process, through the arrangement illustrated in Figure 3.1.
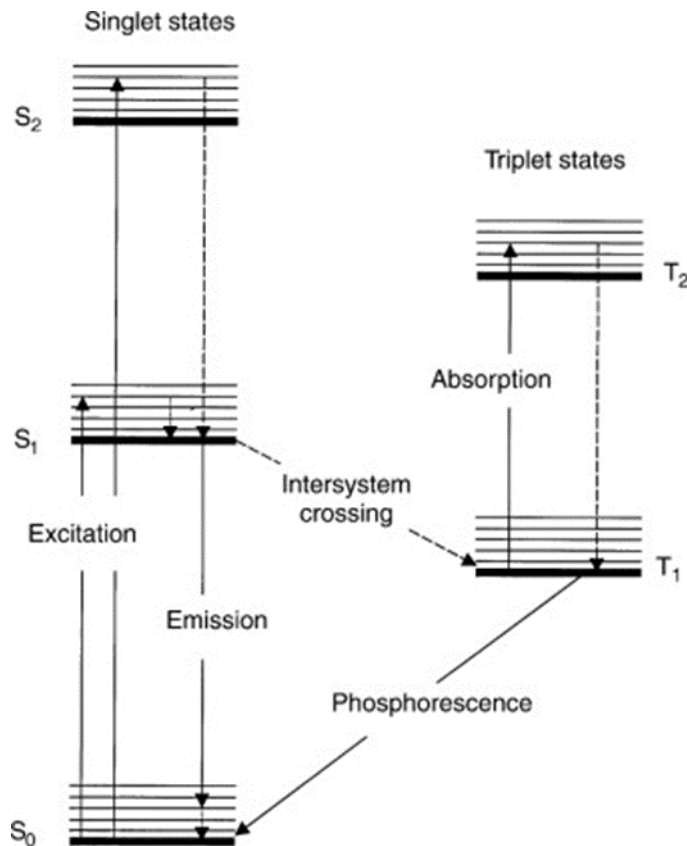
Figure 3.1: Schematic energy level diagram for a dye molecule. Full lines: radiative transitions; dashed lines: nonradiative transitions. [90]

The spectrum alone provides the means to measure a bandwidth of 2.3 picoseconds, assuming a Gaussian distribution. Then for the femtosecond laser, we have to study another technology which is the chirped pulse amplification. It is a process separated into several parts, the stretching of the initial signal, the amplification and the compression. For the creation of the femtosecond laser, the initial signal should be as small as possible which is why the dye laser is a good solution for the initial signal because it allows to create a long and continuous signal with a very short pulse duration. Concerning the amplification its goal is to increase the energy of the different pulses. To amplify the energy of the pulse Mourou decided to use a double grating compressor. The amplifier is made of Neodymium glass and it works as a regenerative amplifier by reflection.

The goal is to amplify the energy until it reaches an energy of several millijoules (mJ). Once this energy level is achieved, the pulse is transmitted through an anti-reflective (AR) coated window to a double grating compressor. The purpose of this compressor is to separate the different pulses and compress them into an even shorter duration while preserving the pulse energy. This marks the birth of the femtosecond laser.
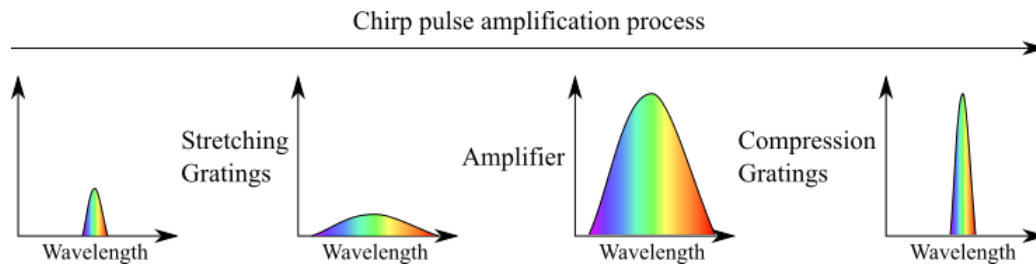
Figure 3.2: Schematic representation of the chirp pulse amplification process adapted from the litterature. [91]

## 3.3   Femtosecond Laser Pulses Fabrication in Silica.

Inscription with the femtosecond laser is possible on several types of materials such as semiconductors, metals, polymers, glass, biological materials or composites. The femtosecond laser affects the material in different ways according to the chosen material.  This is an important part of the femtosecond laser because it is what determines the advantage of using this instead of a longer pulsed laser. As depicted in Figure 3.3, the use of an ultra-fast laser results in a substantial reduction of thermal effects on the material [92, 93]. This translates to a diminished generation of damage caused by the femtosecond laser. The distinctions in effects between a femtosecond laser and a laser with a longer pulse are illustrated in Figure 3.3 (a) and (b). In the case of the longer pulse laser, a notable heat-affected zone emerges, meaning that the structure undergoes diverse forms of damage. This can be observed in Figure 3.3 (c), where the quality of the surface surrounding the impact is severely compromised. In contrast, when employing an ultra-fast laser pulse like the femtosecond laser, the heat-affected zone is notably smaller, as depicted in Figure 3.3 (d).  Additionally, the material surface exhibits a considerably lower amount of debris compared to the longer pulsed laser. This property stands out as one of the primary advantages of the femtosecond laser when compared to other existing laser types.
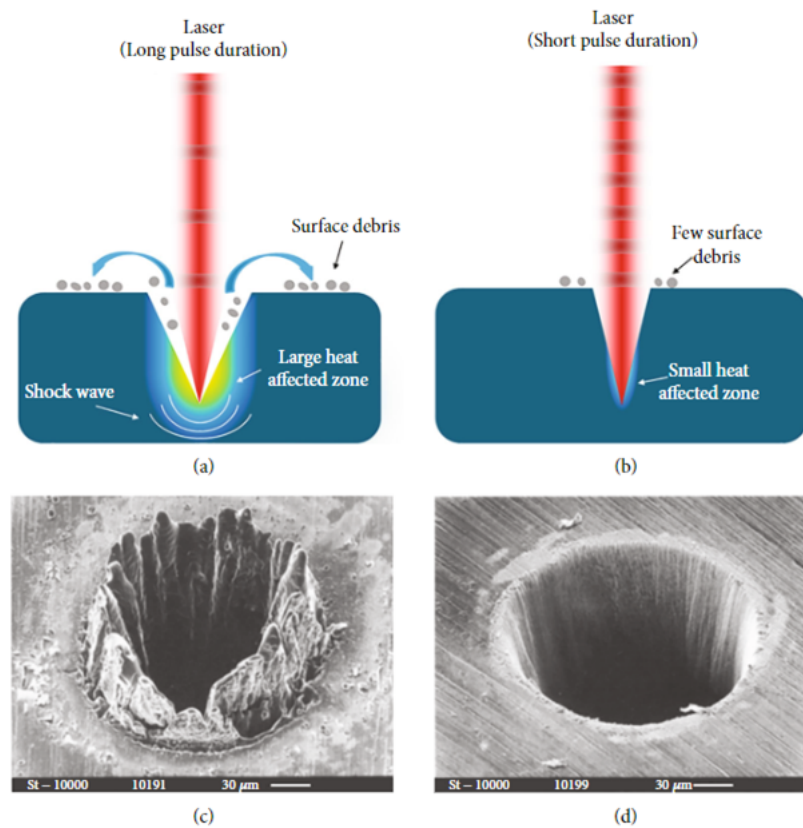
Figure 3.3: Schematic of laser interaction with materials under different pulse durations: **(a)** long pulse duration and **(b)** short pulse duration. SEM images of laser ablated holes fabricated on a 100 µm steel foil by **(c)** 780 nm nanosecond laser of 3.3 ns, 0.5 J/cm² and **(d)** 780 nm femtosecond laser of 200 fs, 0.5 J/cm². [93]

For several cases, the femtosecond laser pulse is used to do micromachining [94, 95, 96]. It is the process of fabricating microstructures or microdevices on glass substrates using various machining techniques. It is important to note that this ablation could also be applied on other types of materials such as metals [97]. The micromachining process relies on several steps, the first is the pattern on the glass structure using a femtosecond laser and then a process of chemical etching with an etching agent (In this case KOH but can also be HF). Most of the microstructures conceived with femtosecond laser rely on the same setup represented in Figure 3.4. In this setup, the femtosecond laser is focused by a lens in the direction of a sample fixed on an X-Y translation stage. The setup also involves key components such as the beam splitter and joulemeter, working together to oversee the energy levels of the femtosecond laser pulses. The beam splitter efficiently splits the laser beam, allowing accurate energy measurements through the joulemeter. This monitoring serves as the foundation for various applications requiring precision. Adding to this setup, the electromechanical shutter plays a significant role. It can regulate the frequency and timing of laser pulse application. This innovation enhances the adaptability of femtosecond laser systems. In this setup, the variable attenuator is another important element.

It allows adjusting the laser's intensity interacting with the sample. Researchers can adjust the experimental conditions for tasks demanding precise laser-sample interactions. A polarizer allows us to control the angle of the linear polarization. This control is important because, depending on the type of polarization, we can induce different types of modifications.
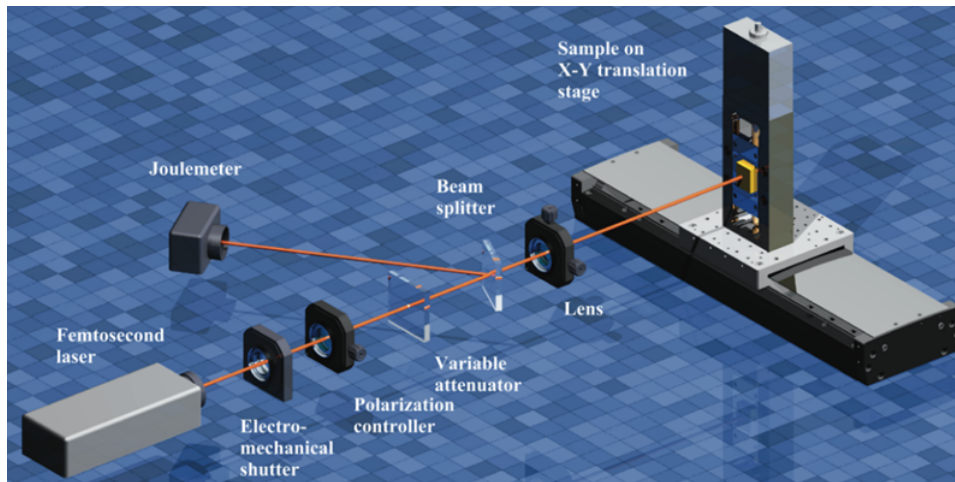


Figure 3.4: Typical experimental setup for surface nano/microstructure under a femtosecond modification. [98]

As previously explained, the femtosecond laser can bring various types of alterations, which are dependent on the different input parameters. When a femtosecond laser interacts with a silica glass plate a change of structure takes place. The silica glass is mostly composed of a six-silicon-ring of quartz, as depicted in Figure 3.5, but when the femtosecond laser interacts with the silica glass this structuration turns it into the three-membered ring of quartz [99, 100], it also induces a change of density because on the same surface there are smaller pack of ring, resulting in a densification or an elevation of the refractive index. This is mostly employed for silica glass, particularly in the generation of optical waveguides. The remaining two forms of alteration mainly centre around mechanical or structural adjustments. There exist numerous methods for modifying these structures, but in this instance, we will concentrate on two of them. The first method involves femtosecond laser-assisted wet etching, a two-stage process. Initially, the sample undergoes exposure to a femtosecond laser emitting a pulse with moderate energy (for instance, in the case of this PhD we worked with silica glass, the pulse energy is 230 nJ). This exposure results in the creation of nano gratings along the structure. Subsequently, these nano gratings are etched using a potent acid (HF) or a strong base (KOH), leading to a chemical reaction between the nano gratings and the etching agent, resulting in material disintegration. Raising the energy of the laser pulse even more will induce direct material ablation. However, this higher energy level was not employed with silica glass due to its susceptibility to break.
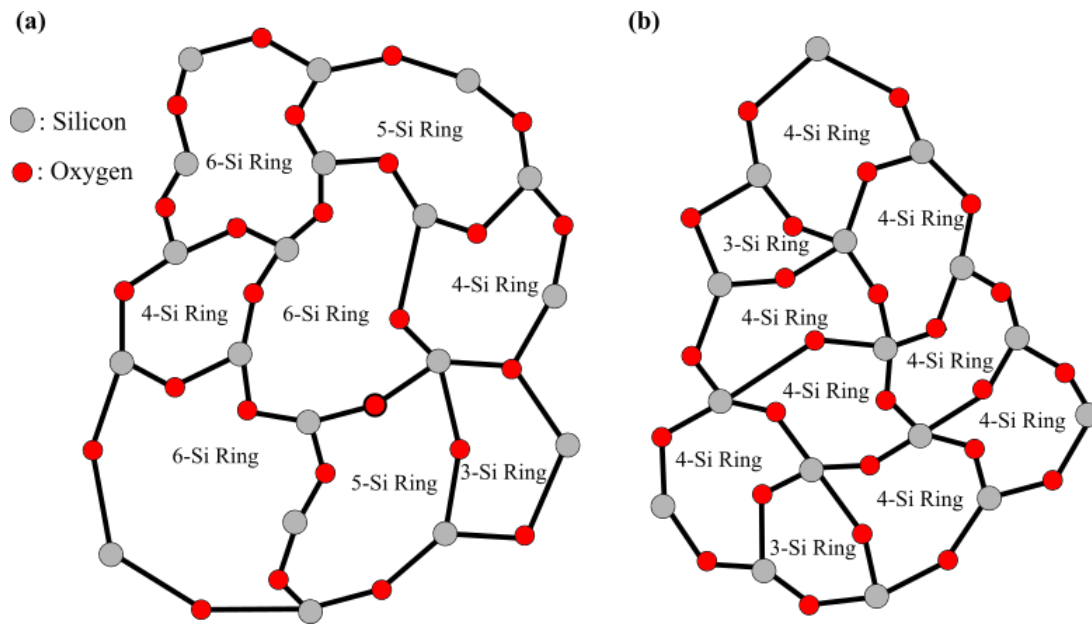
Figure 3.5: **(a)** Schematical representation of the original fused silica structure. **(b)** Schematical representation of the structure of fused silica after it has been irradiated by a femtosecond laser at low energy. [100]

The impact of the femtosecond laser led to a densification of the structure of the silica glass. This explains why the KOH is etching faster on the exposed part than on the non-exposed part. From a chemical point of view, the KOH attacks the silica glass but the specificity as explained before is linked to the structure of the glass. Concerning the reaction of dissolution it is explained by Campbell in 1995 and represented below [79].

$$Si + 4OH^- \rightarrow Si(OH)_4 + 4e^-$$
$$4e^- + 4H_2O \rightarrow 4OH^- + 2H_2$$
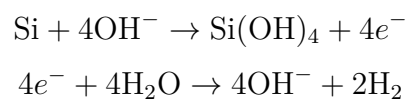
In the equation, $OH^-$ ions are introduced by the KOH base. These ions then proceed to target the Si-O-Si bond, resulting in the formation of silicic acid ($Si(OH)_4$), which is subsequently released into the surrounding water along with four electrons. The generation of small bubbles comes from the generation of hydrogen gas ($H_2$). It is important to note that KOH evenly spreads across the entire surface of the silica glass plate. However, a noteworthy distinction exists: KOH diffusion occurs more rapidly on the irradiated surfaces compared to the non-irradiated ones due to the reactivity of the irradiated surfaces. This variance in etching rates holds significance because there is a two-order-of-magnitude difference in speed, with the irradiated region at a rate of 130 µm/h and the non-irradiated region at 0.7 µm/h. These explanations are important parameters to take into account as a function of the different structures created with a femtosecond laser.

# 3.4   Structures Created With the Femtosecond Laser

As previously explained, the femtosecond laser represents a new research area in materials science, enabling precise interactions with matter at the smallest scale. In femtosecond laser irradiation of optical fibers, two distinct regimes yield different outcomes: Type I irradiation creates waveguides by modifying the refractive index to enhance light guidance, while Type II irradiation forms nanogratings, which are fine periodic structures that enable selective chemical etching for precise microstructuring. By densifying glass and increasing its refractive index, this technology enables the creation of high-quality waveguides and Bragg gratings. Additionally, it allows for wet etching throughout the entire structure, facilitating the design of new shapes for silica glass. This section delves into the fabrication of these structures and their transformative impact on fields such as photonics, optoelectronics, and biomedicine.

## 3.4.1   Waveguide

Femtosecond lasers have paved the way towards advancements in several areas of science and technology [33]. One of these applications is the inscription of optical structures on transparent materials [101, 102]. This transition marks a natural evolution of femtosecond laser technology, shifting from its use in precise surgery to its application in nanofabrication and advanced optics. In this new frontier of research, scientists and engineers are harnessing the properties of these ultrashort lasers to manipulate matter at the nanoscale, opening exciting prospects in integrated optics, photonics, and telecommunications. Through precise and reproducible inscription processes, femtosecond lasers enable the creation of complex optical structures, such as waveguides, diffraction gratings, and microlenses, directly within transparent materials like glass [103]. In summary, the transition from femtosecond laser surgery to the inscription of optical structures on transparent materials using a femtosecond laser represents an example of adapting cutting-edge medical technologies to diverse technology. The femtosecond laser is employed to inscribe these waveguides through various methods. Multiple techniques exist for inscribing optical waveguides using a femtosecond laser. As previously mentioned, the inscription principle relies on using low-energy pulses to induce minor densification leading to an increase of the refractive index. This densification, in turn, enhances the refractive index of the structure impacted by the femtosecond laser. Several key parameters are integral to the formation of optical waveguides. The laser path's shape and design are critical factors that determine the resultant waveguide appearance. Additionally, the energy involved plays a key role in whether densification or alternative modifications occur. Various methods of inscription have been investigated for waveguides. Figure 3.6 depicts parameters values used in the literature for the inscription of the waveguide. The x-axis corresponds to the pulse energy while the y-axis to the writing speed. A quite important dispersion can be noticed
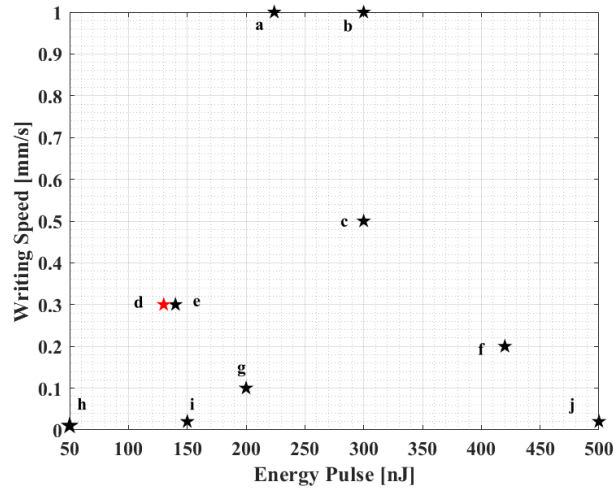
Figure 3.6: Graphic showing the parameter used in the literature for the creation of optical waveguide. **a**: [37], **b**: [104], **c**: [105], **d**: [106], **e**: [107], **f**: [108], **g**: [109], **h**: [110], **i**: [111], **j**: [112].

The first approach involves creating two single paths positioned closely together, inducing densification and consequently altering the refractive index between these adjacent laser paths. Another technique entails encircling the optical waveguide with a closely wound helical path, resulting in densification surrounding the waveguide. Alternatively, overlapping different laser paths and voxels can be employed to produce a homogenized waveguide within silica glass.
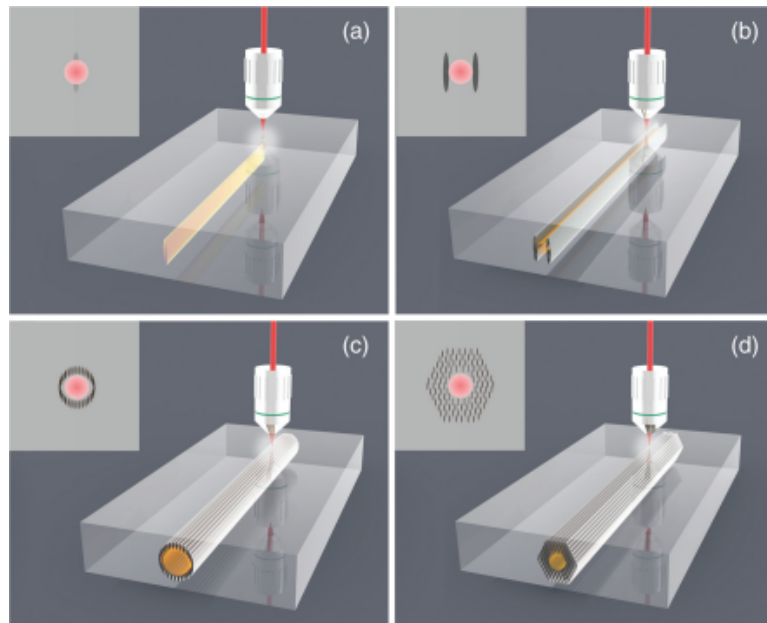


Figure 3.7: Typical experimental setup for surface nano/microstructure under a femtosecond modification : **(a)** single-line, **(b)** double-line, **(c)** depressed-cladding, and **(d)** optical-lattice-like configurations.

[84]

It is important to know that the choice of inscription method for laser paths significantly impacts the waveguide's geometry. Furthermore, it should be noted that while our study primarily focused on inscribing waveguides in silica glass, waveguide can also be inscribed in various types of materials, especially for polymers. There is a large variety of techniques that allow the inscription of waveguide on polymers including photolithography [113] or femtosecond laser processing[61]. The primary advantage inherent to polymer materials predominantly lies in their cost-effectiveness during the production phase, a quality distinguished when contrasted with crystalline materials. However, it is imperative to acknowledge that polymers exhibit heightened sensitivity to temperature variations, making them incapable of supporting extreme thermal conditions, typically exceeding a designated threshold.

Polymers further distinguish themselves by their high flexibility, which allows for easier structural modifications. One example of polymers frequently employed in the field of waveguide technology is Polymethyl Methacrylate (PMMA), prized for its optical transparency and elevated refractive index (n = 1.49). An illustrative instance of PMMA's application in waveguide fabrication was presented by S. Sowa in 2006, who achieved the creation of an optical waveguide through the use of femtosecond laser pulses [114].

Due to the characteristics of polymers, the energy requirements for inscription, as well as the repetition rate of femtosecond lasers, are diminished in comparison to silica glass counterparts. Presently, the requisite energy input stands at 27 nJ per pulse, with a repetition rate of 1 kHz, resulting in an alteration of the refractive index by a magnitude of $4.6 \times 10^{-4}$. This affords polymers a distinctively intriguing and innovative position within the domain of waveguide materials.

However, it is important to acknowledge the inherent fragility associated with polymer structures. Their inability to endure elevated temperature regimes, such as the fusion point of PMMA, which stands at 160°C, renders polymers less than optimal for deployment in exceedingly harsh environmental conditions. Despite this limitation, it is notable that Bragg gratings can indeed be inscribed within polymer matrices, underscoring the versatility of these materials in specific optical applications.

### 3.4.2   Bragg Grating

As explained previously the Bragg grating is a periodic modification of the refractive index in the centre of a fibre or an optical waveguide. This periodic deformation is characterised by a reflected spectrum and a transmitted spectrum. The characteristic wavelength of these two spectras can be used in several ways but in the current case, we will focus on the characterisation of the temperature and the mechanical deformation applied. First Bragg gratings were mostly inscribed within optical fibres due to the minimal loss and the flexibility of the material. Bragg grating can be inscribed in several ways but the two most common are the inscription with UV laser and the phase mask method or direct inscription methods with a femtosecond pulses laser. Various types of Bragg gratings can be synthesized via two fundamental modification approaches.

The first approach involves precise point-by-point [115], line-by-line [27] or plane-by-plane [28] alterations in the structure. The second approach pertains to the manipulation of the periodicity itself and with it the modification of the signal, resulting in outcomes such as two distinct Bragg gratings within a single waveguide, the generation of chirped Bragg gratings or the generation of tilted Bragg grating, among other possibilities. Point-by-point, line-by-line, and plane-by-plane Bragg gratings share analogous optical responses in terms of Bragg wavelength and intensity, even if they differ in geometrical attributes along the waveguide. In contrast, tilting the Bragg grating yields tilted fibre Bragg gratings (TFBGs), which exhibit heightened optical versatility.
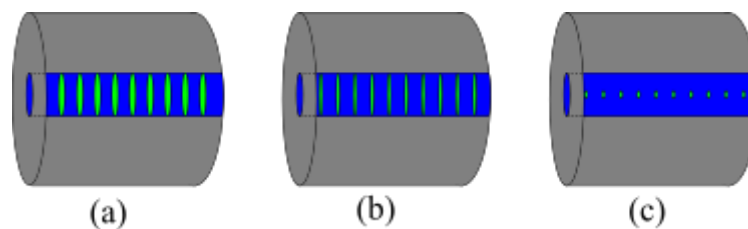


Figure 3.8: Schematic representation of the different types of uniform Bragg grating. **(a)** plane-by-plane, **(b)** Line-by-line and **(c)** point by point Bragg grating.

TFBGs [116], due to their inclined configuration enable the extraction of information regarding the cladding mode behaviour of the fibre. They offer a means to probe surface-related phenomena occurring at the Bragg grating interface. Furthermore, it is possible to introduce spatial variations within the Bragg grating by modulating the period across its length. This results is the creation of a chirped Bragg grating, featuring an irregular evolution of the period. The spacing between the input and output ends is expanded. This chirped setup can serve as both a signal equalizer for the Bragg grating and a compensator for various input optical waves. This observation is significant as it facilitates testing across a longer distance along the entire waveguide. In Figure 3.9 we observe the response of a Tilted Bragg grating [116] and a Chirped Bragg grating [117]. These two spectras strongly differ from the uniform Bragg grating because due to the shape or the different periods of the Bragg grating.

Optical fibre are made of silica glass which has a melting point of 1700 °C [119, 120]. It is a very high temperature and it means it can survive in very harsh environments. Mihailov made several tests over the Bragg grating in harsh conditions. Depending on the range of used temperature the Bragg grating response will strongly differ. Type IA induced by UV exposition is limited to 300 °C for long time use. Whereas Type II fibre Bragg grating induced by femtosecond inscription is more suitable to support higher temperatures. In this situation, Mihailov made a Bragg grating able to reach a temperature of 1000 °C. It is also possible to do a pre-annealing (700 °C) of the optical fibre to remove any stress and that leads to a stable signal up to 1200 °C [50]. Bragg grating can also be the source of birefringence which can be characterised thanks to polarized light. The manufacturing process is lateral/transverse to the optical fibre cross-section it results in an asymmetry of the refractive index modulation leading to photo induce birefringence.
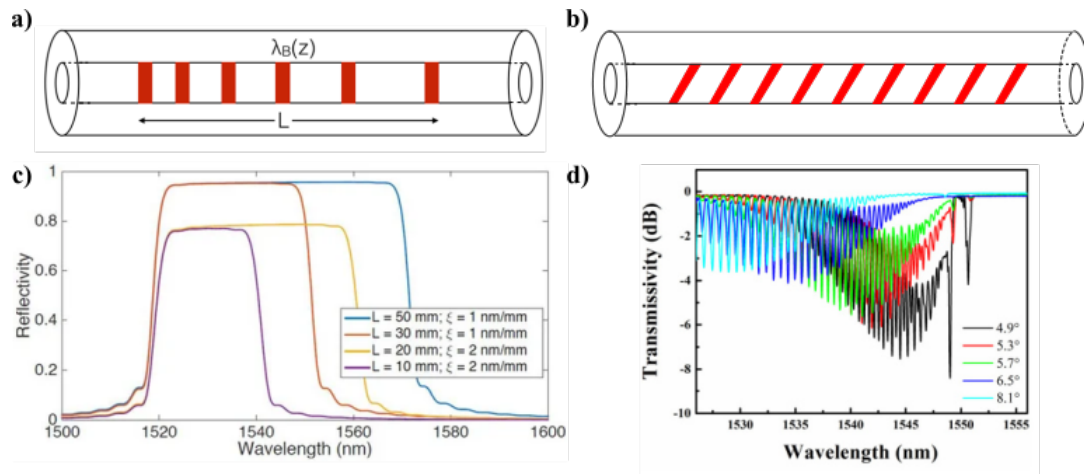
Figure 3.9: (**a**) Schematic representation of a Chirped Fibre Bragg grating. (**b**) Schematic representation of a Tilted Fibre Bragg grating. (**c**) Spectra of Chirped Bragg gratings for different lengths and chip coefficients (**d**) Spectra of Tilted Bragg grating for differents tilted angles. [117, 118]

Polarized lightwaves are represented by perpendicular electric and magnetic field vectors in a transverse plane, perpendicular to the direction of propagation. The state of polarization is defined by the pattern of the electric field vector over time at a fixed position in space. Partially polarized light is a mix of fully polarized and unpolarized light, with a degree of polarization ranging from 0 (unpolarized) to 1 (totally polarized). The degree of polarization can change in transmission media depending on the source spectral width and the medium's dispersive properties. In function of the shape of the curve, we can deduce the birefringence of the measures.

### 3.4.3   Mechanical Deformation of Compliant Mechanisms

There are several approaches for characterising the force applied on a Bragg grating. The first method involves assessing the strain, which is relatively straightforward when dealing with an optical fibre. It means applying tension to the fibre and determining the magnitude of the applied force. Depending on the applied force, we can establish the sensitivity of the silica glass and correlate it with the shift in the spectrum, measured in picometers.

Various fused silica flexure mechanisms have been developed for diverse applications. For instance, Bellouard et al. [121] introduced a monolithic optomechanical micro-displacement sensor with a 50 nm resolution. This sensor comprises a translational guidance system equipped with an integrated linear encoder. Displacement is optically measured via an integrated waveguide located in the sensor frame, oriented perpendicularly to the linear encoder.

Lenssen and Bellouard [123] demonstrated a transparent glass monolithic micro-actuator that operates using a capacitive comb array. A transparent conductive material, such as an indium-tin-oxide layer, is deposited on the structure. The comb array is guided in translation by a flexure mechanism.
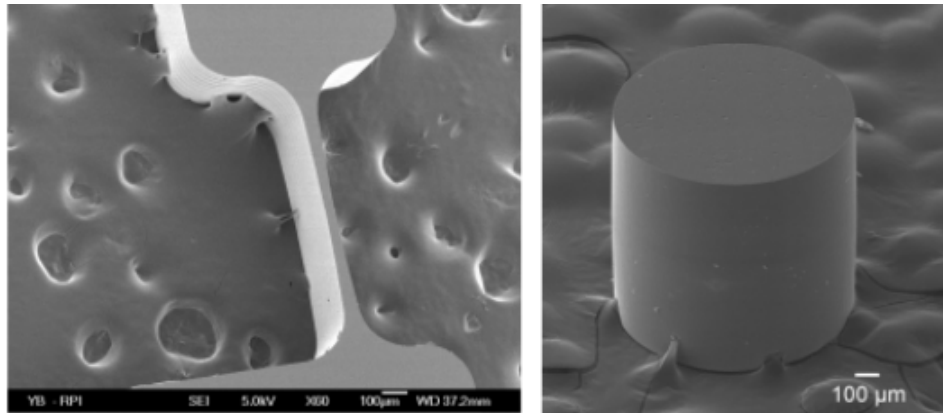
Figure 3.10: A micro-hinge (left) and a cylinder (right) manufactured using the hybrid femtosecond /chemical etching process. [122]

.

Nazir and Bellouard [124] proposed a laser-to-fibre coupling mechanism incorporated into a monolithic fused silica tunable flexure mechanism, enabling sub-nanometer resolution positioning over a range of motion spanning tens of micrometres. Nazir et al. [125] applied their concept of stressors to load a micro-tensile tester for conducting extended static stress measurements under normal atmospheric conditions.

Zanaty et al.[126] introduced a multistable glass monolithic mechanism designed for safe surgical puncturing. This mechanism allows for the independent adjustment of the force and stroke applied by the needle at the output, with a tunable range of 5-20° stroke and a force exceeding 8 mN.



Figure 3.11: Table states of the mechanism, puncturing occurs on switching from (a) pre-puncturing state to (b) post-puncturing state. [126]

Tissot-Daguette et al[127] presented a constant-force surgical tool based on a monolithic glass flexure mechanism, providing 1 gf of force with a maximum variation of 0.1 gf over a displacement range of 870 micrometres.

A microscope is employed to provide visual feedback regarding the output displacement. It is important to recognize that our understanding of material behaviour at the microscale has paved the way for groundbreaking innovations for several types of sensors.

## 3.5    Applications of Femtosecond Laser

Femtosecond lasers have enabled a major improvement for precise micromachining and microfabrication of materials such as glass or polymer. Concerning the area of hydrophobic and hydrophilic structures, femtosecond lasers are employed to engineer surfaces with tailored wetting properties, impacting materials science or medical devices. Our chapter will conclude with the new machine called the Femtoprint, a convergence of these two distinct applications. Through the Femtoprint machine, we witness a novel technology that harnesses femtosecond lasers to create intricate microstructures with precise control, promising a host of innovations and advancements in diverse fields.

### 3.5.1    Optic and Microfluidic in Transparent Material

The initial application of the femtosecond laser is primarily focused on the creation of optical structures. In our research, we specifically concentrate on the waveguide and the Bragg grating, as they serve as the first steps for any eventual application. One of the key advantages of the femtosecond laser is its low cost, small volume, and strong performance, making it an ideal tool for fabricating microstructures, such as microlenses. They are optical components designed to focus light in microscale applications. They are typically made of transparent materials such as silica glass. They are used in a wide range of applications, including imaging systems, optical communications or laser systems. They can be fabricated through the femtosecond laser-assisted wet etching, but also with a technique of embossing micro plastic [128] or thermal reflow method [129]. An example of Microlens is represented in Figure 3.12.
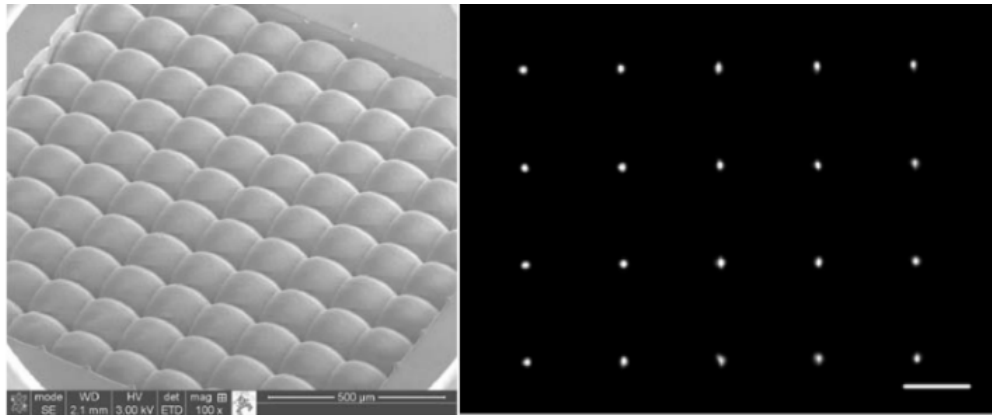
Figure 3.12: SEM images of the plano-convex spherical microlens arrays (left). The image of the focusing line array using a ×4 objective lens, the scale bar is 100 µm (right). [103]

While the fabrication of microlenses is an aspect of optical engineering, the capabilities of the femtosecond laser extend to a broader array of applications. One such application is the creation of biosensors. However, several types of biosensors can be created. For example, integrating optics with microfluidics is a common technique in the new way of creating biosensors. This lab-on-chip technique is particularly interesting because it allows for the integration of a Bragg grating sensitive to the surface and a microfluidic structure on the same chip. In a typical lab-on-chip device, a Bragg grating is used as a sensor to detect changes in the surrounding environment.
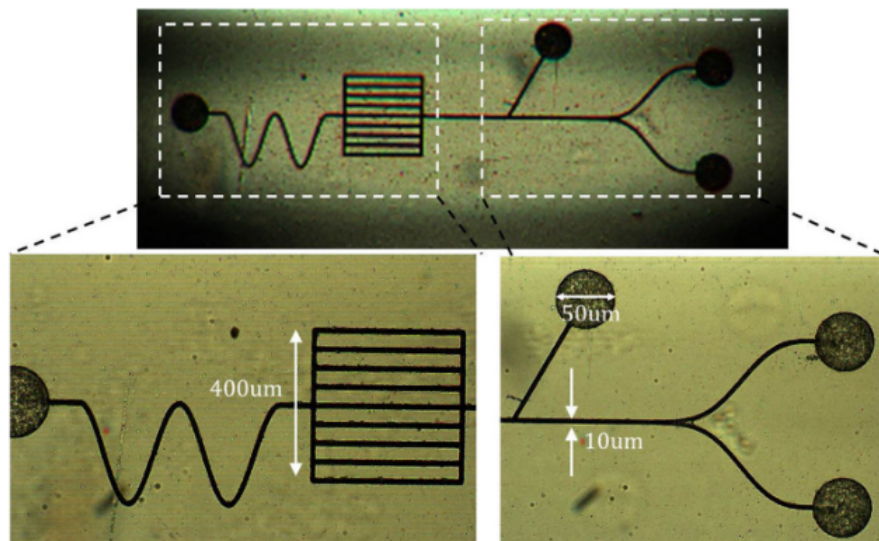


Figure 3.13: Optical images of the microfluidic device on the top surface of a flat polished fibre. [130]

By integrating the Bragg grating with a microfluidic system, the lab-on-chip device can perform a wide range of biochemical analyses. For example, the microfluidic system can be used to transport a sample to the Bragg grating, where it can be analyzed for the presence of specific molecules. The microfluidic system can also be used to control the flow of the sample, allowing for precise control over the analysis process. Overall, the integration of optics with microfluidics is a powerful technique for the field of biochemical analysis. By combining the precision of optical sensing with the versatility of microfluidic systems, lab-on-chip devices can perform complex analyses in a compact and portable format, opening up new possibilities for point-of-care diagnostics, environmental monitoring, and biomedical research. While we have explored its precision and efficiency in surface ablation and the creation of optical structures, femtosecond lasers also play a pivotal role in ocular procedures. In the realm of ophthalmology, femtosecond laser technology has introduced surgeries like LASIK[131], cataract extraction, and corneal transplants. The ability to create precise incisions and tissue modifications has changed ocular surgery, enhancing patient outcomes and reducing the risk associated with traditional surgical techniques.

### 3.5.2    Hydrophobicity/Hydrophilicity

In this section of the literature overview, we explore the potential applications of the interaction between femtosecond-etched structures and a wet environment. Wettability is an inherent property of solid surfaces, closely linked with their physico-chemical attributes. This characteristic is important due to its susceptibility to chemical adjustments, illustrated by the incorporation of elongated carbon chains, or mechanical alterations using femtosecond laser techniques. The rapid assessment of material wettability involves analyzing the contact angle established by a liquid on the material's surface. Figure 3.14, inspired from [132], represents the different types of contact angles that can be encountered.
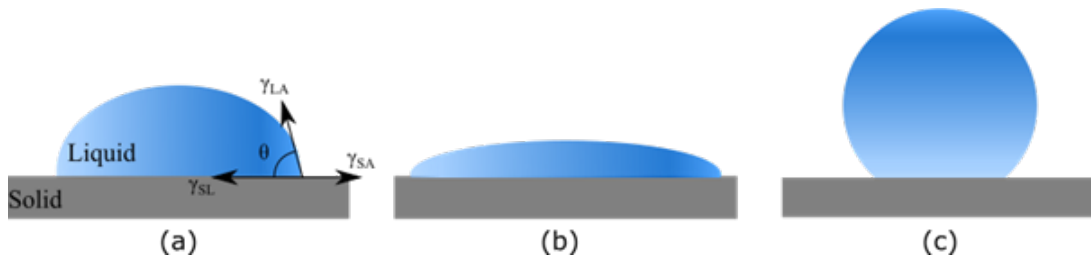


Figure 3.14: Scheme of wetting state of a liquid droplet on a solid surface. **(a)** Droplet on a flat substrate. **(b)** Droplet on a hydrophilic surface **(c)** Droplet on a hydrophobic surface.

The contact angle depends on the surface free energies existing at distinct interfaces, specifically at the solid/liquid ($\gamma_{SL}$), solid/air($\gamma_{SA}$), and liquid/air ($\gamma_{LA}$) interfaces. The conceptual framework for the contact angle finds its roots in Young's equation [133].

$$\cos \theta = \frac{\gamma_{SA} - \gamma_{SL}}{\gamma_{LA}} \tag{3.1}$$

Over time, adjustments were made to Young's formula, as it became apparent that another parameter capable of influencing the contact angle is the surface roughness. The interaction between the contact angle, surface free energy, and surface roughness (R) is encapsulated within the following equation.

$$\cos\theta = \frac{R(\gamma_{SA} - \gamma_{SL})}{\gamma_{LA}} \tag{3.2}$$

The femtosecond laser plays an important role in the construction of the different structures due to its low thermal effect, it can directly excite the material to create a plasma able to etch the material. If we are at high energy the femtosecond laser will create multiple parallel microgrooves which will induce a variety of porous nanostructures, hence a hydrophilic surface. This will change the properties of the surface of the material. In some cases of a very hydrophilic surface, an interesting phenomenon can take place. In some situation, the liquid can move uphill against gravity. Regarding hydrophobic structures, we can draw inspiration from nature. A good example of a natural hydrophobic structure is the lotus leaf. The latter has a slight shake where the liquid droplets will freely roll down away from the surface. This phenomenon is called superhydrophobicity, it is characterised by a contact angle larger than 150° but that could reach until 160°.
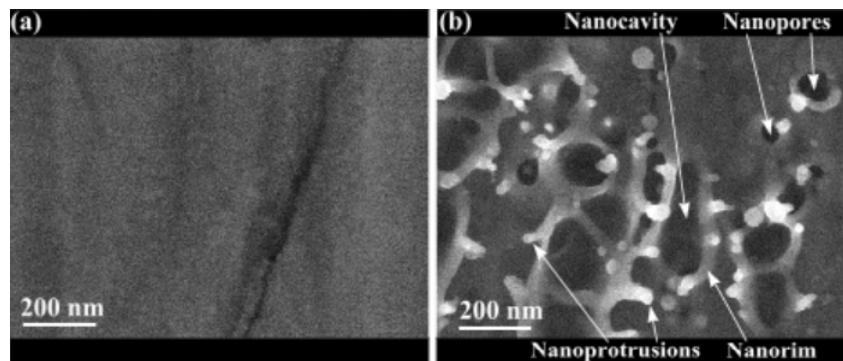


Figure 3.15: **(a)** Image of sample surface before irradiation and **(b)** nascent nanostructures induced on copper by femtosecond laser ablation at F = 0.35 J/cm2 and N = 1. Note,**(a)** does not show the same spot on the sample as in **(b)**. [134]

As it has been observed in 1997 by Barthlott and Neinhuis [135] the microstructure at the surface of the lotus leaf is in a very interesting state. It has a lot of microscale papillae with a diameter of 10 µm each randomly distributed on the surface of the leaf. These different papillae are the sources of the superhydrophobicity of the lotus leaf.

Regarding the incorporation of the femtosecond laser in the formation of this structure, the primary objective is to use high-energy femtosecond laser pulses for direct material surface ablation. Subsequently, the excess energy on the surface irradiated by the femtosecond laser can be reduced through an additional modification.
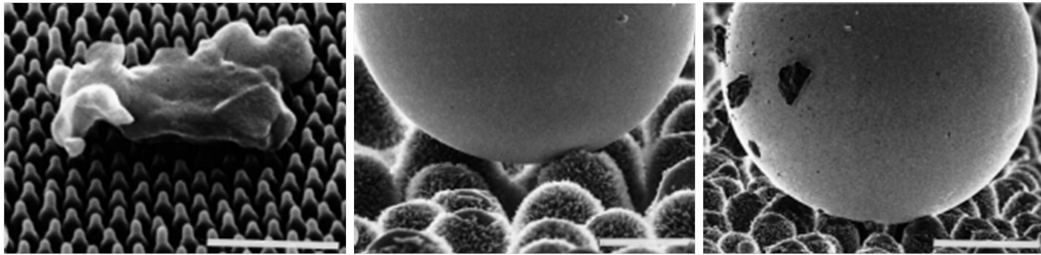
Figure 3.16: Purity of the sacred lotus, or escape from contamination in biological surfaces. [136]

This adjustment involves doping the surface with fluoroalkysilan molecules, resulting in a superhydrophobic surface with an approximate contact angle of 160°. It is important to note that the femtosecond laser is capable of producing both hydrophilic and hydrophobic structures, with the main difference being the energy levels applied during the ablation process. According to Wang [61], the creation of hydrophobic structures requires lower energy levels, typically ranging from 0.4 to 2.1 J/cm², while maintaining hydrophilic structures necessitates a higher energy combination, within the range of 2.1 J/cm² to 52.7 J/cm². This is explained in the case of the polymethyl methacrylate (PMMA) the proportion of C-O bonds versus the quantity of C=O, the polarity of the C=O is more important hence more hydrophilic. Which is why for the case of the PMMA the high densification energy gives material with a more hydrophilic surface.

### 3.5.3   Femtoprint Machine

Expanding upon the capabilities of femtosecond lasers in ophthalmic surgery and the controlled modification of surface wettability, our focus now shifts to the convergence of these applications, leading to the emergence of a technology known as Femtoprint. This technique harnesses the precision and control inherent to femtosecond lasers to fabricate intricate microstructures on surfaces. In the forthcoming discussion, we will develop its potential across a spectrum of disciplines. Ranging from engineered materials to cutting-edge advancements in medical devices.

In 2012 Yves Bellouard [4] and his team published an article called the Femtoprint project. In this article, the authors provide an account of the development of a novel, fully automated printer system integrated with a femtosecond laser. This technology unlocks the potential to apply various design methodologies, including ablation, nano-grating fabrication, and small waveguide production, all within a single transparent specimen. The femtoprint machine is compartmentalized into three distinct components: a control unit, a laser scanning system, and the laser source.

The primary objective of the femtoprint project is to establish a versatile platform capable of creating the aforementioned diverse structures with a high degree of precision.

The entire process is fully automated and governed by a computer system. In this article, they describe the different parameters for the optimization of the machine such as which repetition rate is the most suited for the best spreading of the etching agent. It describes also all the different possibilities linked to the Femtoprint machine such as micro-moulding, fabrication of integrated optics or microfluidics. In the Femtoprint project the femtosecond laser was used to create cavities that were coated with a polymer. The latter was then used for molding, once the substrate was removed. There are also presenting examples of controlled refractive index modification to create optical waveguides or voluntary birefringence.

Before using the Femtoprint machine on a transparent substrate, we must define the various laser paths on the silica glass plate. These laser paths will be created using the Alphacam software. Through this software, we have to design the different geometries of the future structures. The design of the different geometries is important because we have to anticipate the future function of the geometries, whether they are optical structures or mechanical structures. Once we've designed the geometries and figured out the function of each structure, we move on to planning the different laser paths. To create an optical waveguide, we need to make sure the laser paths overlap. This overlap is what forms a uniform optical waveguide. For mechanical structures that will be etched later, we use a fast scan through the volume of the glass plate. Knowing how to use Alphacam software is really important here because it's during the laser path design that we set the pulse energy, repetition rate, writing speed, and laser polarization. This step is crucial because once the laser paths are set, we can't change them during the printing process. The different steps linked to the alphacam software are represented in Figure 3.17.
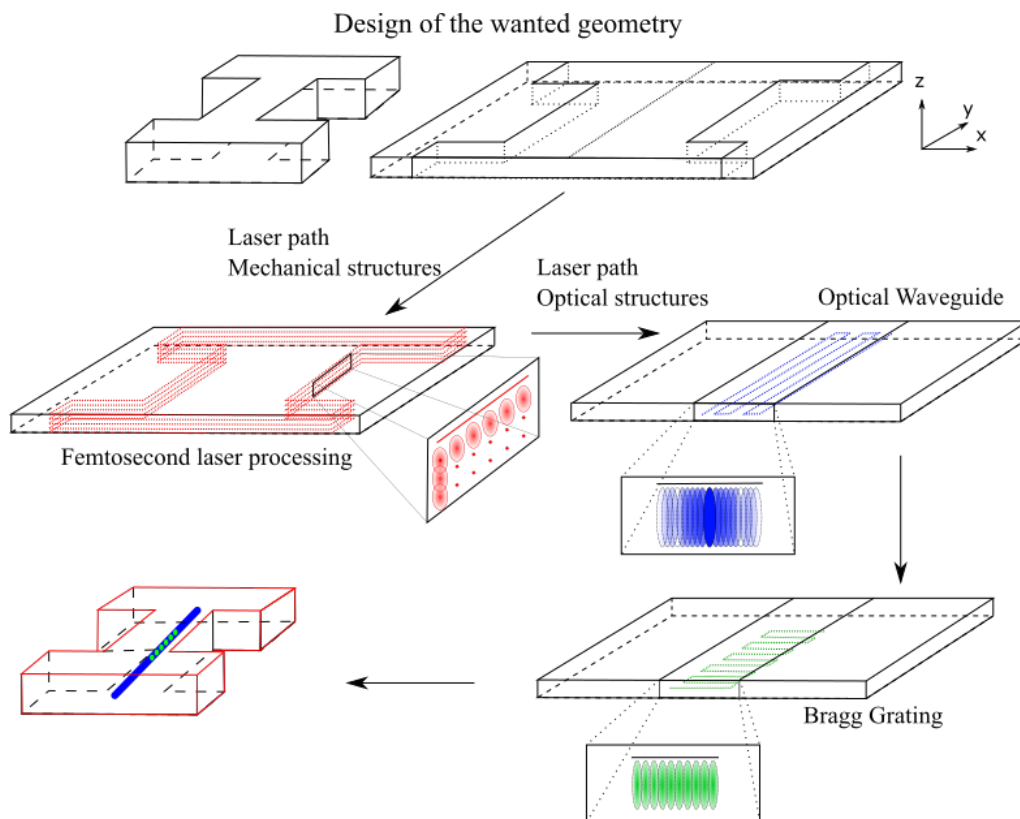
Design of the wanted geometry

Figure 3.17: Schematical representation of the different laser path that can be used in alphacam.

Figure 3.17 represents the different steps of the Alphacam software and explains how the femtosecond laser will act on the silica glass plate. We can see that there are three types of laser paths for three different structures. The first laser path is for processing to design the mechanical structures, represented in red. In this case, the energy is high and the voxels are spaced from each other due to the writing speed. Then, the blue and green laser paths represent the inscription of optical structures. For the optical waveguide, there is a strong overlap induced by a space of 0.5 µm between the different laser paths to create a homogeneous waveguide. The green laser path represents the Bragg grating, with a period that can be easily adjusted. Once we combine all this information together, we obtain a new mechanical structure with an optical waveguide and a Bragg grating within it, ready to be etched.

The femtoprint machine is composed of three different parts represented in Figure 3.18. The first part is the camera and the microscope objective, it allows the user to follow the impression. The second part is the objective dedicated to focus the femtosecond laser pulses. The final part is the moving plate, it is important to note that the femtosecond objective is fixed.
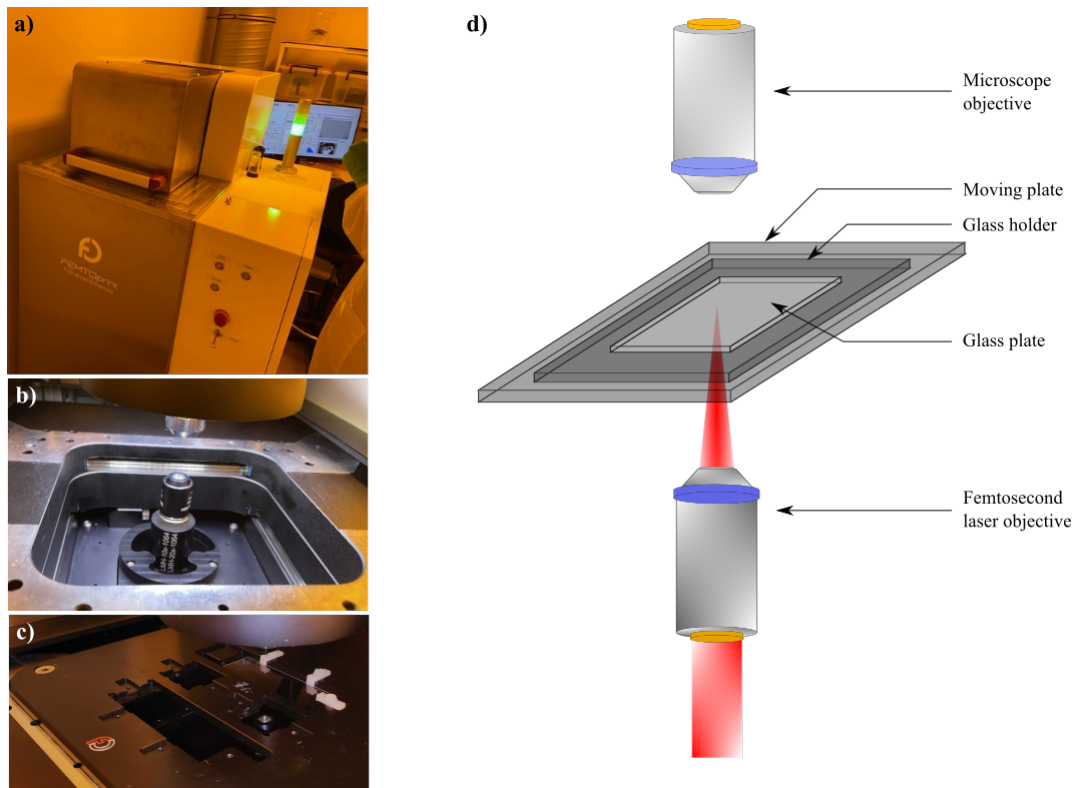
Figure 3.18: **(a)** The FEMTOprint device is used to perform the laser exposure step. **(b)** The laser objective is located at the bottom. The microscope at the top is used to calibrate the position and orient the glass substrate correctly. **(c)** The glass substrate is attached on a holder placed above the laser objective, itself fixed to a moving stage. **(d)** Schematic representation of the femtoprint machine.

In conclusion, the femtosecond laser has emerged as a powerful tool in materials science, enabling the creation of a wide range of structures with unique properties and functionalities. From photonic crystals and microfluidic devices to metamaterials and beyond, the possibilities are limitless. The ability to precisely manipulate matter at the microscale has opened up new ways for research and innovation, with potential applications across a variety of fields. The advent of femtoprint machines, which uses femtosecond laser technology, has expanded the scope of what can be achieved, allowing for the creation of intricate structures with unprecedented precision. As we continue to explore and refine the capabilities of femtosecond laser technology and femtoprint machines, we can expect to see even more exciting developments in the future.

# Chapter 4

# Experimental Results: Optical Fibre Insertion, Waveguide Integration, and Bragg Grating Formation

This chapter focuses on presenting the experimental results obtained during this PhD. We initiate our study with an investigation of the insertion process of the optical fibre into the silica glass plate. Then once we can insert the optical fibre into the glass plate we will illustrate the process of integrating a waveguide and a Bragg grating. We will examine each decision and detail the reasoning behind each choice.

## 4.1 Inscription Setup on Fused Silica Glass

The Femtoprint machine stands as the pivotal piece of equipment in this PhD. Within our research, we employ a fused silica glass plate measuring 74x26 mm, and 0.5 mm in thickness, supplied by Siegert Wafer ref T20394, with a purity ranging from 99.9998 % to 99.99995 %.

The Femtoprint process comprises several key steps. The initial phase is the fabrication of diverse structures via numerical control. To study this process in detail, we start by generating a solid model of the monolithic structure using SolidWorks software. Then, we transfer the solid configuration to a customized version of the Alphacam software, which is provided by FEMTOprint. Within the Alphacam software, we select various operations and parameters. Notably, there are several types of laser paths available, with our focus primarily directed towards the "rough" and "pocketing" options. The "rough" path is employed for vertical inscriptions covering the entire plate, while the "pocketing" path is mostly used for planar operations, especially in the creation of waveguides.

Before initiating the printing process, it is important to consider several parameters. These parameters vary due to the diverse objectives at hand, resulting in different focused energy and spacing between them. For instance, when working with the x20 objective, the recommended vertical spacing is 7 µm, and the planar spacing is set at 3 µm whereas for the x10 objective, the recommended vertical spacing is 20 µm and the planar spacing is recommended to be at 4 µm. We have decided to work with the x20 objective for the rest of our work.

The second phase of the process is dedicated to the actual printing procedure. During this stage, the primary objective is to implement the laser paths described within Alphacam onto a silica glass plate. It is imperative to acknowledge that, within the femtosecond laser-assisted etching process, a single laser can fulfil a dual role in the creation of both optical and mechanical structures. Specifically, optical components like waveguides and gratings, as relevant to our study, are created through the application of femtosecond pulse lasers. To provide further elaboration, the pulse duration is configured at 400 femtoseconds, the femtosecond laser operates at a wavelength of 1030 nm, and the numerical aperture of the objective lens (x20) is calibrated at 0.4. The voxel is designed to possess an height of 24 micrometres and a width of 1.5 micrometres.
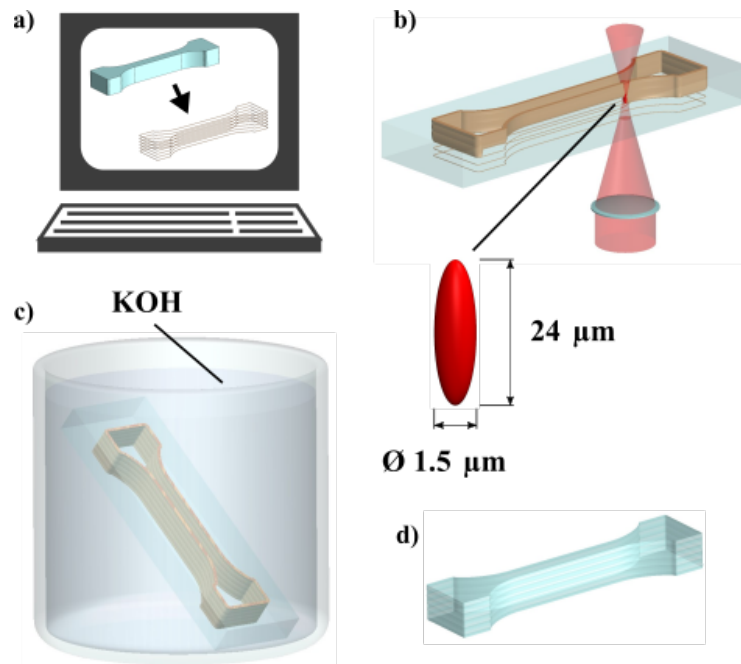


Figure 4.1: Femtosecond laser-assisted etching. **(a)** The laser path is extracted from the 3D model of the designed part. **(b)** Laser exposure step: the laser path begins at the top of the substrate and finishes at the surface in front of the laser objective. The laser exposed volume is defined by the laser path and the laser voxel dimension. The dimension is assumed according to the FEMTOprint parameters and not measured. The voxel dimension depends on the focusing conditions and laser parameters. (For representation purposes, the proportions are not accurate) **(c)** Etching step: the substrate is placed in a KOH bath at 85 °C for wet etching. **(d)** After etching, the finished part is cleaned with pure water.

Initiating an inscription with the femtoprint machine necessitates several steps. Initially, the laser is required to detect the glass plate surface, To achieve this, the femtosecond laser is operated at an energy level of 60 nJ. A sensor then detects the peak intensity corresponding to changes in the refractive index, indicating the air/glass interface. Then, through a computational process, the plate thickness is ascertained experimentally by the Femtoprint machine. Once the plate's thickness is determined, the dimensions of the desired structure are input, and adjustments in various angles are computed to optimize the inscription quality. Simultaneously, the formation of mechanical structures which require shaping, necessitates an additional wet etching procedure to remove material sections previously exposed to laser pulses. As detailed in the state-of-the-art section, the substrate is placed in a 12 M KOH bath at 85°C for wet etching.

KOH is etching at a rate of 130 µm/h to the portions that were exposed to femtosecond laser pulses, while it is only etch at a rate of 0.7 µm/h to the non-exposed areas, as represented in Figure 4.1. The non-uniform etching is an important factor to consider, as it implies that while the primary mechanical structures are being etched, the remaining portion of the glass plate is also etched but at a much slower rate. This selective etching phenomenon could potentially compromise the integrity of the optical structures if adequate safety margins are not incorporated. Hence, to limit this risk, we will maintain a 10 µm gap between the edge of the plate and the initiation of the waveguide for the remaining portion of each structure. All these different parameters are involved in the creation of the different optical structures but it is important to note that the setup for the characterisation differs in many different ways. The goal of the next section is dedicated to the different equipment for the characterisation of the optical waveguide and the Bragg grating.

## 4.2 Fabrication of Fibre Holder for Optimal Transmission

### 4.2.1 Insertion and Alignment of the Optical Fibre

This section focuses on the process of fabricating insertions for optical fibres within silica glass. The objective is to ensure both a correct optimal transmission and signal quality. We will explore the fabrication techniques and characterise the resulting structures using femtosecond laser combined with chemical wet etching. Through several experiments, we aim to control the principles and methodologies essential for creating structures that facilitate connection between optical fibres and silica glass waveguides.

To construct our sensor, it was imperative to establish a dedicated cavity to facilitate the optical fibre access to the primary structural framework. Conventionally, for such circumstances, ferrules are commonly employed. These ferrules are conical structures composed of ceramic, or metal, material that is affixed to the terminus of the optical fibre. An example of ceramic ferrules made by Thorlabs is represented in Figure 4.2.
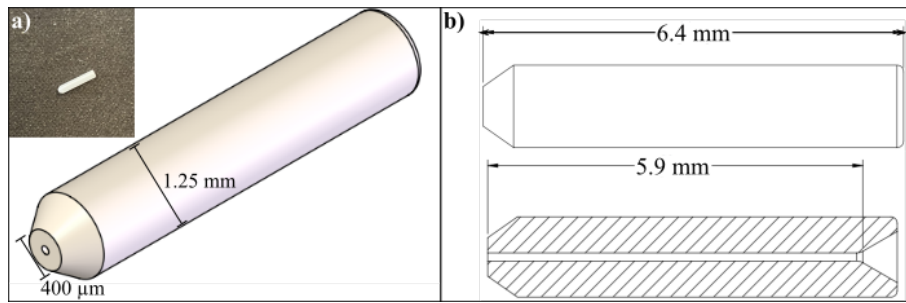
Figure 4.2: **a)** Isometric representation of ceramic ferrules. **b)** Schematic representation of the ferrules from a side view. [Thorlabs : CFLC126-10]

The fundamental purpose of incorporating these structures is multiple, the first goal is to align the fibre with the material, the second objective is to maintain the fibre in position and the last objective is to reduce the loss of signal transmission. The better alignment will reduce the loss and we add matching gel index to improve the quality of the coupling. In our development, our approach detailed the integration of these ferrules into silica glass through the creation of dedicated cavities. This strategic measure was adopted to ensure the minimal attenuation of signal integrity at the interface between the silica glass and the optical fibre's tip. We tried to directly carve an insertion for ferrules into the silica glass, aiming to optimize the optical signal within the glass itself. This carving process was executed utilizing femtosecond laser technology with chemical etching.
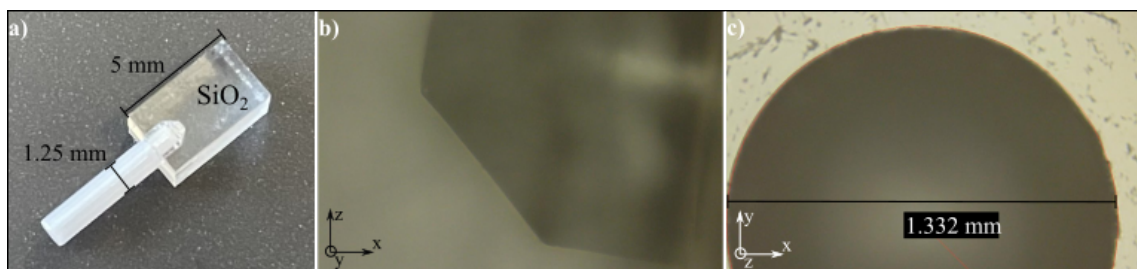


Figure 4.3: **(a)** Picture of a ceramic ferrule inserted into a 5 mm thick silica glass plate. **(b)** Microscopic picture of a ferrule holder from a top point of view **(c)** Microscopic picture of a ferrule holder from a side point of view.

Figure 4.3 illustrates the first attempt of a ferrules holder structure etched directly into silica glass, designed to accommodate conical ceramic ferrules from Thorlabs. The images provide both macroscopic and microscopic perspectives of the etched structure. As illustrated in Figure 4.3 a, the insertion pathway for silica glass was successfully achieved, with the identification of several noteworthy challenges. One issue is the time requirement for this process. Due to the structural characteristics of the ferrules and their dimensions, the etching procedure employing KOH necessitated an extended duration of over 48 hours to form the insertion cavity. It is important to remember with these large times of etching that the KOH is etching part of silica glass that has not been affected by the femtosecond laser at a rate of 0.7 µm per hour.

It means that in 48 hours 33.6 µm of the non-affected area was etched. It means that this non-selective etching could strongly affect the shape of the structure. It is an effect that we can anticipate in terms of margin of security but we cannot anticipate the exact direction of etching on the non-irradiated part.
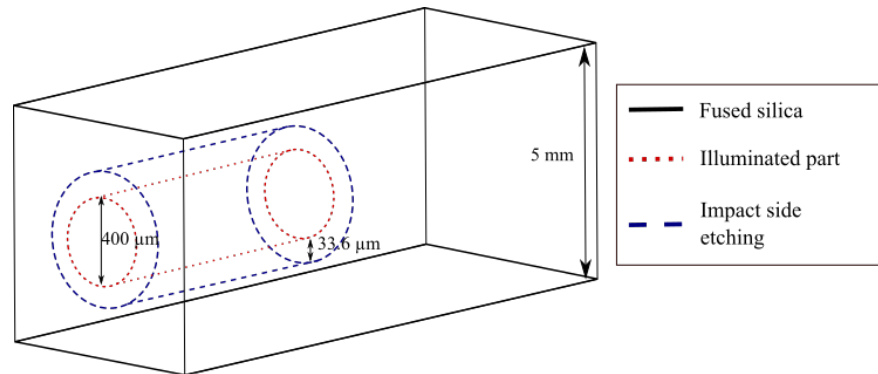


Figure 4.4: Schematical representation of the evolution of the KOH within the silica glass plate after 48 hours.

In the next phase, our attempts shifted towards reproducing the identical insertion for the ferrule into silica glass but instead with a departure from the lateral orientation. Specifically, instead of inscribing the ferrule holder in silica glass as represented in Figure 4.5 a, we tried to inscribe the ferrule holder perpendicular to the surface of the glass plate, as illustrated in Figure 4.5 b. While the visual representation may appear similar, it conceals several crucial considerations. The non-circular shape of the voxel introduces a higher laser path length due to the voxel's thickness.
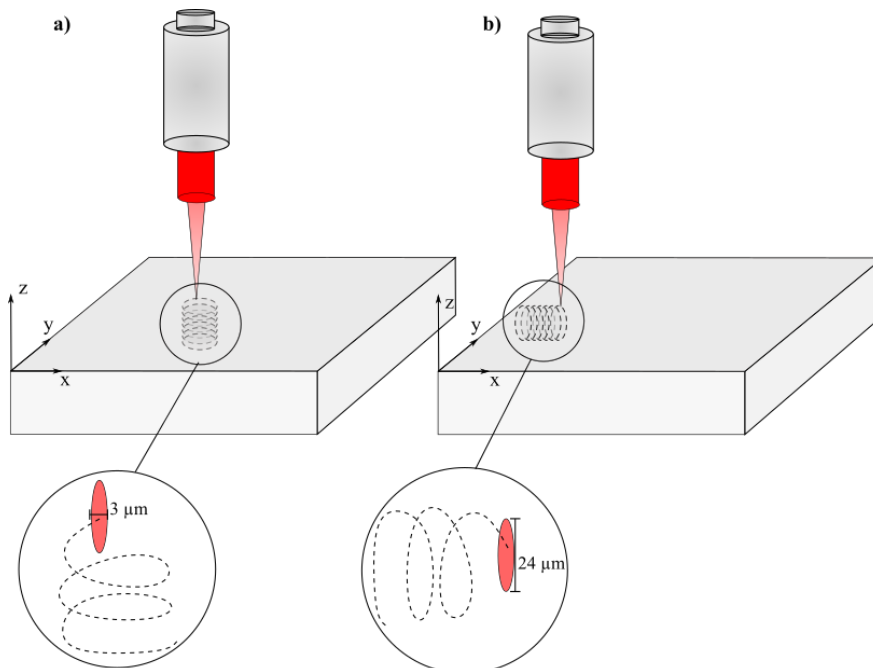


Figure 4.5: Schematic illustration depicting the laser inscription on the silica glass **(a)** parallel to the laser emission. **(b)** Perpendicular to the laser emission.

This results in extended printing and etching durations, impacting the overall process. Nevertheless, we have tried to inscribe ferrule holder geometry while taking into account the different modifications of the voxel and we have obtained different structures described in Figure 4.6.
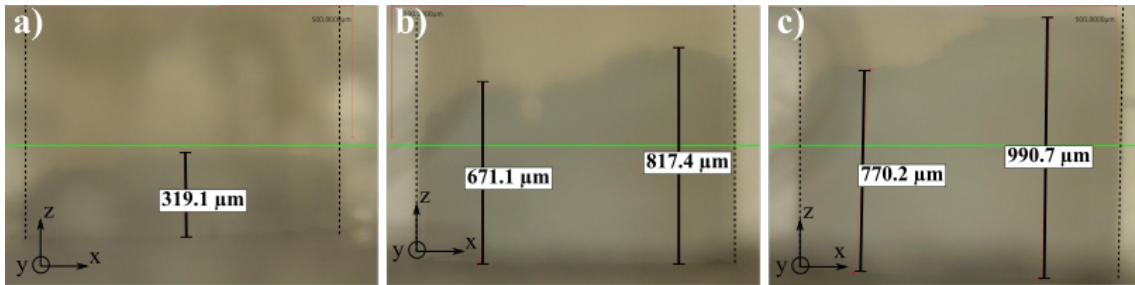


Figure 4.6: Microscopic pictures of the evolution of the KOH after different times of chemical etching: **(a)** 48 h, **(b)** 60h, **(c)** 96h.

Figure 4.6 represents from a planar point of view. The evolution of the chemical etching in the structures conceived for the ferrule holder. Even after 96 hours, the ferrule holder remains incomplete. While this approach is a possibility, the etching time makes it impractical for our intended purposes. Given the multitude of experiments planned, a process that demands more than 96 hours for each iteration would pose significant logistical challenges. An alternative method will be thought to meet the experimental timelines effectively.

The other challenge is due to the high numerical aperture associated with the x20 objective (0.4) limiting its capability to print on a glass plate thickness superior to 0.5 mm. So even if we can create a ferrule holder we either have to bend the waveguide, or we have to create the entrance of the ferrules and make it centered close to the edge of the glass plate so that we can inscribe directly with the x20 objective which is limited at a 500 µm thickness. The decision was made to discontinue this particular aspect of the design and explore an alternative approach more suitable for a 500 µm thick glass plate. The alternative is not to use the ferrule and instead insert directly the optical fibre within the silica glass structure.

### 4.2.2   Improved Fibre Holder Design

The second approach is a direct insertion of the optical fibre in direct contact with the silica glass. This design features a square cavity with dimensions matching the size of the optical fibre cladding. We decided to inscribe square cavities because they were easier to print and faster to etch. In our initial efforts, we tried creating a design with a single closed cavity alongside an open one. However, a significant issue was that the optical fibre consistently dislodged from the primary structure. In response, we decided to enhance the stability by replicating the structure, leading to the configuration shown in Figure 4.7, comprising a total of three different parts.

The first structure (I) is a cavity created for the insertion of the optical fibre, represented in blue in Figure 4.7 a. The dimensions are adapted to a 126 µm diameter optical fibre.
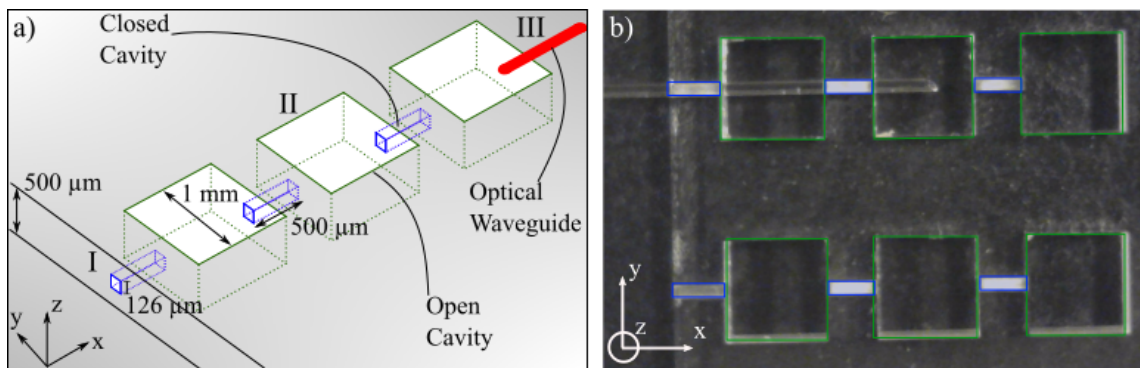
Figure 4.7: **(a)** Scheme of ceramic ferrules inserted into a 0.5 mm thick silica glass (74x26 mm). **(b)** Microscopic picture of a ferrules holder.

Then the fibre enters an open cavity (II) going through the entire glass plate, represented in green in Figure 4.7 a. This kind of cavity has two goals, the first one is to improve the speed of KOH to accelerate the etching. The second objective is to facilitate cleaning and removing pieces of broken fibre ends if it applies during insertion (bad insertion). As represented in Figure 4.7 the structure I and II are reproduced three times each in total. At the end of the last open cavity, the waveguide (III) is aligned and centred with the cavity. To summarize, the fibre is maintained and guided with the etched tunnels or capillary (I) while the cavities (II) are used for faster etching and cleaning. The advantages of this structure are that it is easy to print, it is a seven-hour etching only and it also allows an alignment of the optical fibre directly with the waveguide. The main drawback of the structure is that at the insertion we may have a big insertion loss due to the damaged fibre while searching the entrance and the second drawback is the fact that the fibre is not fixed to the surface of the glass so we may have to use glue and/or index matching gel to be sure of the transmission of the signal.

In summary, we have accomplished the construction of a structure capable of holding and aligning the optical fibre with an optical waveguide. This structure involves a printing time of 1 hour followed by an etching process lasting 7 hours. The open cavities measure 1 mm in length, while the closed ones are 0.5 mm long, resulting in a total structure length of 4.5 mm considering the presence of three of each type. We decided to repeat the structure three times due to the stability they provided. With one or two repetitions, the optical fibre was not stable enough.

The insertion of the fibre emerges as the most intricate aspect, suggesting a potential enhancement by reshaping the closed cavities into cones rather than cubes. This alteration in shape could potentially facilitate the insertion of the optical fibre, streamlining the overall assembly process.

# 4.3   Inscription of Optical Waveguides

Our next task involves identifying the optimal parameters for inscribing the waveguide. The primary goal of the optical waveguide is to guide light in various directions, the most known example remains the optical fibre. In reviewing the literature, we have encountered various methods for inscribing optical waveguides [137]. One can inscribe a waveguide in glass with two types of techniques either by a thin deposition of a physical or chemical structure such as sol-gel [138] process or the chemical vapour deposition [139]. A modification of the refractive index can also be directly induced. The femtosecond laser inscription is one of those techniques with UV writing or ion exchange.

## 4.3.1   Inscription Parameters for the creation of Waveguides

Patterning optical elements such as waveguides or Bragg grating relies on the increase of the refractive index due to femtosecond laser densification. For optimal parameters for waveguide inscription, our focus narrows down to minimizing the energy pulse. To determine this critical threshold, we have embarked on constructing a comprehensive map that establishes a correlation between the evolution of energy and speed on their capacity to inscribe on silica glass. The goal is to explore diverse paths with varying spatial parameters, discerning when the femtosecond laser triggers inscription on the silica glass plate. For qualitative analysis, our research employs a variety of microscopes, each possessing distinct characteristics. A significant portion of the quantitative analyses were conducted employing a VK-X200 3D laser scanning microscope from Keyence. This particular microscope is equipped with four distinct objectives, each featuring a unique numerical aperture. The principal advantage of this Keyence microscope, as illustrated in Figure 4.8, lies in its capacity to facilitate observation via laser illumination UV light. The employment of this laser proved valuable in the examination that cannot easily be seen by the naked eye.
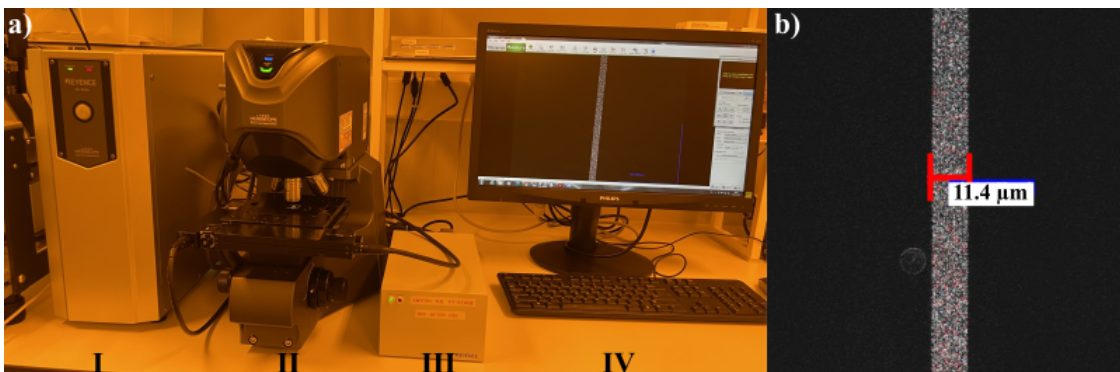


Figure 4.8: **(a)** Picture of the Keyence microscope setup comprising into four different parts I) Mainframe computer II) Keyence microscope III) Axis controller IV) Central monitor. **(b)** Picture of a waveguide in silica glass observed through the microscope with a UV laser used for observation.

The Femtoprint machine uses an energy pulse of 60 nJ to assess the location of the surface of the silica glass plate. To that aim, the Femtoprint machine uses the difference of refractive index between air and the fused silica glass. We also know from the literature that the increase of the refractive index and the densification of the silica glass is induced at a low energy pulse [140]. Thus, we deduce that the energy required for actual waveguide inscription surpasses this baseline of 60 nJ. We then designed a map comprising 42 squares each measuring 100 µm. Within this matrix, pulse energy fluctuates between 100 and 160 nJ, while writing speed spans from 1 to 60 mm/min we did maintain a repetition rate of 1 MHz to stay in the recommended parameters by the Femtoprint industry. This systematic approach is anticipated to find the minimum pulse energy needed for initiating successful inscription. Figure 4.9 represented below is a schematic representation of the map with two microscopic pictures to give us an idea of how the inscription looks like. The blue squares represent a succession of laser paths each spaced of 4 µm whereas the grey part represents the absence of inscription. As depicted in Figure 4.9, it becomes evident that the energy pulse starts influencing the surface of the fused silica plate at 130 nJ. While a more granular search within the range of 120 to 130 nJ might reveal the precise inscription energy pulse, it is essential to acknowledge the regular calibration requirements for the femtosecond laser. It is possible that an inscription took place but we are not able to observe it with the kind of microscope we have available. The calibration process can introduce variability to the input energy. Therefore, to account for potential fluctuations and ensure reliability, we have chosen to set the energy for waveguide inscription at 130 nJ. This calibrated energy level will serve as the primary parameter for the inscription of the optical waveguide. The next step is to find the optimal space between the different laser paths.
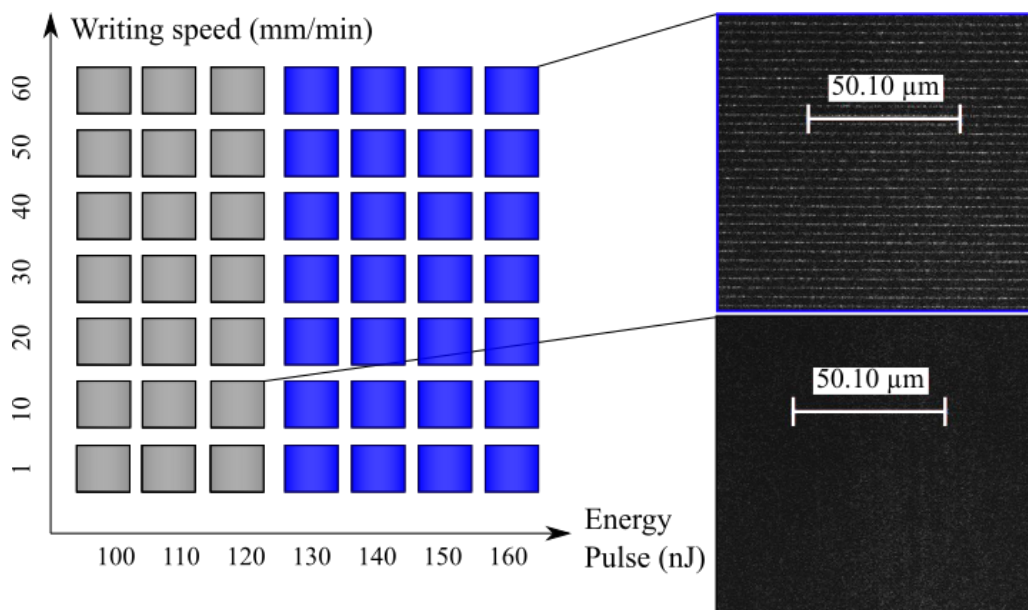


Figure 4.9: Picture of a mapping of the evolution of the energy pulse as a function of the writing speed. The blue square represents a successfully inscribed square whereas the grey square represents the absence of any inscription.

For the creation of a homogeneous waveguide we need to induce an overlap between the different laser paths. In the next phase, we have chosen to conduct multiple parallel inscriptions, each featuring distinct spacing between them but for each of them the inscription is at the same depth. The initial setting for the induced parameter in the mechanical inscription with the space recommended by Femtoprint for the inscription of the mechanical structure was 3 µm, so we lower this space at 2.5, 2.0, 1.5, 1.0 and 0.5 µm, while maintaining a consistent energy level of 130 nJ and a deliberately slow speed of 1 mm/min. This decision is based on the fact that we want to obtain the most homogeneous possible optical waveguide. To find it experimentally we have tried different spaces. This evolution is represented in Figure 4.10, the goal is to find which spacing will give us the most homogeneous waveguide.
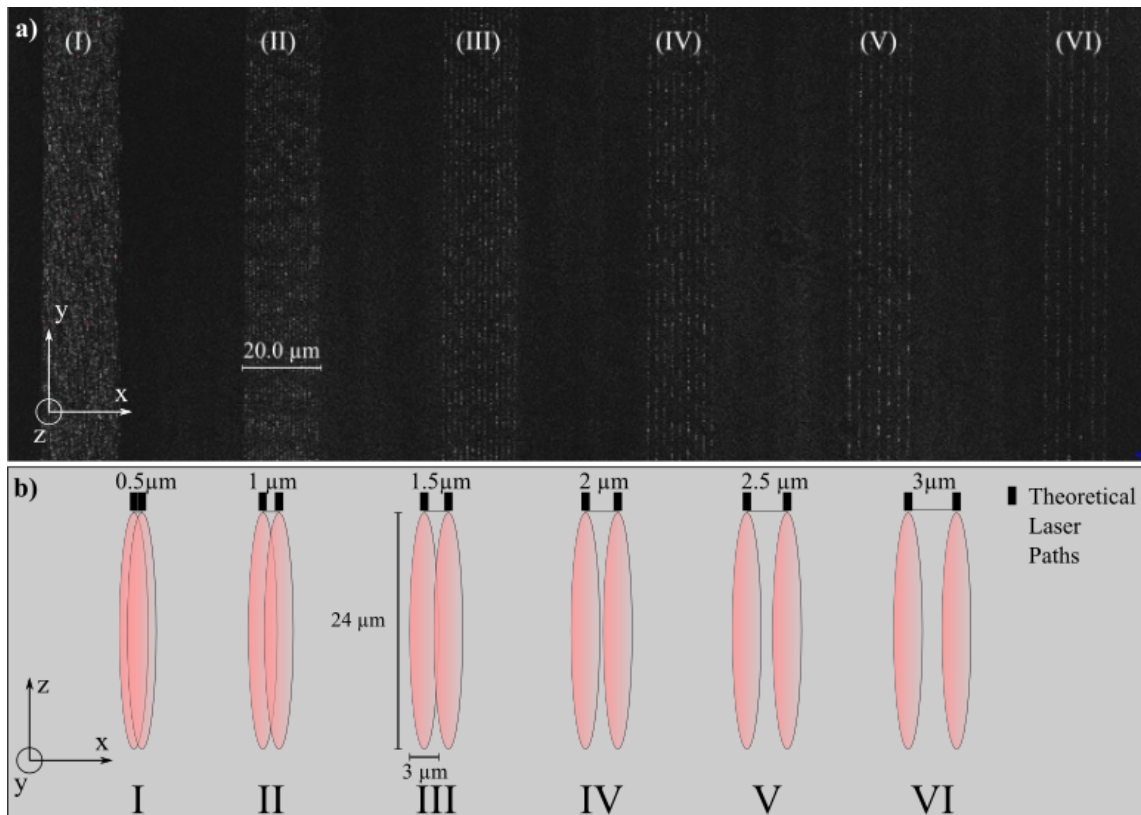


Figure 4.10: Microscope picture of the different waveguides inscribed with different spaces of pocketing. (I) 0.5 µm, (II) 1.0 µm, (III) 1.5 µm, (IV) 2.0 µm, (V) 2.5 µm, (VI) 3.0 µm.

In Figure 4.10, the laser path exhibits homogeneity when the spacing between the different lines is set at 0.5 µm. This observation led us to adopt a 0.5 µm spacing for all the waveguides in our study. We attempted to reduce the spacing between the laser paths further, but this did not result in any improvement in homogeneity. Once we obtained the first parameter for the waveguide, the next step involves deducing the optimal inscription pattern based on the type of inscription.

### 4.3.2 Design of the waveguide pattern

As previously emphasized, the Femtoprint machine operates as an automated system, where each inscription is pre-defined before initiating the printing process and remains unalterable during execution. Among the various available operations, our focus will be directed towards two specific techniques: the planar pocketing inscription and the helicoidal rough inscription, visually depicted in Figure 4.11. These chosen methodologies will play a crucial role in shaping and structuring our optical waveguide.
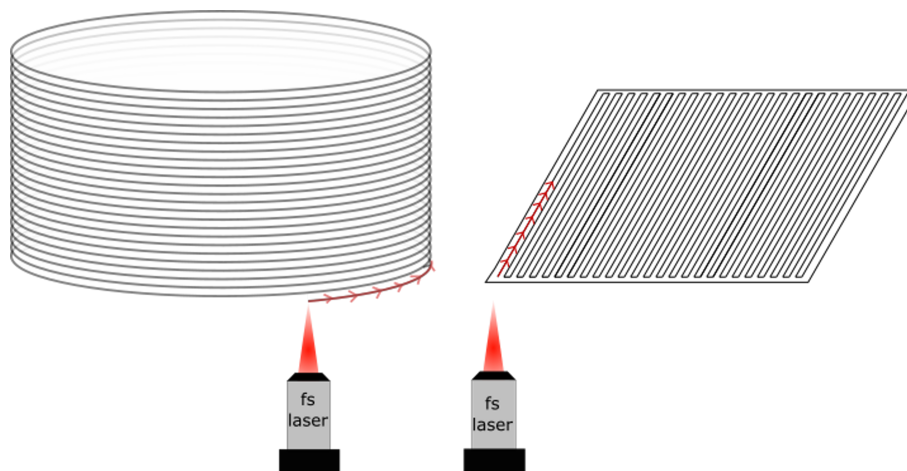


Figure 4.11: Schematic representation of the helicoidal inscription of the femtosecond laser (left) and of the planar pocketing inscription of the femtosecond laser (right).

The significance of the planar pocketing and helicoidal rough inscriptions lies in their crucial role in shaping the optical waveguide. The specific configuration of these laser paths has a direct impact on the induced types of defaults or imperfections in the waveguide. Choosing the optimal structure cannot only rely on a microscope analysis in this scenario. Therefore, in the upcoming section, we plan to characterise the waveguide. Through this characterisation process, we aim to determine which of the two laser path configurations is most effective for signal transmission and which one induces the least insertion loss.

## 4.4 Characterisation of the waveguide signal

Firstly, we aim to compare the pocketing waveguide and the helicoidal waveguide to determine which is better suited for our specific requirements and which one results in the minimal insertion loss. Secondly, we seek to assess the quality of the waveguide in facilitating the transmission of a signal before adding a Bragg grating. These dual objectives are key points in guiding our selection and optimization processes for an effective and efficient optical waveguide.

### 4.4.1    Characterisation of the insertion loss

The waveguides were characterised with an InfraRed (IR) light. To achieve this, we will conduct a series of transmission measurements, with the aim of identifying the most effective approach in terms of measurement quality. The initial step involves obtaining a baseline measurement, specifically a fibre-to-fibre measurement. This baseline measurement provides us with the highest possible value, taking into account the characteristics of the source and optimal experimental conditions.

Proceeding from this, the next phase involves assessing the signal quality using both the helicoidal and planar waveguide configurations. This comparative analysis aims to estimate the loss in quality between the two inscription methodologies, thereby facilitating the selection of the more optimal approach. Through this evaluation, we intend to make an informed decision regarding the preference for either helicoidal or planar waveguide inscriptions based on their respective signal quality.
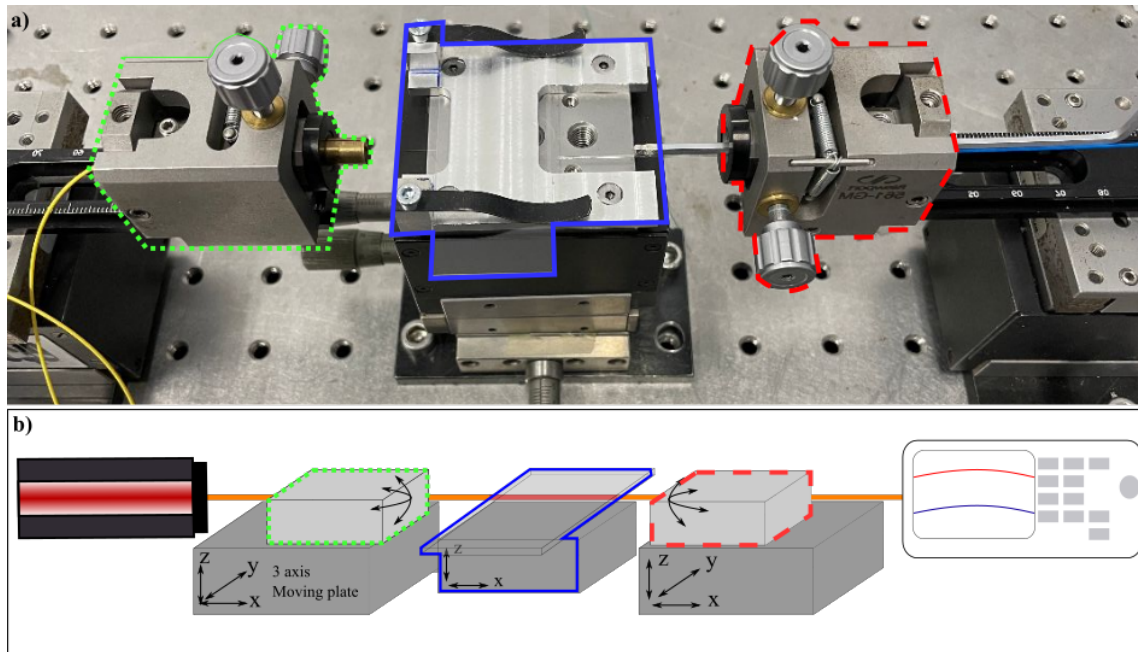


Figure 4.12: Setup Spectrum analysis of signal transmission curves across varied waveguide configurations.

The fibre is positioned on a two-axis translation stage, while the fibres for input and output fibre to fibre are mounted on three-axis stages. For quantitative characterisation, the setup in Figure 4.12 enables the determination of signal transmission quality by comparing the output optical power with and without the waveguide between the two butt-coupling fibres. To limit parasitic reflections, index matching gel is applied at both input and output and align with micrometer alignments platforms. The silica substrates are used without polishing; therefore, this characterisation step allows for the determination of relative transmission losses, which accounts for losses due to unpolished side of the glass plate. Figure 4.13 illustrates the transmission values for a 26 mm long waveguide.
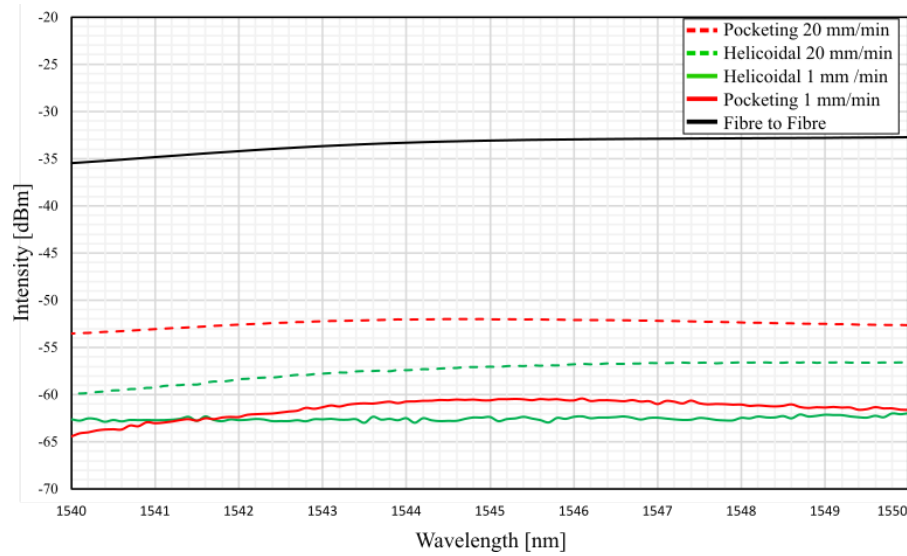
Figure 4.13: Spectrum analysis of signal transmission curves across varied waveguide configurations.

Considering the intensity through the butt-coupling fibres without the waveguide (-35 dBm), sample pocketing at 20 mm/min exhibits the lowest losses, determined to be 2.2 dB/cm. It is important to take into account that in this situation all the tested waveguides have the same length (26 mm), and were unfortunately only tested once, meaning we are not able to observe the variations of the measurements of these waveguides. As previously mentioned, this value is overestimated due to the unpolished substrate edges. However, in comparison to other waveguides and considering the transmission microscope characterisation of the samples, we conclude that the pocketing design (planar) with a high scanning speed (20 mm/s) is better suited for producing homogeneous waveguides. Several critical insights can be acquired from the spectral analysis. Firstly, there is a notable quality gap of at least 20 dB between the fibre-to-fibre connection and the various waveguides, reaching a gap of 30 dB for the 1mm/min waveguide. Upon closer examination, at a writing speed of 1 mm/min, the choice of inscription method does not significantly influence waveguide quality. However, at a higher inscription speed (20 mm/min), differences emerge. Notably, the pocketing method yields the waveguide with the smallest deviation from the fibre-to-fibre connection. Based on these observations, the decision has been made to adopt the pocketing method for inscription, instead of the helicoidal method.

## 4.4.2 Characterisation of the signal transmission quality

In the course of this doctoral research, we have employed various lasers and spectrum analyzers. Our analytical approach encompasses two distinct modalities: reflection-based analysis and transmission-based analysis. In the case of the reflection measurements to obtain the response, we need a circulator. It will transmit the signal reflected by the Bragg grating.

Most of the characterisations was made with a FibreSensor Bragg meter (Fibresensing FS2200) which has a circulator incorporated into the complete equipment. But in some other situations, we had to use an external circulator coupled with a broadband light source and then directly connected to the Optical Spectrum Analyser of Yokogawa (Model AQ6370D). For the transmission measurements, the setup is really simple we used an incoming broadband source linked directly to the Bragg grating and then connected to the optical spectrum analyser. The setup for the reflection measurements is represented in Figure 4.14.
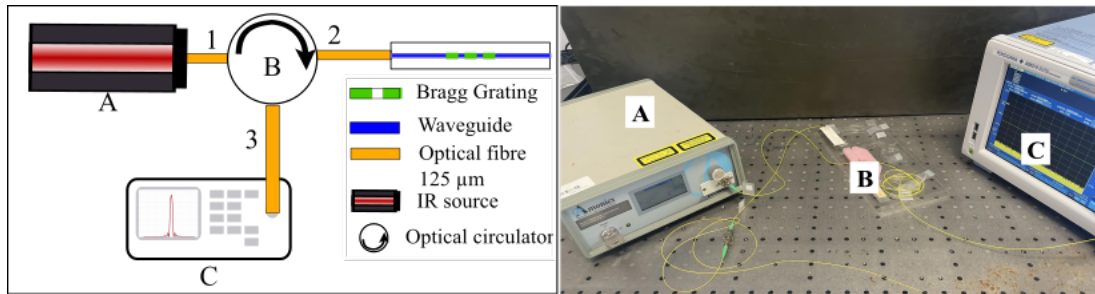


Figure 4.14: Schematical representation of the reflection set up (left) and picture of the reflection setup (right). A: Optical source, B: Circulator and C: Optical spectrum analyser.

Now that the optical waveguide has been successfully fabricated, the next crucial step is to assess its limits to transmit a Bragg grating signal. Initially, three distinct Bragg gratings were inscribed onto an optical fibre, a process facilitated by the resources provided by the Noria at the University of Mons. These three Bragg gratings were deliberately engineered with varying periods and lengths. Unfortunately, we do not know the exact length of those gratings made with the Noria system but we do have their spectrum. Subsequently, the transmission intensity was meticulously measured. The objective behind this measurement was to establish an initial reference point for energy evaluation. After recording these measurements during the transmission phase we estimated the intensity of the Bragg peak. Then the optical fibre was intentionally severed after the Bragg grating. Then the same three optical fibres containing the different Bragg gratings were once again measured in transmission, but instead of being connected directly to the Spectrum analyser, they had to pass through the glass plate and our waveguide. It is worth noting that the primary focus of this experimental setup was not to quantify insertion loss but rather to gauge the propagation loss through the integrated optical waveguide. The results are represented in Figure 4.15.
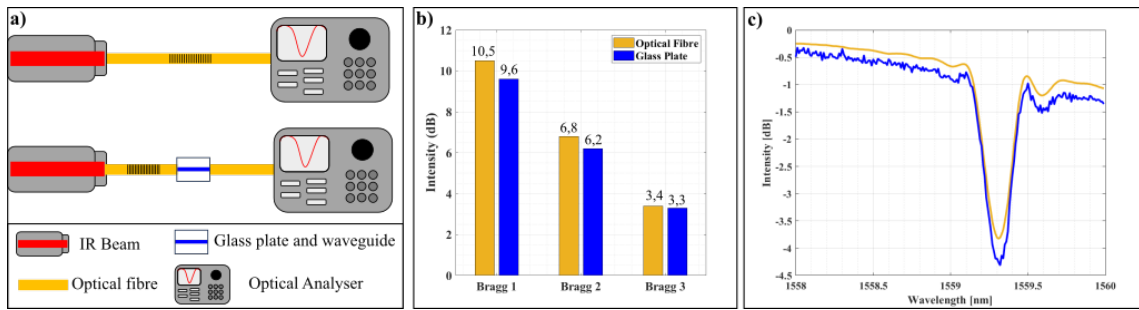
Figure 4.15: **(a)** Schematic representation of the different setups put in place for the characterisation of the Bragg grating in transmission. **(b)** Bar chart representing the different intensities as a function of the signal transmission through the optical fibre and the glass plate.**(c)** Spectrum obtained for the difference of transmission in the case of the third Bragg.

In each instance, the observed transmission rate exceeded the threshold of 90%, indicating that more than 90% of the signal successfully goes through the entire waveguide. This high transmission efficiency affirmed the suitability of the chosen waveguide for linear signal propagation. Consequently, we have decided to consistently employ this waveguide for our subsequent experiments, given its demonstrated efficiency in maintaining signal integrity during straight-line transmission. With the waveguide's performance validated, our focus then shifted to the inscription of a Bragg Grating within the silica glass plate.

## 4.5 Inscription of Bragg Gratings

As previously explained, the Bragg grating involves a periodic modification of the refractive index inscribed into the core of the waveguide. This regular deformation gives rise to two signals: a transmitted signal and a reflected signal. The objective of this section is to present and explain various studies conducted on the Bragg grating how it works and how it can be used. In this section, our experiments involve the direct inscription of a Bragg grating within an optical fiber, followed by its inscription into a silica glass plate. We inscribed the Bragg grating using an energy pulse that is slightly higher than that used for the optical waveguide, specifically at 150 nJ. To ensure successful deposition, we also reduced the writing speed to 15 mm/min for the Bragg grating inscription.

### 4.5.1 Inscription of a Bragg grating within an optical fibre

Given that the optical fibre stands as a reference waveguide, any challenges encountered in Bragg grating inscription would be attributed to the capabilities of the femtoprint machine. This investigation seeks to establish the potential for integrating Bragg gratings directly into optical fibres through the application of femtosecond laser technology.

The process of inscribing a Bragg grating within an optical fibre presented a set of challenges, particularly concerning the precise localization of the optical fibre core. In the femtoprint machine, the ability to detect the surface is essential for creating diverse angles from which the inscription initiates. However, when attempting to secure the optical fibre directly onto the glass plate, two primary issues emerged. Firstly, achieving an accurate localization of the optical fibre core proved to be challenging. Secondly, maintaining a perfectly straight line along the x-axis posed difficulties due to irregularities when placing an optical fibre directly on the glass surface.
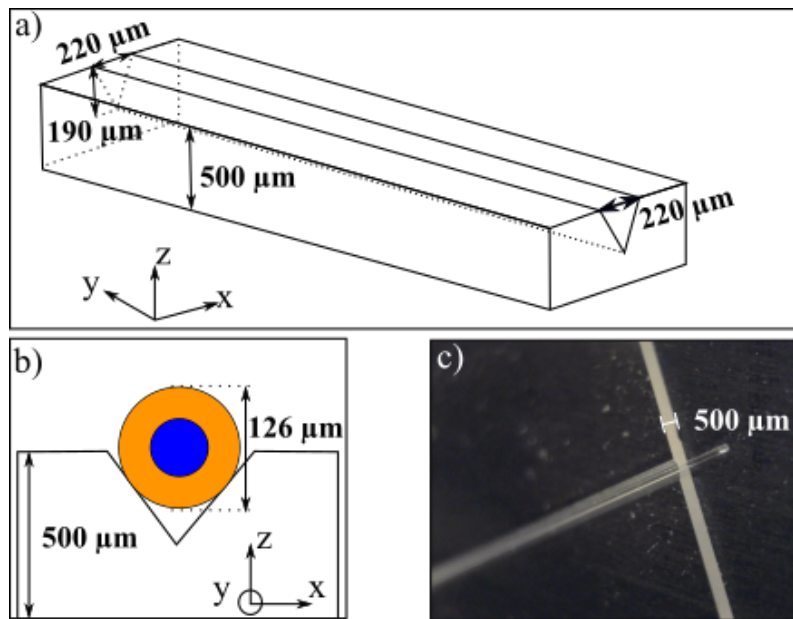


Figure 4.16: **(a)** Schematic representation of the V-groove from an isometrical perspective. **(b)** Schematic cross-section representation illustrating the positioning of an optical fibre within the V-shaped groove. **(c)** Actual photograph depicting an optical fibre securely placed within a V-groove.

To address these challenges, a strategic decision was made to etch a V-shaped groove directly into the glass plate. This groove serves a crucial role in guiding the optical fibre in a straight line at a known depth. By incorporating this groove, we aim to overcome the challenges associated with core localization and angle alignment that arise when placing the fibre directly on the glass surface. The V-shaped groove provides a stable and controlled environment, ensuring that the optical fibre remains in a straight line, thus enhancing the precision and reliability of the inscription process. This strategic modification aims to optimize the overall success and accuracy of Bragg grating inscription within the optical fibre using the Femtoprint machine. The first version of the V-shaped groove is represented in Figure 4.16. Upon closer examination, a drawback emerged in the form of opacity caused by chemical etching on the silica glass plate. This opacity occurs in areas where the laser has previously affected the surface, making it impossible for the laser to inscribe a second time in the same location after chemical etching.

This limitation was particularly evident in the V-groove region and it can be observed in Figure 4.16. c). To address this issue, a modification to the structure was implemented. An open cavity was introduced in the middle of the V-groove, ensuring that the entire optical fibre remained accessible, as represented in Figure 4.17.
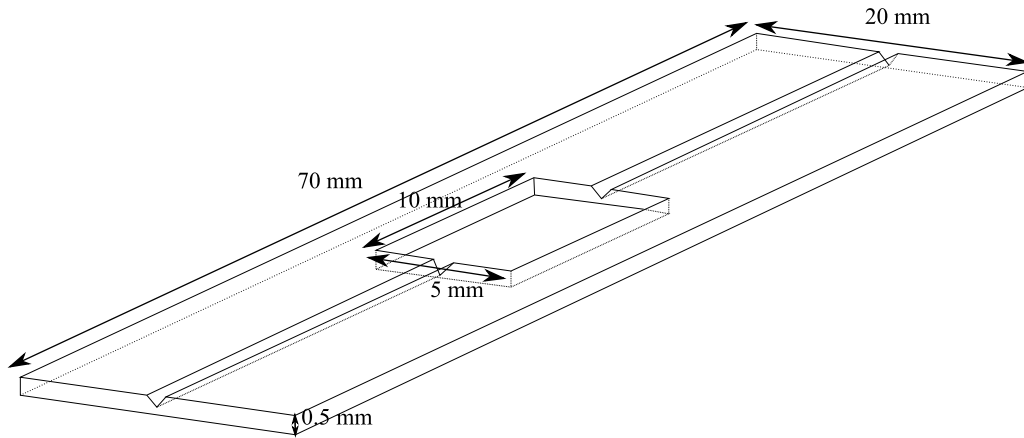


Figure 4.17: Schematic representation of the open V-groove from an isometrical perspective.

This adjustment aims to overcome the opacity-related challenges, allowing for the successful inscription of the laser at any position, even after chemical etching, and thereby enhancing the effectiveness of the inscription process. Once we corrected this default we started to inscribe on the optical fibre. To be sure to reach the core of the optical fibre and obtain a signal we decided to do a plane-by-plane Bragg Grating slightly larger than the core. It is important to note that for these results we connected the optical fibre directly to the Bragg sensors 4.18. a). The setup, is schematically represented in Figure 4.18 c). and the results obtained are represented in Figure 4.18 b-d).

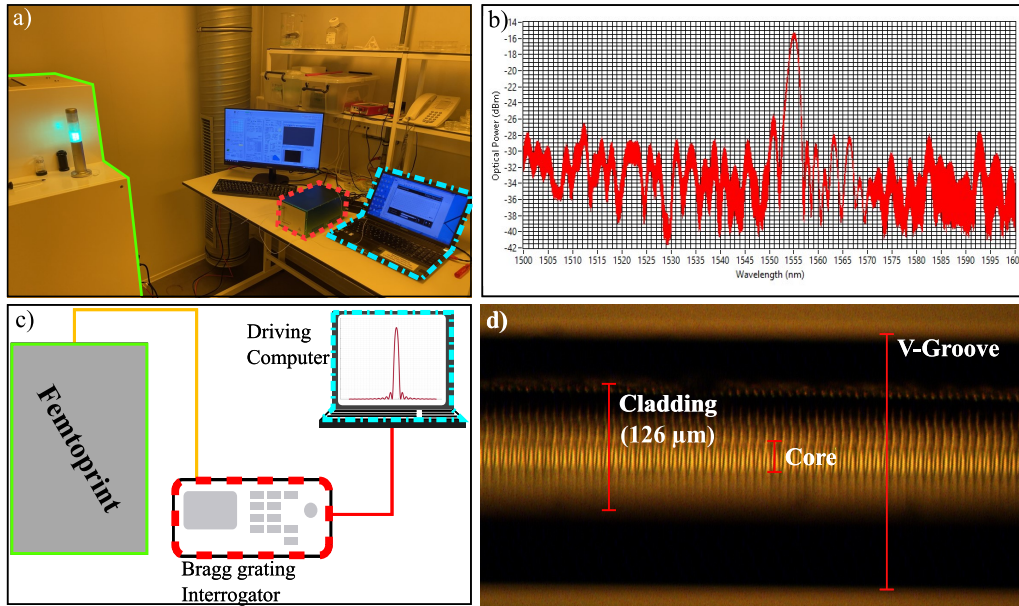Figure 4.18: **(a)** Photograph depicting the optical fibre alongside the computer interfaced with the Femtoprint machine. **(b)** The reflected spectrum of the Bragg grating obtained through the inscription using the V groove. **(c)** Schematic representation illustrating the setup for the inscription process. **(d)** Microscope image capturing the layer-by-layer Bragg grating inscribed into the optical fibre. NB: 1) The yellow colour is due to the light condition of the clean room. 2) The poor quality of the spectrum results from the fact that it is a picture of a spectrum and raw data were not recorded.

The spectrum of the Bragg grating obtained with the Femtoprint in Figure 4.18. b. serves as a reference for subsequent Bragg gratings discussed in this manuscript. It exhibits two distinct components: the predominant noise and the emerging peak. The Bragg wavelength is determined as the wavelength corresponding to the maximum intensity of this peak. Alternatively, it is possible to associate the Bragg wavelength with the centroid of the spectrum and designate it as the Bragg wavelength. In this particular instance, a pulse energy of 150 nJ and a period of 2.12 µm was applied, resulting in a 4th-order Bragg grating. Once achieved, the intensity of this Bragg grating is of 15 dB marks a promising starting point, yet there is room for improvement.

The size of the inscription area plays an important role in signal quality. As depicted in Figure 4.18. d, the Bragg grating extends beyond the core into the entire cladding, this could damage the signal quality but we did not try to characterize it. To enhance both the signal quality and the overall optical response, a reduction in the size of the inscription area is a potential avenue for improvement. After receiving training from Femtoprint engineers, we acquired the skills to calibrate every adjustment angle required for the precise inscription of a Bragg grating on a silica glass plate. Before each inscription, the Femtoprint machine performs calculations to determine the exact location of the glass plate surface, creating a grid of the surface that will undergo inscription.

This grid extends to four distinct points, as illustrated in Figure 4.19. At these points, the machine calculates the surface location, allowing for the determination of tilted angles $\alpha$ and $\beta$.
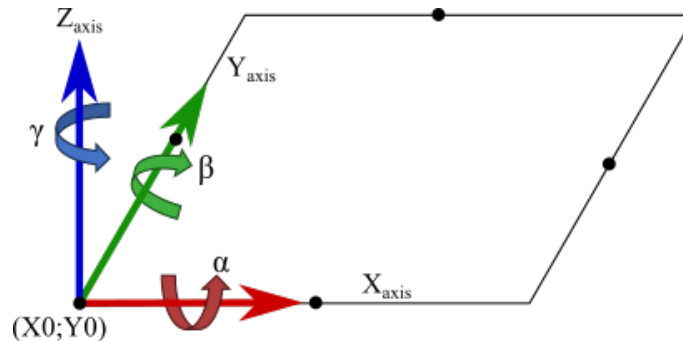


Figure 4.19: illustration of the various angles adjustable within the Femtoprint process.

However, achieving precision in the inscription on an optical fibre necessitates an additional angle, $\gamma$, calculated using two other points. This $\gamma$ angle is particularly important for maintaining a straight line along the x-axis while targeting the core of the optical fibre. The calibration of these angles ensures the accuracy and effectiveness of the Bragg grating inscription process. Addressing the issue of inscription depth, it is noteworthy that the Femtosecond laser is responsive to changes in refractive index. With the Femtoprint machine we can accurately identify the interface between two different refractive indices. Knowing this parameter, we were able to inscribe the Bragg grating more accurately on the optical fibre taking into account the difference between the core and the cladding. Using these two parameters facilitates a more precise and localized inscription of the Bragg grating, allowing for direct targeting of the optical fibre core. This approach yields a refined and well-defined response from the Bragg grating inscribed into the optical fibre, represented in Figure 4.20.

The spectral response serves as conclusive evidence of our capability to inscribe a Bragg grating directly into the core of the optical fibre. The significant dB response not only underscores the importance of traversing along the x-axis but also emphasizes the criticality of understanding the depth of the substrate being inscribed. Having successfully mastered the inscription of Bragg gratings into optical fibres, our subsequent objective is to extend this proficiency to the direct inscription of Bragg gratings into the silica glass substrate.

### 4.5.2 Inscription of a Bragg grating within a glass plate

In this section, we attempt to integrate the three primary structures outlined earlier. We incorporate an insertion structure to enhance the alignment precision of the optical fibre with the optical waveguide inscribed in fused silica. Furthermore, within the core of the optical waveguide, we introduce the integration of a Bragg grating to augment the overall functionality and performance of the system.
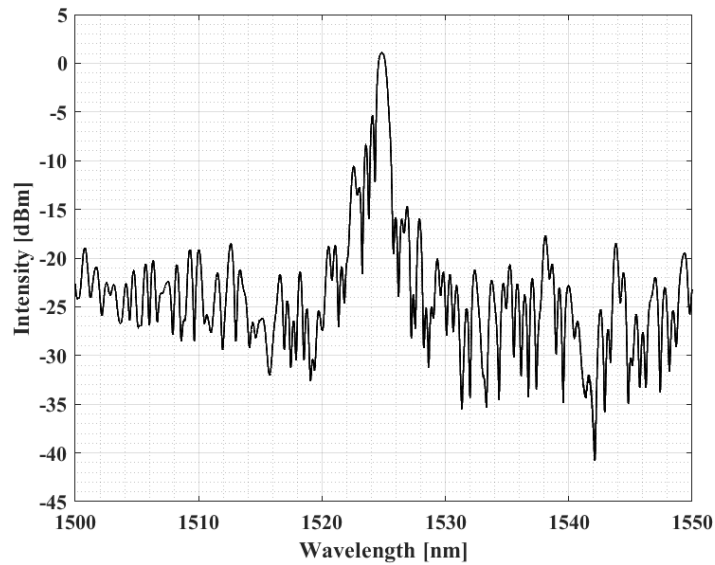
Figure 4.20: Spectrum of the Bragg grating on the optical fibre inscribed while taking into account the $\gamma$ angle of the machine.

For every Bragg grating in the following analysis, we used index matching gel right before the optical touch the last glass plate surface containing the waveguide. For every optical structure, there is a space of 10 µm to separate the surface of the glass plate from the surface of the waveguide to avoid any damage in the main structure during the etching. The focal challenge centres around achieving meticulous alignment between the optical fibre and the midpoint of the waveguide. In our initial try, we successfully inscribed a Bragg grating precisely at the midpoint of the waveguide. Although the resulting Bragg grating exhibited a small intensity, this serves as the inaugural confirmation of the process's viability. This milestone is visually depicted in Figure 4.21.

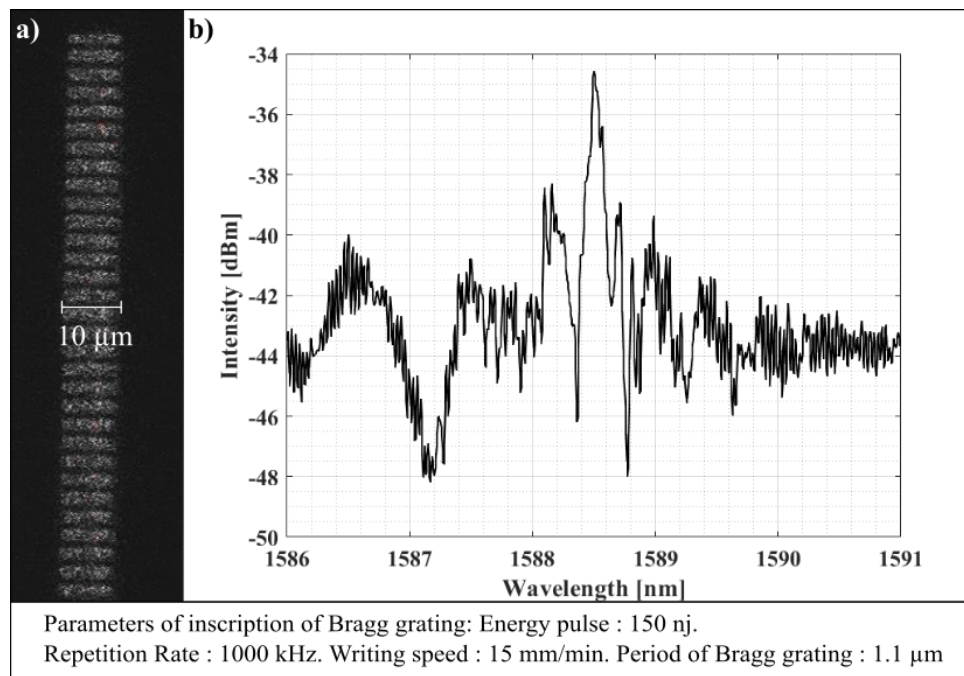| Parameters of inscription of Bragg grating: Energy pulse : 150 nj. |
| Repetition Rate : 1000 kHz. Writing speed : 15 mm/min. Period of Bragg grating : 1.1 µm |

Figure 4.21: **(a)** Microscope picture of the waveguide and the Bragg grating observed under the microscope. **(b)** Reflected amplitude spectrum of the first Bragg grating inscribed into fused silica glass.

The Bragg grating in this instance is inscribed using a pulse energy of 150 nJ, a repetition rate of 1 MHz, and a translation speed of 15 mm/min, resulting in an intensity of 8 dB. We have choosen to use a plane-by-plane Bragg grating but there is an example of the line by line Bragg grating in Appendix B. We hypothesised that the inscription of the Bragg grating could be optimized by considering various factors. One factor involves adjusting the locations where the waveguide and the Bragg grating are inscribed. In the current configuration, the cavity is centred within the silica glass plate, with the centre positioned 250 µm from the surface. In Figure 4.21.a, the waveguide location is based on the voxel diameter (24 µm), positioned 12 µm above the centre and 236 µm from the surface as represented in Figure 4.22.
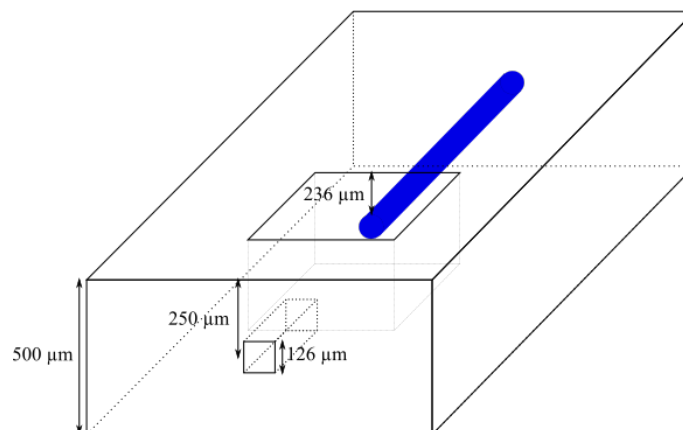


Figure 4.22: Schematical representation of the silica glass plate with an optical waveguide and a fibre holder insertion.

We opted to vary the depth of the waveguide and evaluate the corresponding spectrum intensities. After consideration of the different intensities, we determined that an optimal inscription depth of 240 µm from the surface of the glass plate yielded the highest intensity in the Bragg spectrum. This variance in quality is due to the localization of the waveguide and the Bragg grating is depicted in Figure 4.23.
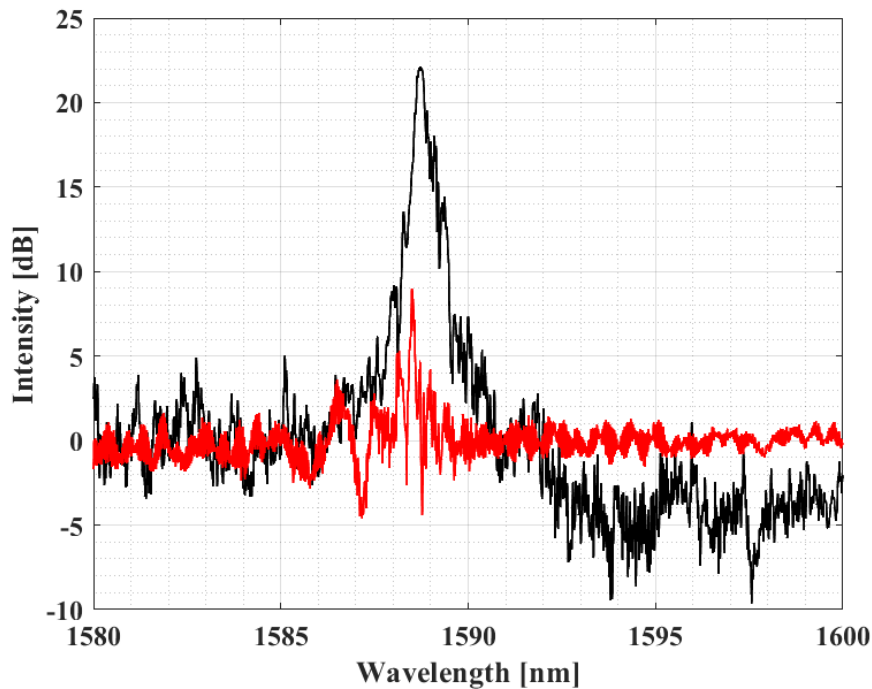


Figure 4.23: Amplitude optical spectrum representing the difference in terms of intensity between the first signal obtained (red curve) and the optimized structure (black curve). Intensity are offset to 0 dB for better comparison between both spectrum

The optimization of the signal is due to the placement of the insertion cavity. An improved alignment significantly increases the transmission quality of the signal, leading to an enhancement in the quality of the Bragg grating as well. From now on the parameter for the inscription of the Bragg grating will remain an energy of pulse of 150 nJ, a repetition rate of 1 MHz, a translation speed of 15 mm/min, a security space of 10 µm between the waveguide and the surface of the glass plate, an inscription at 240 µm from the surface if we want the inscription to be centered. The next step is to test the limit of the Bragg grating and we test different possibilities to characterise the limit of the Bragg grating.

## 4.6 Characterisation of different Bragg gratings

Several tests were conducted in reflection for the Bragg grating. The initial test aimed to ascertain whether the intensity of the Bragg peak is affected by the input side. In the updated design featuring two entrances, the Bragg grating was placed at the beginning of one of them. Subsequently, the quality of the signal was tested when the input signal originated from both the left and right sides. The main objective of this experiment is to measure the quality of the waveguide on the signal of the Bragg but also to assess whether the intensity of the Bragg grating is influenced by its location. Figure 4.24 represents the signal obtained from a Bragg grating as a function of the side of the incoming light.
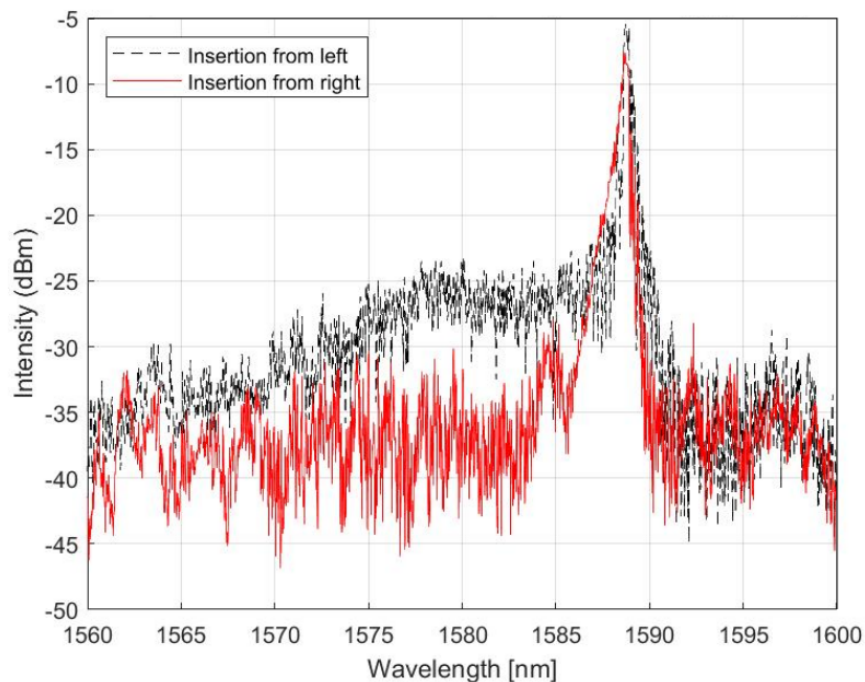


Figure 4.24: Optical spectra obtained from the insertion of the optical fibre on the left and right sides of the microstructure. (Ep = 150 nJ, repetition rate = 1 MHz, writing speed = 15 mm/min, grating period = 1.1 µm).

Figure 4.24 indicates that the side of insertion of the optical fibre does not impact the intensity of the Bragg peak. But we can observe an asymmetry of the geometry as a function of the side of the insertion of the optical fibre. This insertion of the signal may be linked to a lack of alignment at the interaction between the glass plate surface and the waveguide or it can be linked to a damaged optical fibre after several trials of insertion. However, depending on the quality of the waveguide, it may influence the signal quality and induce a slight shift in the Bragg wavelength.

The next objective of this section is to explore diverse possibilities with the Bragg grating while comprehending the encountered limitations.

In our refined configuration, we conducted systematic tests, manipulating various parameters of the Bragg grating. As an initial exploration, we varied the order of magnitude, experimenting with period adjustments to generate both 2$^{nd}$ and 4$^{th}$-order Bragg gratings. We did not try to reach the 1$^{st}$ order because considering the size of the voxel it was not possible, and we did not try to inscribe a 3$^{rd}$. The difference in the order of Bragg grating is explained in Chapter 2 section 3 Bragg grating. The corresponding spectra for these two orders are illustrated in Figure 4.25. This experimental endeavour aims to showcase the versatility and functionality of the technique across different configurations.
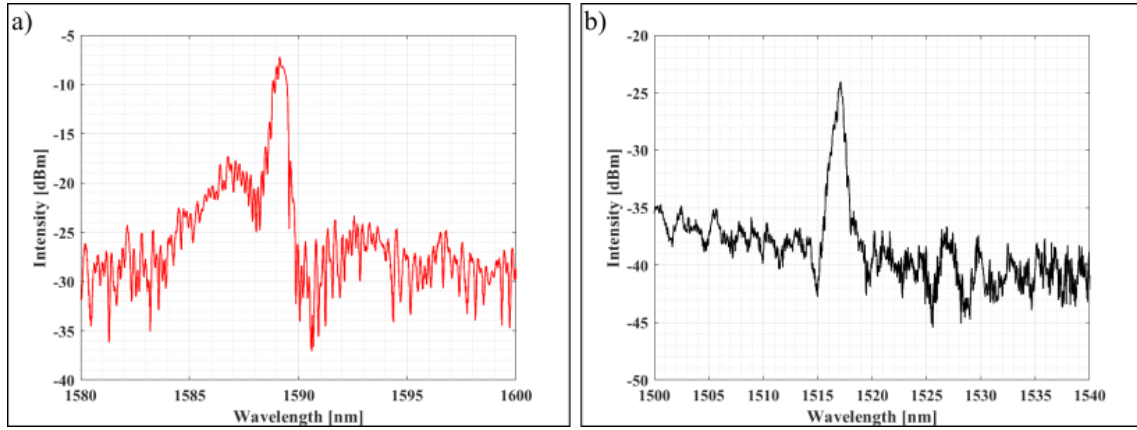


Figure 4.25: **(a)** Spectrum of a 2$^{nd}$ order Bragg grating **(b)** Spectrum of a 4$^{th}$ order Bragg grating.

Having established our capability to inscribe different orders, thereby creating two distinct peaks at different wavelengths, we investigate the feasibility of generating two peaks within the same waveguide.

To explore this, we opted to create two Bragg gratings with varying periods, the first period is 2.1 µm and the second period is 2.2 µm. Considering the equation of the Bragg period, equation 2.9 chapter two section 2, we are able to deduce the theoretical Bragg Wavelength.

$$\lambda_{BG_{2.1}} = \frac{2n_r\Lambda}{M} = \frac{2 \times 1.44462 \; 2.1 \times 10^{-6}}{4} = 1516.851\text{nm}$$

$$\lambda_{BG_{2.2}} = \frac{2n_r\Lambda}{M} = \frac{2 \times 1.44462 \; 2.2 \times 10^{-6}}{4} = 1589.082\text{nm}$$

Upon observing the two experimental spectra, we use the Matlab code to calculate the gravity centre and deduce the two experimental Bragg wavelengths. According to the experimental characterisation, the two experimental Bragg wavelengths are $\lambda_{BG_{2.1}}^{exp} = 1517.2$ nm and $\lambda_{BG_{2.2}}^{exp} = 1589.12$ nm. A minor deviation between the experimental results and theoretical expectations is noted, which could be attributed to the resolution limitations of the femtoprint machine, as we are operating near its threshold.

However, considering the linear relationship between the period of the grating and the Bragg wavelength, it was done to deduce a factor correlating the ratio between the Bragg wavelength and the period of the grating.

$$\frac{2.2}{2.1} = 1.0476$$

$$\frac{1589.12}{1517.2} = 1.0474$$

These results are interesting because they allow us to confirm the accuracy of the result that we have obtained. Then, we connected an optical fibre directly to a Bragg grating on both ends to examine if we could observe its spectrum from both directions. We anticipate detecting the two Bragg peaks with varying intensities in the current scenario. When the optical fibre is positioned on the left side, the left Bragg grating will be initially exposed to the incoming light, reflecting more prominently than the second peak, and vice versa if the light originates from the right side. Figure 4.26 represents an insertion of the optical fibre from the left and the right sides of two different Bragg gratings. The Bragg grating assimilated to $\lambda_1$ has a period of 2.1 µm and a length of 3 mm. The Bragg grating assimilated to $\lambda_2$ has a period of 2.2 µm and a length of 3 mm. Both Bragg brating are separated by 2 mm of waveguide.
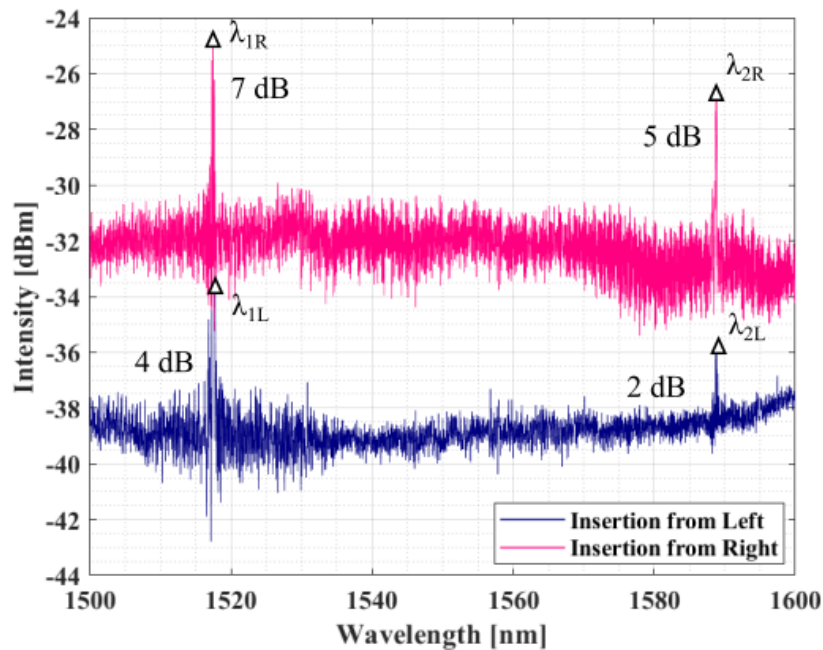


Figure 4.26: Amplitude spectrum of two different Bragg gratings in the same waveguide measured in reflection.

Several features can be observed from Figure 4.26. Firstly, it is evident that both Bragg peaks are observed across the entire spectrum without any difficulties no matter the side of insertion. Notably, although there is a difference in intensity, it remains comparable. This observation suggests that there is no major difference in the quality of reflection within the waveguide. It is also important to note that there is a difference in term of intensity between the two insertions (left and right), this is probably linked to the quality of the insertion of the optical fibre. This study holds significance due to the introduction of the two Bragg gratings, enabling the verification of Bragg grating continuity along the waveguide. This capability opens avenues for innovative applications, such as the creation of a curved waveguide with distinct Bragg gratings positioned at the input and output ends. The successful appearance of both Bragg gratings on the waveguide would serve as evidence that the signal has successfully traversed the entire length of the waveguide. Optimizing signal transmission is an important consideration in the literature [141], which advises that the waveguide bending angle should be kept below 5°. Beyond this threshold, the literature suggests that signal loss becomes prohibitively significant, emphasizing the importance of maintaining a minimal angle to ensure efficient signal propagation. The presentation and results obtained from the Bragg grating constitute important information for the development and characterisation of the waveguide, which will be elaborated in the subsequent section.
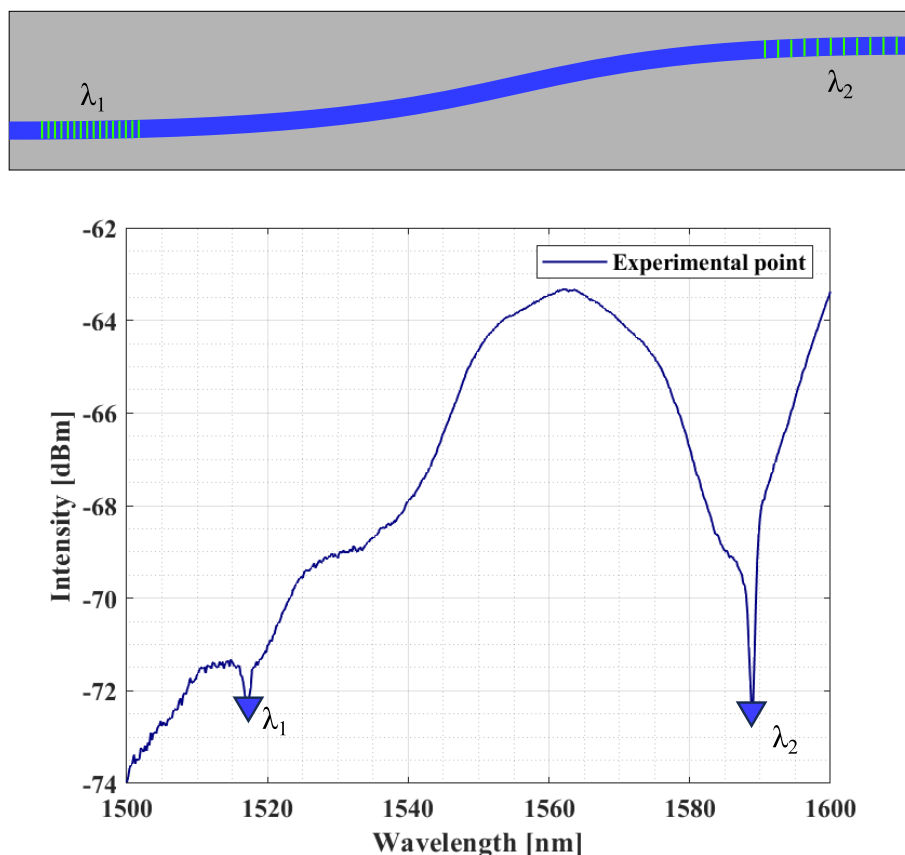


Figure 4.27: Transmitted amplitude spectrum obtained from the two Bragg gratings in the bent waveguide.

## 4.6.1 Detailed characterisation of the optical waveguide

In this section, our primary objective is to delve into the characteristics of the waveguide, extracting essential details about its physical properties, including dimensions and refractive index modulation. Furthermore, we aim to describe the waveguide's birefringence through careful manipulation of the incident polarization angle. Additionally, our investigation extends to determining the specific type of the waveguide, whether it is single-mode or multimode, thereby facilitating precise classification. As elucidated, the characterisation of the optical waveguide involves several steps. An initial crucial step entails the microscopic observation of the waveguide from both an overhead and cross-sectional perspective. The objective of this characterisation is to obtain the precise dimensions of the waveguide with the utmost accuracy. In the context of this study, the microscope serves primarily for quantitative analysis and fundamental observations, such as size measurements. For observing the waveguide, we used a Zeiss optical microscope, specifically an Axio Imager.M2. This microscope offers the advantage of various lighting options for observation, whether in transmission or reflection. Moreover, it allows for the immersion of the waveguides in oil during observation. The shape of the waveguide and microscopic images are depicted in Figure 4.28.
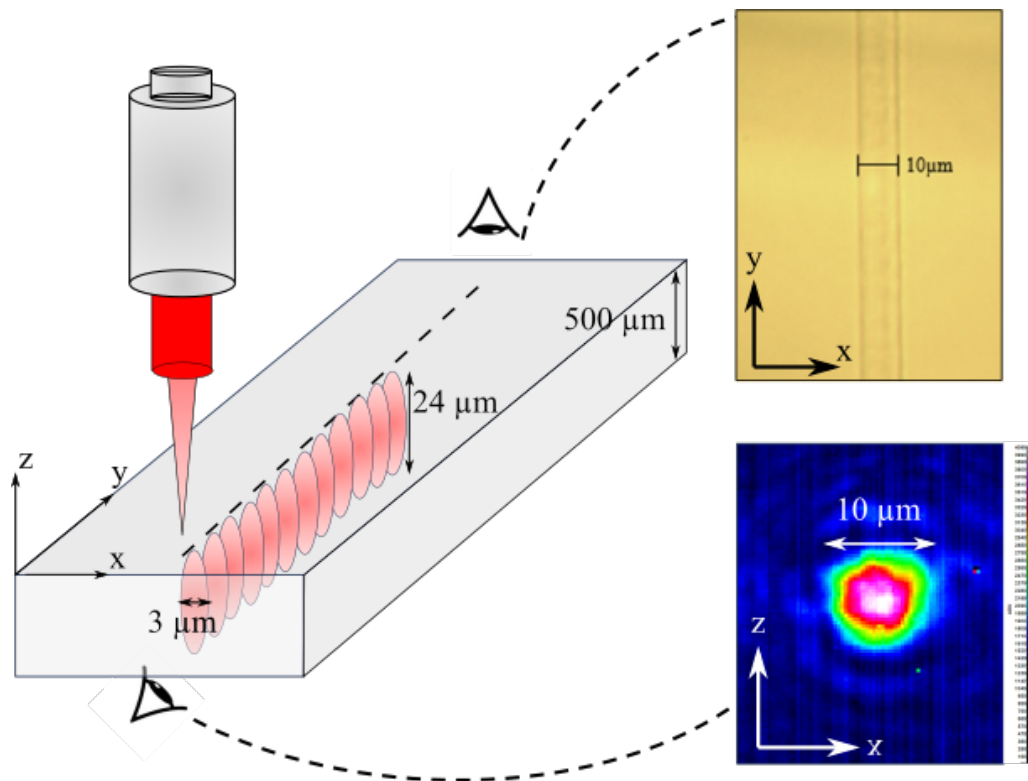


Figure 4.28: Sketch of the femtosecond laser patterning process for waveguide creation in planar substrate, with one microscope picture obtained during the planar characterisation and an IR picture obtained during the cross section characterisation.

This figure is crucial as it provides insights into the shape of the inscribed waveguide. Based on the image, the waveguide appears to be non-symmetrical with a width of 10 μm and a depth of 12 μm, according to the side view obtain with the IR camera. The camera used is a XenICS XEVA-435 Camera, 320 x 256 pixel resolution. The camera offer frame rates of more than 340 Hz. linked to a broad band light source from Amonics (ALS-CL-17-B-FA ), with a spectral range of 1528nm to 1608nm and an exciting wavelength of 1050 nm. This asymmetrical shape is a significant parameter as it will induce birefringence, which can be further characterised. It is important to take into account that the waveguide has a length of 22 mm in the current situation. Additionally, we observed the output of the optical waveguide using an IR camera to examine the type of mode and the signal spreading at the waveguide's output. Figure 4.29 shows the signal intensity at the output of the waveguide, with the red colour indicating the higher intensity.
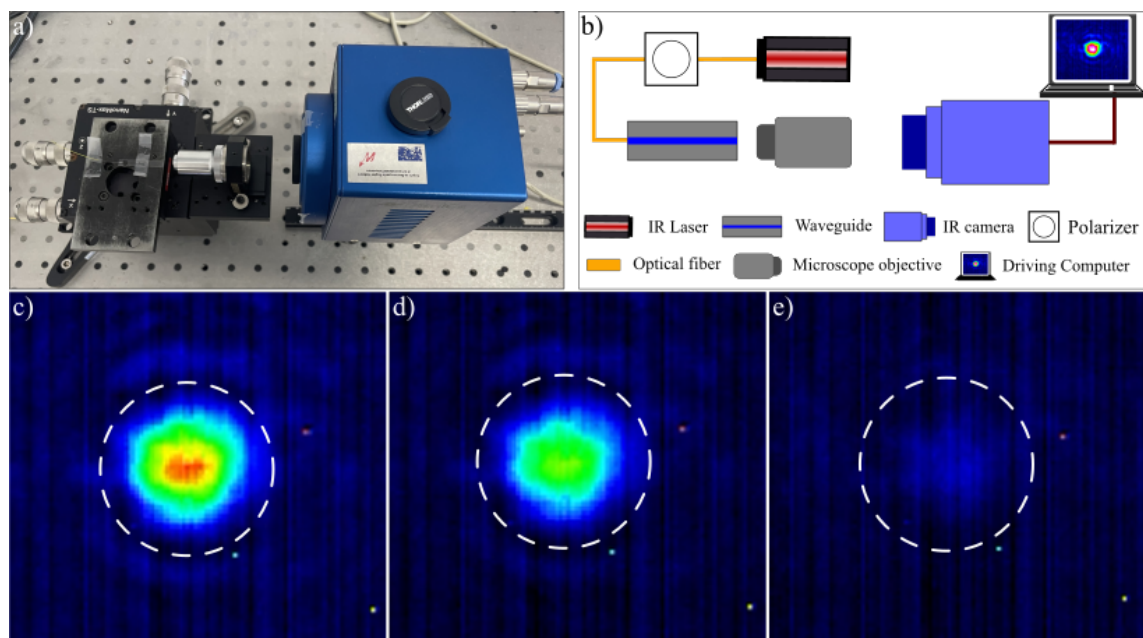


Figure 4.29: **(a)** Picture of the IR analysis setup. **(b)** Schematic representation of the IR analysis setup.**(c)** Picture of the waveguide observed with a 0° angle of polarization
. **(d)** Picture of the waveguide observed with a 45° angle of polarization.**(e)** Picture of the waveguide observed with a 90° angle of polarization.

From the observations in Figure 4.29, it is apparent that the waveguide is fully functional, exhibiting an intensity profile, and it seems to be a single-mode waveguide, due to its circular shape. Also there is only one output on the signal. However, our exploration involved changing the polarized light to assess potential variations in the output. Remarkably, we observed fluctuations in the output intensity corresponding to changes in the polarization angle. This finding affirms the birefringent nature of the waveguide but also implies the influence of the type of polarization employed. After characterising the dimensions of the waveguide using the microscope, the subsequent step involves measuring the numerical aperture (NA) and determin-

ing the type of mode we are working with. To measure the numerical aperture, we constructed the set-up depicted in Figure 4.30 a and schematically represented in Figure 4.30 c to trace the path of a red laser through the waveguide. Once we carefully aligned the waveguide with the red laser, we observed an initial pattern on a white screen, as shown in Figure 4.30 b, indicating a favourable output.
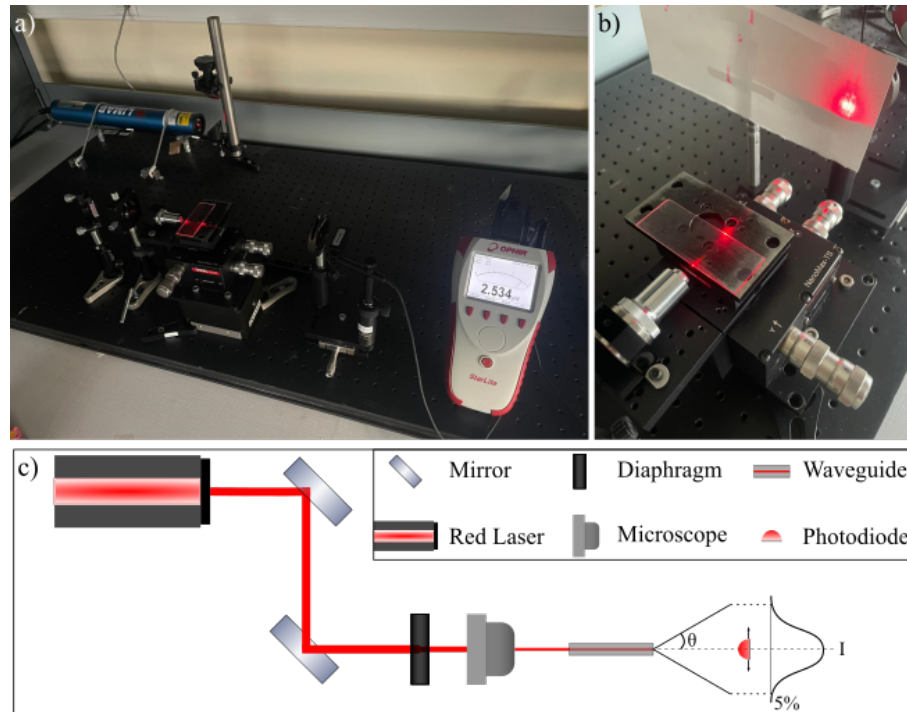


Figure 4.30: **(a)** Picture of the optical set-up used to characterise the numerical aperture. **(b)** Picture of the output of the red laser after going through the optical waveguide. **(c)** Sketch of the optical path to characterise the numerical aperture (NA) at 633 nm.

The final step in characterising the numerical aperture involved placing a photodiode at the waveguide's output to measure the intensity at the signal's maximum. Upon reaching this peak intensity, we adjusted the photodiode until the signal decreased to 5 % of its initial value, this method of characterization is described by Lapointe [142]. This intensity represents the numerical aperture's limit. Using the numerical aperture equation:

$$NA = n \times \sin\theta \tag{4.1}$$

We could deduce $\theta$ and subsequently calculate the numerical aperture. In the present situation, the numerical aperture was estimated to be 0.04. However, due to the lack of material at the University of Mons, we only could characterise the numerical aperture for a red wavelength. We should not take into account this numerical aperture because we conducted the analysis with a single-wavelength red laser. Even though the diode was designed for a red wavelength.

This analysis provides us with an idea of the expected numerical aperture. This is an important parameter that must be taken into account. As explained by [143] a waveguide is considered single-mode when its numerical aperture is below 0.4. In the current situation this value means that the waveguide will allow single-mode propagation.

In the next section, we aimed to conduct a more refined characterisation of the impact of femtosecond laser pulses on the silica glass surface. Insights from existing literature pointed to the phenomenon wherein low-energy femtosecond laser pulses induce densification in the silica glass, through a modification of the structure of Si-O bonds [111]. This alteration results in observable variations in the refractive index of the material. The densification effects manifest visually through interference and phase changes, making them observable through Digital Holographic Microscopy (DHM). The DHM from Lyncee is an advanced imaging device that uses holography and digital technology to capture high-resolution, three-dimensional images of microscopic objects. DHM is non-invasive, offers real-time imaging, and is valuable for various applications, including biology, materials science, and microelectronics. It provides quantitative data on object height, volume, and more, making it a versatile tool for research and analysis in both scientific and industrial settings. Its ability to resolve fine details and capture dynamic processes makes it an essential instrument in studying microstructures and living cells. DHM uses a functional red laser (wavelength: 632 nm) which is divided into two distinct components. The primary signal is directed towards the observed sample, while the secondary signal is a reference. Then these signals are combined to produce an interference pattern, which is then digitally captured as a holographic image. This hologram goes through computational processing to reconstruct a three-dimensional representation of the sample, providing comprehensive insights into its shape and structure, including surface topography. The resulting reconstruction leads to three distinct image types: holographic, phase, and intensity, as illustrated in Figure 4.31.
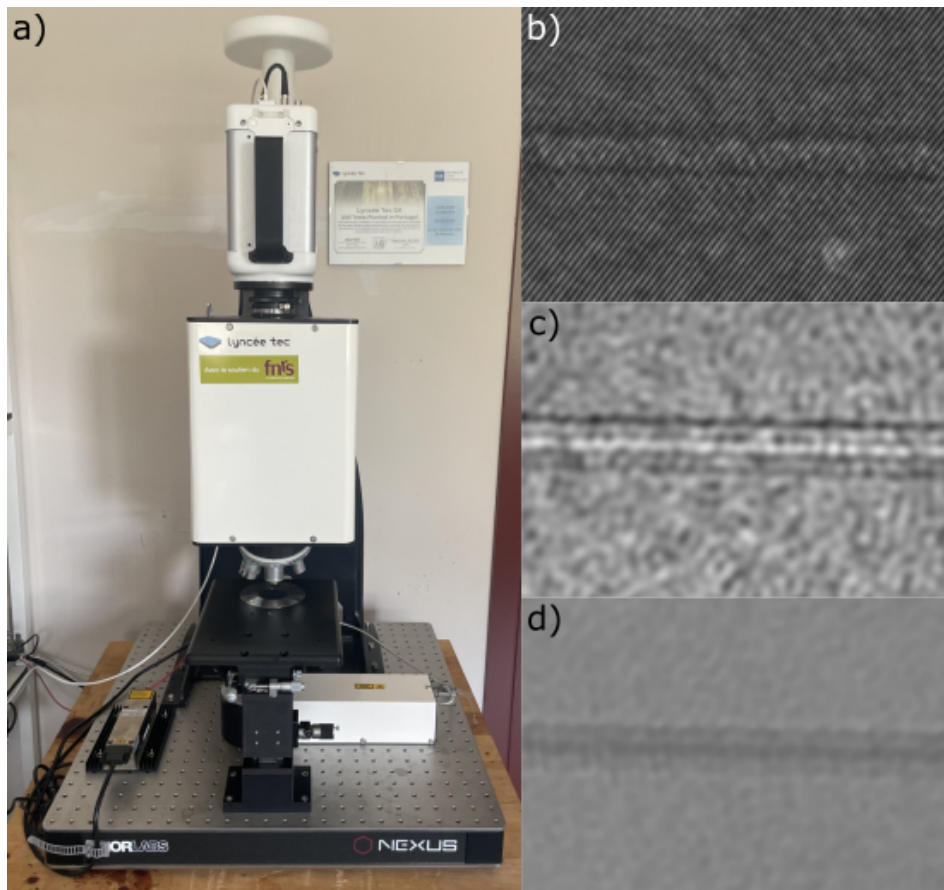
Figure 4.31: **(a)** Picture of the DHM microscope setup. Picture of a waveguide in silica glass observed through the microscope by taking into account the holographic difference **(b)**. The intensity difference **(c)** and the phase difference **(d)**.

Figure 4.32 serves to illustrate the evolution of the refractive index as a function of the pulse energy employed for inscribing the optical structure. The objective of this investigation was to establish a relationship between pulse energy and the evolution of the refractive index. The inset graph in Figure 4.32 encapsulates this relationship, through a representation of the interaction between femtosecond laser pulse energy and the resultant changes in refractive index within the silica glass structure. This exploration contributes to valuable insights into the fundamental mechanisms underlying the femtosecond laser-induced modifications in the optical properties of silica glass, furthering our understanding of the intricate processes involved in the inscription of optical structures.
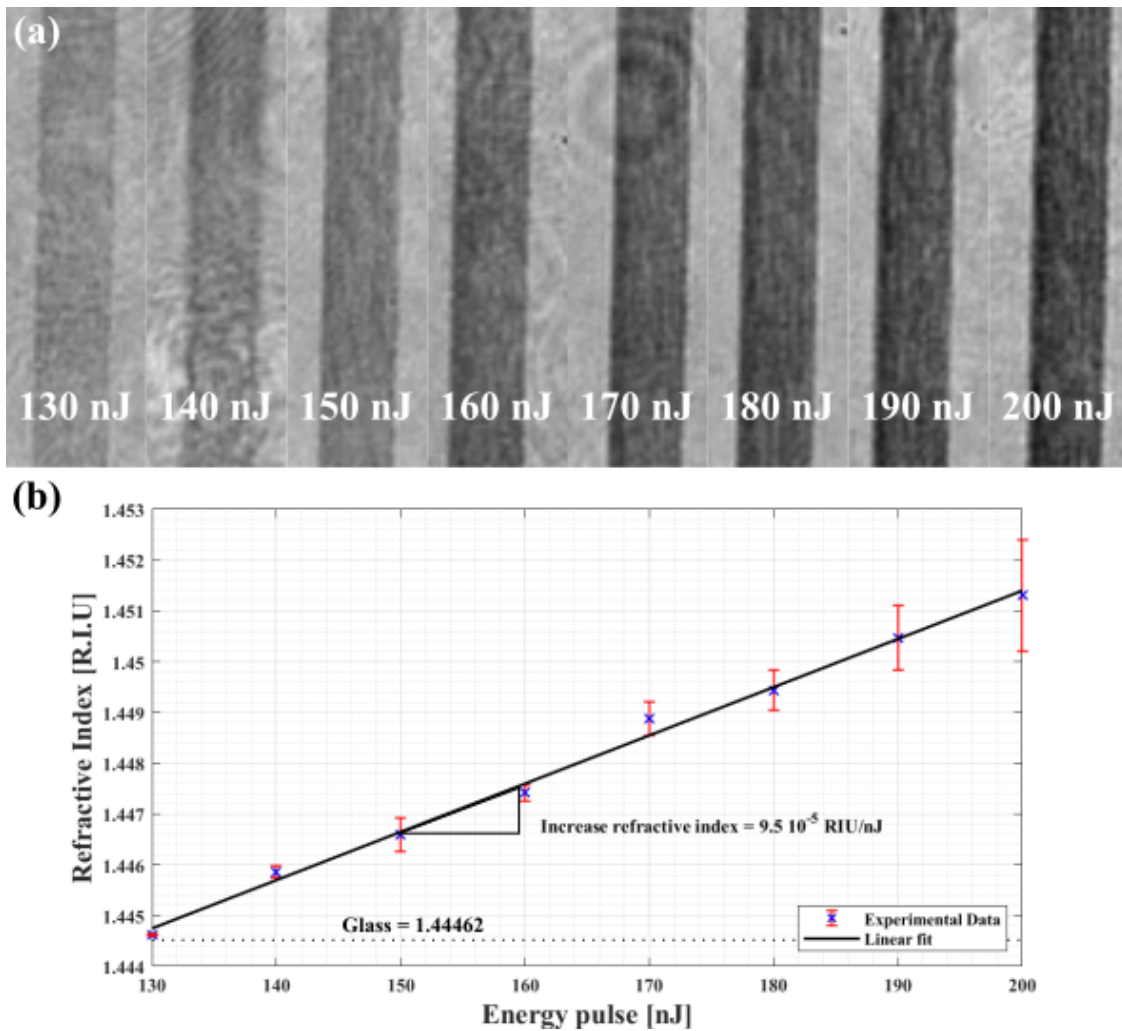
Figure 4.32: DHM pictures of the waveguides for different laser pulse energies (from 130 nJ to 200 nJ by steps of 10 nJ). **(a)** Microscopic pictures of the evolution of the waveguide as a function of the energy of the pulse. **(b)** Computed refractive index modifications as a function of the pulse energy. The standard deviation is obtained from the measurement of three sets.

In light of the previous refractive index measurements through DHM, we have derived the values of the numerical aperture (NA) of the optical waveguides according to the following equation [142]:

$$\mathrm{NA} = \sqrt{(n_1^2 - n_2^2)} \tag{4.2}$$

Here $n_1$ and $n_2$ are the refractive index of the modified and unmodified silica substrate respectively. Considering the refractive index of the silica glass at 1500 nm to be 1.44462 when there is no modification, according to the Siegert wafer's datasheet n°T20394. With the value of 1.4473935 based on DHM measurements for the waveguide produced with 130nJ pulses energy, we determine the corresponding Numerical Aperture to be 0.09.

It is noteworthy to consider the implications of the estimated NA in the context of optical waveguides, particularly in distinguishing between single-mode and multi-mode systems. Taking into consideration the waveguide dimensions and the propagation wavelength, in single-mode waveguides, characterised by a single optical mode propagation, a lower NA is generally favoured. On the other hand, multimode waveguides, accommodating multiple optical modes, often benefit from a higher NA to support broader mode propagation. Therefore, the determined NA value plays a pivotal role in the operational characteristics of single-mode and multimode optical waveguides. The NA and the characterisation to obtain the V-Number will give us the information on whether the waveguide is single mode or multimode are crucial parameters for describing the waveguide. However, we also need to examine the impact of birefringence on the overall output of the signal.

After successfully characterising the properties of our waveguide, our next objective is the insertion of a Bragg grating. We then investigated the polarization dependence in a Bragg grating. The latter was inscribed during the same operational procedure as the waveguide, featuring a uniform period of $\Lambda = 1.1$ µm and extending over a length of L = 3 mm. Our analysis focused on the second-order Bragg peak positioned at 1588 nm. While submitting the system to polarized light, we made a noteworthy observation: the Bragg peak exhibited a discernible spectral shift depending on the input polarization state. This shift is a direct consequence of the photo-induced birefringence during the manufacturing process, a phenomenon that is spectrally represented in Figure. 4.33 for the two input states of polarization that yield the maximum wavelength separation between the reflected amplitudes. This corresponds to the so-called fast axis (red curve) and slow axis (blue curve). Hence, this birefringence is manifested as a differential shift of 300 picometers in the Bragg peak wavelength (wavelength separation between the red and blue curves). This experimental outcome underscores the influence of waveguide-induced birefringence on the spectral characteristics of the Bragg grating. In this case to get the Bragg wavelength we decided to choose the technique of the gravity spectrum. It is known that, for Bragg gratings, the wavelength separation between the slow and fast axes corresponds to $2 \times \Delta_n \times \Lambda$ where $\Delta_n$ is the birefringence value and $\Lambda$ the grating period. Hence, a wavelength separation of 300 pm corresponds to a birefringence value of $2.72 \ 10^{-4}$, which is important and corresponds to typical values reached in polarization-maintaining optical fibres.
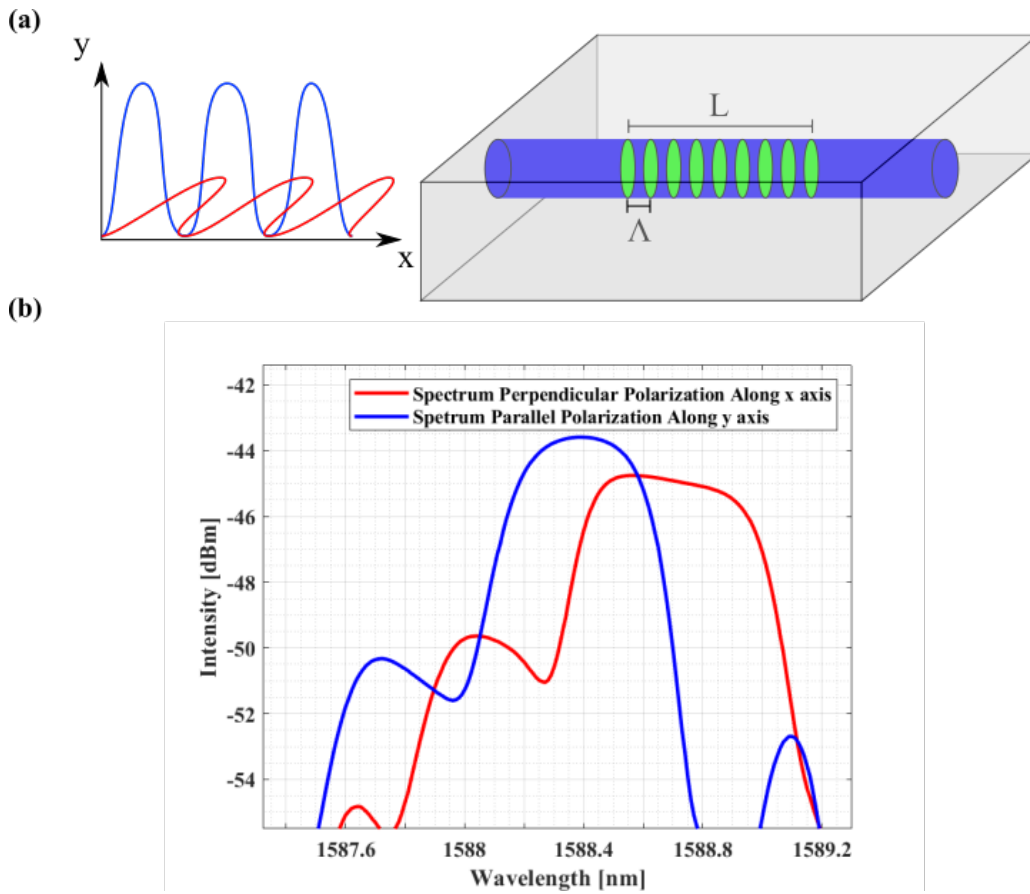
Figure 4.33: Reflected amplitude spectrum of the Bragg grating measured for two orthogonal polarization states.

Given the relatively high birefringence value measured in Figure 4.33, we aimed to investigate the effect of the laser polarization state on the photo-induced birefringence. To accomplish this, we conducted reflective measurements on two distinct Bragg gratings, each inscribed under specific parameters. The first Bragg grating was inscribed with an energy of 150 nJ, a translation speed of 15 mm/min, a repetition rate of 1 MHz, a period of 1.1 µm, and a perpendicular polarization during the inscription. The second Bragg grating shared identical inscription parameters, with the only difference being a parallel polarization during inscription. Here, polarization is defined as parallel or perpendicular to the writing direction as represented in Figure 4.34.

Then, we characterised the evolution of birefringence at increments of every ten degrees of polarization. The primary objective of this investigation was to derive a comprehensive and nuanced understanding of birefringence evolution in response to varying degrees of polarization.

In Figure. 4.34. a, the waveguide and Bragg grating are inscribed using perpendicular-polarized femtosecond laser light, while in Figure. 4.34. b, the waveguide is inscribed with parallel-polarized femtosecond laser light.

Figure 4.34: Schematical representation and characterisation curve of the evolution of the Bragg wavelength as a function of the state of polarization in the case of a waveguide inscribed with a perpendicularly polarized inscription **(a)** and with a parallel polarized inscription **(b)**.
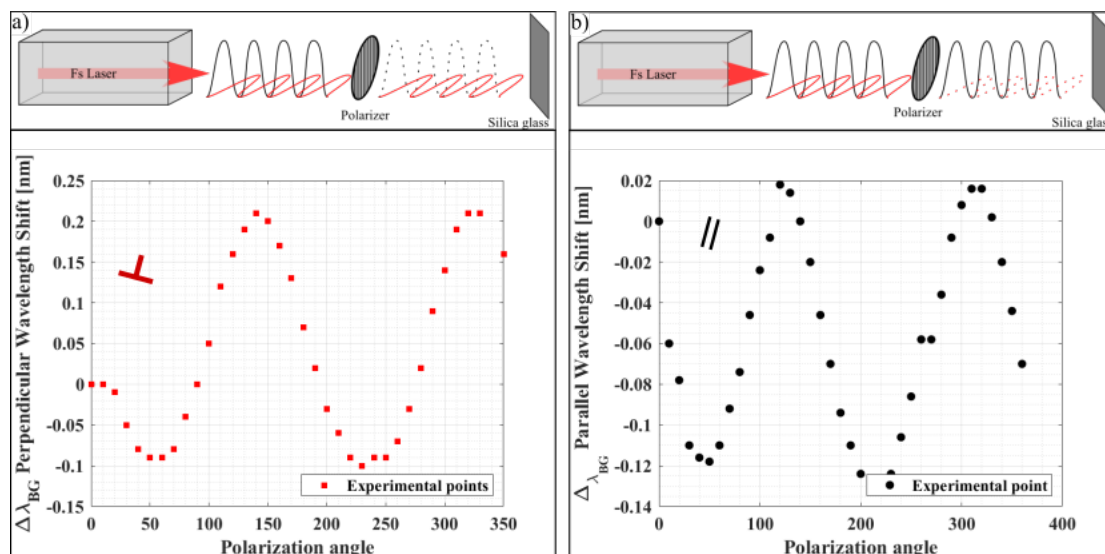
For the parallel laser polarization, the wavelength separation linked to the birefringence drops to 142 pm, corresponding to a birefringence value of $1.34 \times 10^{-4}$.

These observations affirm that the use of perpendicular-polarized and parallel-polarized femtosecond laser light imparts unique birefringence to the waveguides, resulting in distinct optical properties and behaviours. Taking into account the future applications we would want to avoid the birefringence as much as possible because it could interfere in the quality of the shift of the Bragg grating. This divergence in polarization orientation provides a valuable avenue for exploring and understanding the waveguide's response to different polarizations, opening up opportunities for applications in optical communication and photonic devices such as microchips or biosensing. This phenomenon emphasizes the precise control over polarization characteristics during the fabrication process, highlighting the potential for customized birefringence in waveguide design. In sensing, for instance, it also paves the way for transverse force measurements.

## 4.6.2 Conclusion

In this section, an array of optical structures was meticulously engineered. Our initial focus was on assessing the impact of femtosecond laser irradiation directly on fused silica glass. Conducting numerous inscriptions at diverse energy thresholds while conscientiously minimizing the energy input, our investigation revealed that the most efficient energy level for this particular application of femtosecond laser pulses is 130 nJ.

Then our investigation aimed to determine the optimal parameters for crafting the most proficient waveguide inscriptions. Commencing with the minimal energy pulse, we systematically assessed the writing speed of the apparatus. Through a series of tests conducted at varying speeds, we ascertained that the most uniform results were achieved at a speed of 20 mm/min. In the context of waveguide fabrication, we explored diverse spacings between laser paths and various inscription methodologies for homogeneity. Ultimately, we choose to employ planar inscriptions with a spacing of 0.5 µm between individual laser paths based on their superior homogeneity characteristics. Lately, the decision was made to incorporate a Bragg grating within the core of the established waveguide. Initially, attempts were made to directly inscribe a Bragg grating into the optical fibre core. The objective was to assess the feasibility of Bragg grating inscription within this specific context. Various energy levels and periods were systematically tested, and the most optimal parameters were identified for the Bragg grating inscription. Notably, the Bragg grating inscribed with a pulse energy of 150 nJ, a writing speed of 15 mm/min, and a repetition rate of 1 MHz emerged as the configuration yielding the most favourable results. The different parameters for the Femtoprint machine are summarized in appendix B.1.

Following the aforementioned trials, we explored the direct inscription of a Bragg grating onto the planar glass substrate, varying the period of the grating. Specifically, we conducted experiments involving the inscription of two distinct Bragg gratings, each designed for a different wavelength, within individual waveguides. Subsequently, these two Bragg gratings were integrated into a single waveguide to assess the combined effects. Following the exploration of the diverse parameters outlined above, a comprehensive characterisation of the waveguide was undertaken. This characterisation encompassed an assessment of size, mode types, sensitivity to refractive index variations, as well as the birefringence of both the waveguide and the incorporated Bragg grating.

# Chapter 5

# Study of the Temperature and Strain Sensitivities of Built-in Bragg Grating

In this chapter, we studied the Bragg grating sensitivity to the variation of different parameters: The temperature in the surrounding environment and the reactivity to mechanical deformation. The primary objective is to provide a comprehensive description of the experimental setup, detailing the types of characterisation methods employed. Each step in the process was executed to define the sensitivity of the Bragg grating in our experimental context.

## 5.1 Effect of Temperature Sensitivity

The Bragg grating is known to be sensitive to various parameters, especially temperature and strain. Literature mentions a sensitivity of the order of 10 pm/°C. The experimental set-up is represented in Figure 5.1. The principle is just to measure the evolution of the Bragg peak in reflection as a function of the evolution of the ambient temperature controlled with a hot plate. We decided to conduct the measurements on the silica glass hot plate because, even though there is a cavity for the insertion of the optical fibre, we wanted to have control over and be able to adapt the position of the glass plate. However, we acknowledge that if we were to repeat the experiment, we would opt to conduct it in an oven instead of on a glass plate.
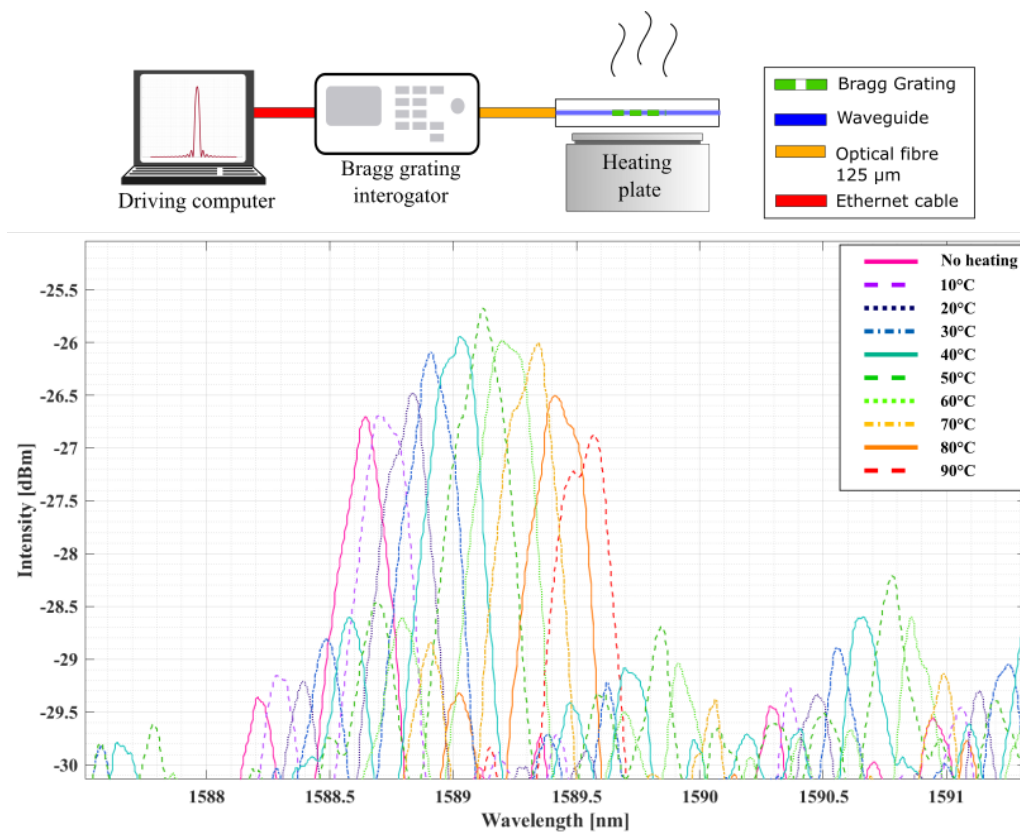
Figure 5.1: characterisation set-up for the Bragg grating measurements in reflection mode. Top : Schematic representation of the experimental set-up. Bottom : Spectra for the characterisation of the evolution of the Bragg grating as a function of the temperature.



Figure 5.2: Eight characterisation measurements for Bragg gratings in reflection mode through six different batches. The different batches represent the same plate measured at six different times in this case.

The experimental configuration of Figure 5.1 includes a Bragg grating interrogator linked with an ethernet cable to a computer for a control interface. The latter encompasses a tunable laser source and a photodiode. It operates as an optical spectrum analyser in the C+ L band. Temperature modifications were introduced using a Fisher Scientific heating plate. Six measurements were carried out starting from room temperature, a temperature increase of 140°C was applied by steps of 20°C. The data represented in Figure 5.2 were different from each other in terms of sensibility obtained. We thought that the reason for this difference was due to a lack of precision of the device. So in the next measurements, we decided to use a Peltier with a PID (Proportional-Integral-Derivative) temperature controller and an external thermocouple to measure the temperature changes of the sample, as represented in Figure 5.3. In the following graph, we have realised ten measurements from three different samples, the error bars come from the standard deviation. [144]



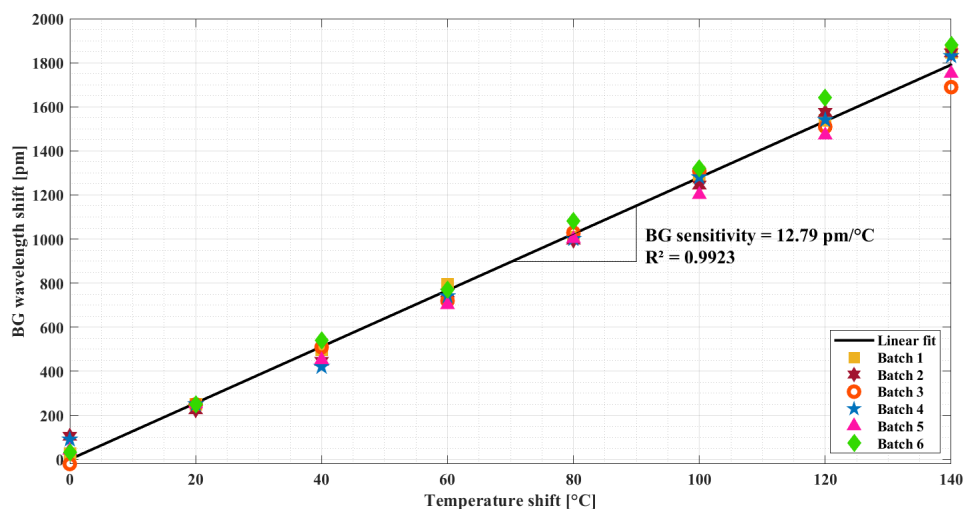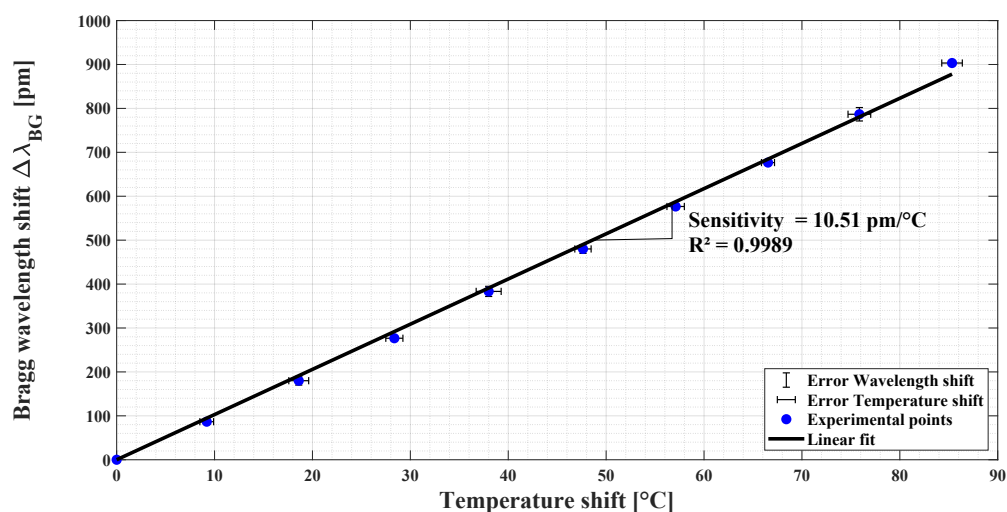Figure 5.3: Characterisation of the Bragg grating along the evolution of the temperature. Measured from three different samples that have been etched within the same glass plate

.

With this modified set-up we obtained a sensitivity which was closer to the sensitivity obtained in the literature so that this way of characterising the Bragg grating for temperature measurements is satfisfactory. The next section focuses on our second type of characterisation, centred on the mechanical deformation capabilities of fused silica glass. The inherent elasticity of fused silica glass enables us to induce controlled deformations. By considering parameters such as thickness, we explore the potential for deformation in fused silica glass. This characterisation provides valuable insights into the material's structural flexibility and lays the groundwork for applications demanding tailored mechanical responses in silica glass.

## 5.2    Axial Strain Sensitivity

We initiated the mechanical deformation characterisation by focusing on axial traction. This choice was made due to the simplicity of obtaining and calculating axial strain.

To characterise the evolution of the Bragg grating we have developed a set-up to apply controlled traction values. In the first set-up represented in Figure 5.4, we have decided to use different weights and put them into a 3D printed basket to apply traction on the Bragg grating with the flexible structure. Initially, the glass plate is separated into distinct sections. Notably, there is an alignment cavity for the optical fibre, followed by the waveguide and Bragg grating encased within a flexible structure inscribed directly onto the glass plate. This flexible structure assumes a pivotal role as the stretched component for axial traction characterisation, elaborated upon in the "Theoretical Background" chapter, in the Sensor section. To encapsulate this scenario, we find ourselves in a traction situation wherein we apply tension to the flexible part of the glass structure.

$$\sigma = E\epsilon \qquad (5.1)$$

Here, $\sigma$ is the stress, E is the modulus of Elasticity and $\epsilon$ is the strain. Through the Hooke law (Equation 5.2) we can derive the strain experienced by the glass plate where L is the length and $\epsilon$ is the strain, considering the modulus of elasticity is constant the strain is the following.

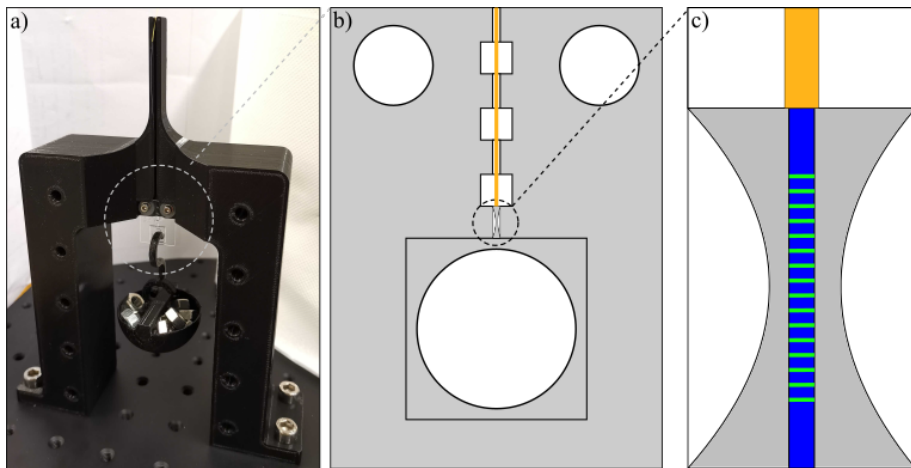$$\epsilon = \frac{\Delta L}{L} \qquad (5.2)$$



Figure 5.4: **(a)** Picture of the Infuse traction set-up **(b)** Schematic representation of the glass plate with the flexible structure **(c)** Schematic representation of the waveguide and the Bragg grating.

However, a circular open cavity was used to exert pressure on the Bragg grating, and this setup had certain limitations. Firstly, there was a lack of precision in quantifying the traction, as bolts were manually added, requiring intermittent weighing—an impractical design aspect. Furthermore, the addition of bolts introduced movement, potentially leading to non-uniaxial traction. The second major drawback was associated with characterisation. The characterisation process relied on the weight of the bolts, limiting the range of achievable strain levels. Consequently, data acquisition was constrained, resulting in a reduced quantity of available data points. We then decided to adopt a new set-up. It remains on the same principle as explained before but instead of adding bolts with a defined weight we have a voice-call actuator directly linked to the circular cavity of the glass and we pull directly on the flexible structure represented in Figure 5.5.
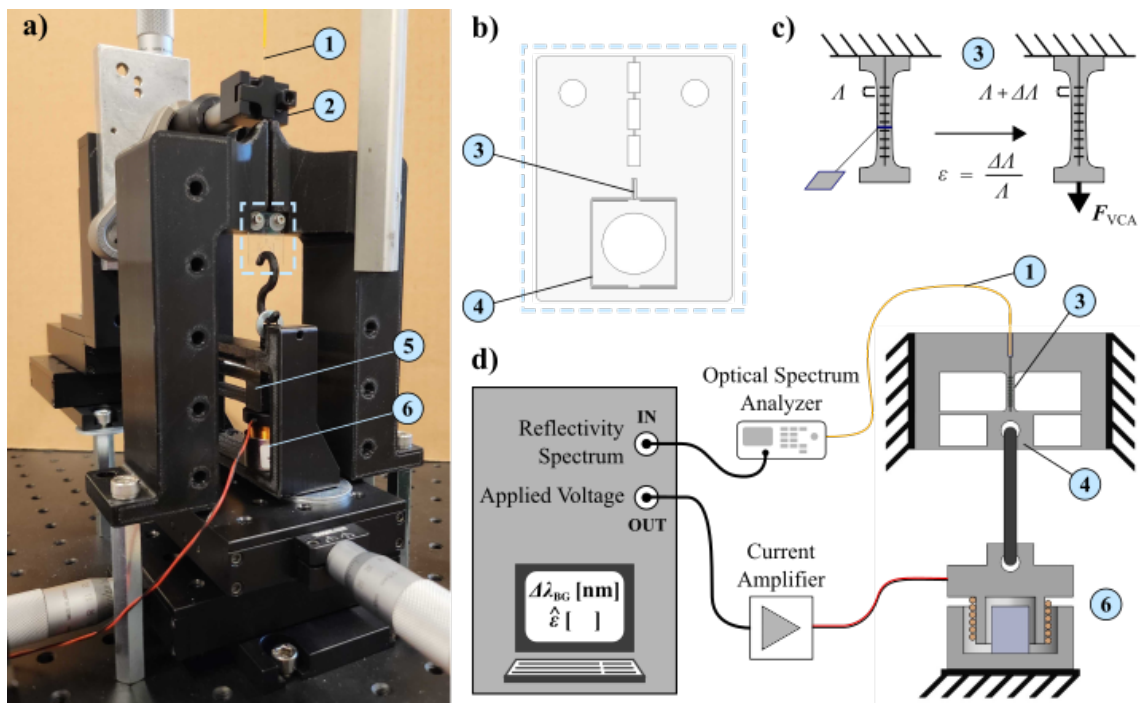


Figure 5.5: Testbench developed to characterise the axial strain sensitivity of a Bragg Grating sensor inscribed in a fused silica tensile specimen. **(a)** The tensile specimen (in the blue square) is hanging fixed by two screws. The optical fibre 1) connected to the Bragg interrogator is placed at the top. A fibre clamp 2) is used to position the fibre. **(b)** The tensile specimen 3) is included in a monolithic structure. **(c)** The tensile specimen contains a Bragg grating which undergoes a strain $\varepsilon$ when the force $\boldsymbol{F}_{\mathrm{VCA}}$ is applied at its free end 4). **(d)** Experimental scheme: the optical fibre 1) is guided to interface with the tensile specimen 3); the load is applied with a Voice-Coil Actuator (VCA) 6); the moving coil is guided in translation using a monolithic 3D printed flexure mechanism 5); A LabVIEW platform records the reflected spectrum from the interrogator and the applied voltage commanding the VCA; the estimated applied axial strain $\hat{\epsilon}$ and it is resulting Bragg grating wavelength shift $\Delta\lambda_{\mathrm{BG}}$ are obtained by post-processing with Matlab.

As explained before, the characterisation of axial strain sensitivity employs a voice-coil actuator, and the experimental set-up, along with its schematic representation, is illustrated in Figure 5.5. The force, denoted as $F_{\text{VCA}}$, applied at the free end of the tensile specimen, is controlled through the analogue output of the National Instrument Multifunction I/O device (USB-6002). To drive the voice-coil actuator $(1.53 \text{ NA}^{-1})$ based on the applied voltage, a custom current amplifier $(0.2 \text{ AV}^{-1})$ is employed. The tensile specimen maintains uniformity along its length. Here, $F_{\text{load}}$ corresponds to $F_{\text{VCA}}$, and $S$ represents its cross-sectional area $(47.5 \times 207 \text{ µm}^2)$. Different characterisations have been realised and so far to follow the Bragg wavelength, we have always used the maximum intensity and assimilated it to the Bragg wavelength. In this case, we have observed a peculiar phenomenon: the appearance of another peak, represented in Figure 5.6. At first we thought this was linked to the birefringence but after testing it witha polarizer we have to say that we do not know the origin of the second peak. It is possible it is linked to the shear stressed.
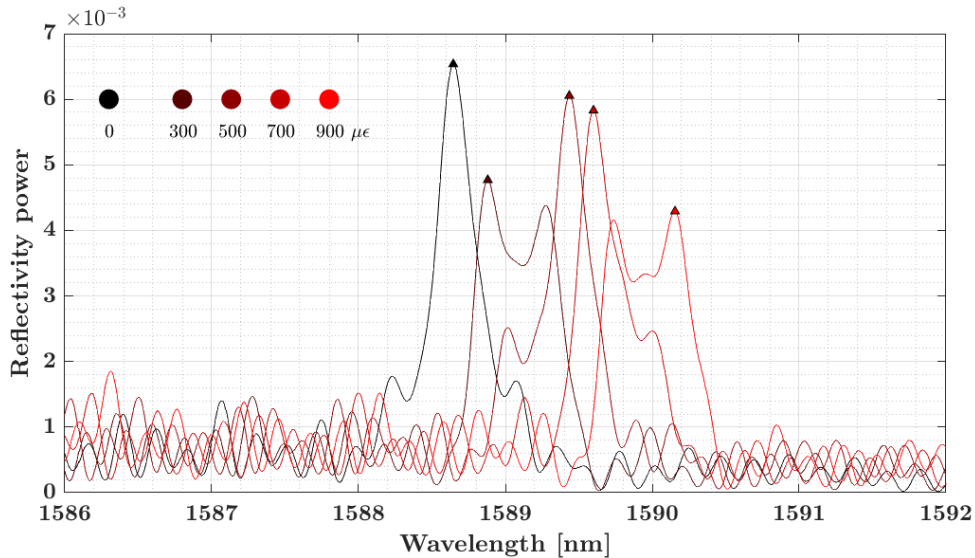


Figure 5.6: 5 reflected amplitude spectra of the traction structure measurements at 0, 300, 500, 700 and 900 µε. Strain is applied on the tensile specimen using a VCA.

The graphic reveals a noteworthy observation: when tracking the maximum of the spectrum without applied strain, a single Bragg peak is evident. However, when strain is introduced, such as 300 µε, or 900 µε, a second peak emerges, posing complications in accurately tracking the Bragg wavelength. The evolution of this second peak, superior to the initial Bragg peak, introduces a discontinuity in the characterisation process. This "jump" is illustrated in Figure 5.7, where the evolution of the Bragg peak is correlated with the applied strain.
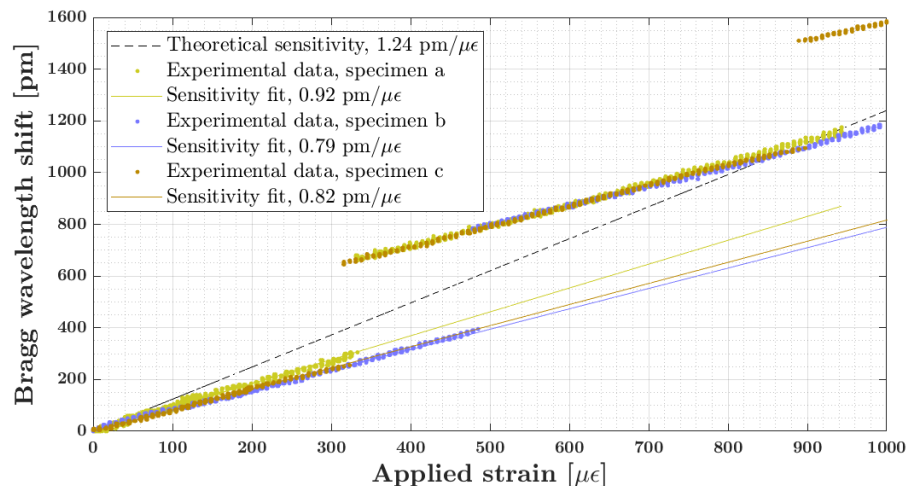
Figure 5.7: Bragg grating sensitivity to axial strain of three different specimens of tensile strain sensors. Strain is applied using a VCA. The VCA command is set such that the strain applied varies from 0 to 1000 µε.

As depicted in Figure 5.7, it is evident that in three distinct measurements, following the maximum yields two different jumps in the characterisation. This issue appears to be recurrent. Consequently, for subsequent analyses, we have opted to shift our focus from the maximum and instead concentrate on the midpoint of the area beneath the curve, we decided to choose the midpoint area beneath the curve because it fits more the theoretical model. This alternative technique considers both peaks, reducing the challenge posed by the emergence of a second peak and providing a more reliable approach for further analysis. We did the same analysis and applied the new method to follow the Bragg wavelength. The method to characterise the Bragg peak is explained with a simple version of the Matlab code in Appendix C. The characterisation is presented in Figure 5.8.
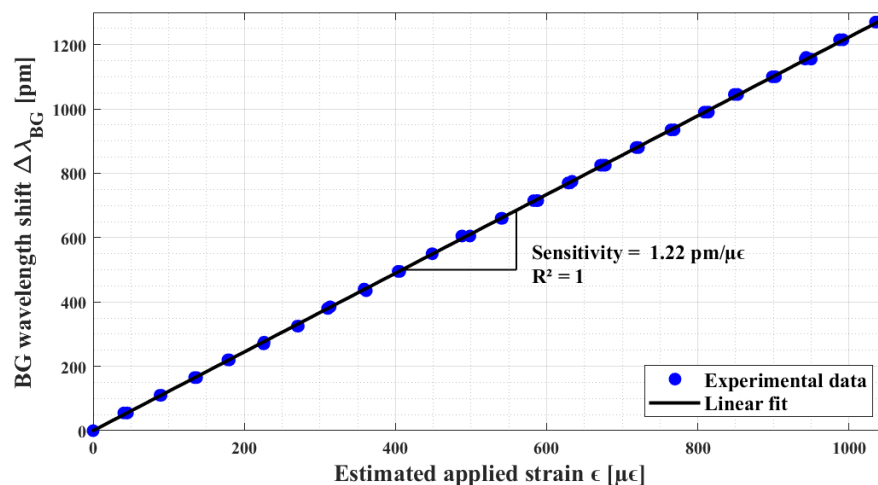


Figure 5.8: Evolution of the Bragg wavelength as a function of the axial strain application. For this measurement, the same sample was measured 3 times.

This wavelength shift is determined by calculating the difference between the strained and unstrained specimens. To minimize the potential impact of air fluctuations during the experiment, the experimental set-up is positioned within a confined space. The linear regression of the raw data yields an axial strain sensitivity of 1.22 pm/με. This sensitivity value is approximately 10% higher than the typical values obtained in optical fibres but aligns well with the theoretical predictions for the planar substrate. In the next section, we decide to focus on another type of mechanical deformation known as the three-point deformation.

## 5.3    3-point Bending Sensitivity

Now that we have successfully developed axial traction, the next phase involves the establishment of three-point characterisation for mechanical deformation. This process proved to be slightly more complex compared to axial strain, primarily due to the necessity of precisely applying a vertical constraint without compromising the integrity of the glass plate. The three-point mechanical characterisation set-up is more intricate than the previous one because it is constrained in terms of bending owing to the relative fragility of the glass plate in a bending process. In this section, we will comprehensively detail the various steps undertaken for the creation of the set-up and the subsequent characterisation of the obtained results. The three-point characterisation, as illustrated in Chapter 2, section 2.4.3, adheres to the fundamental principle of establishing a flexible structure supported by two parallel points, thereby forming a surface. Subsequently, a third point applies force at the centre of the structure. It is important to note that the waveguide and the Bragg grating will not react the same way if they are below or above the neutral axis of the structure. A first representation of the experimental set-up for the characterisation of the three-point deformation can be observed in Figure 5.9
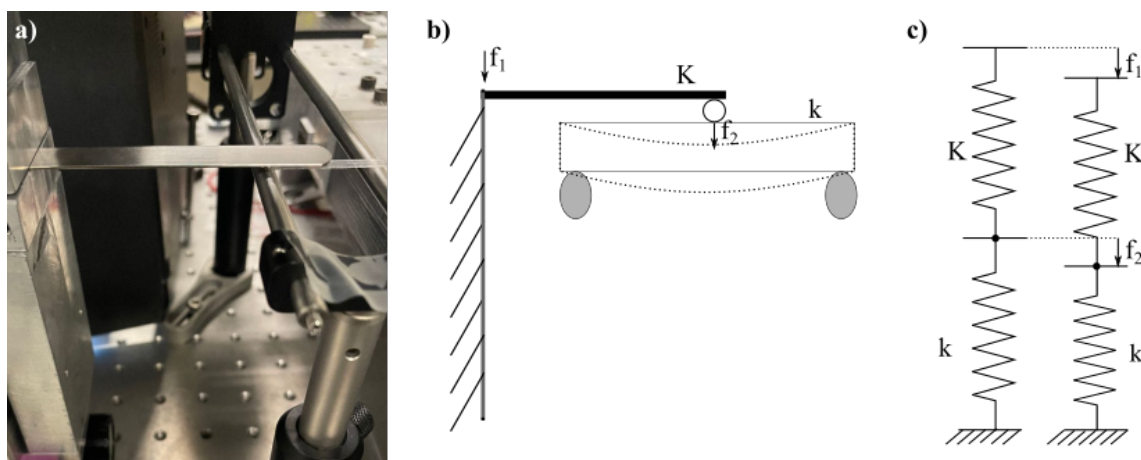


Figure 5.9:  Representation of the three-point set-up **(a)**.  Photographic **(b)**, schematical representation **(c)**, mechanical equivalent representation.

The behaviour of the Bragg grating varies depending on its position relative to the neutral axis. When situated above the neutral axis, the Bragg grating experiences compression, resulting in a smaller period and a corresponding shift towards shorter wavelengths. Conversely, when positioned below the neutral axis, the period of the Bragg grating increases, leading to a shift towards longer wavelengths. This means we will have two types of characterisation with the three-point mechanical flexion set-up. To perform this characterisation, we have built the set-up represented in Figure 5.10
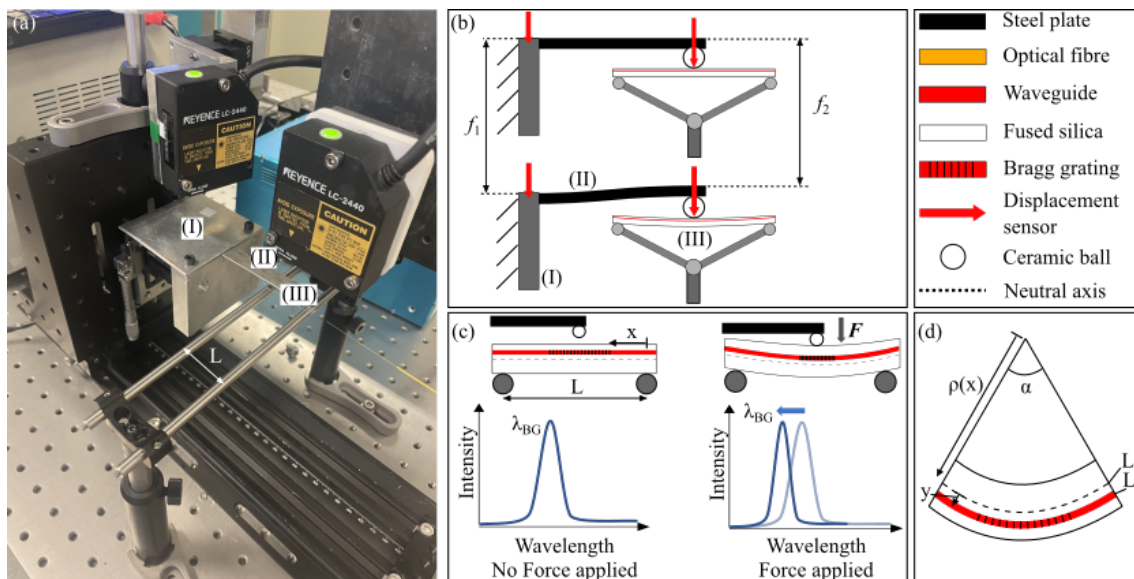


Figure 5.10: **(a)** Three-point flexural test bench. **(b)** A stainless steel beam with a ceramic ball is used to load the glass test beam. Two displacement sensors are used to monitor the stainless steel clamped side displacement $f_1$ and its ball end displacement $f_2$. **(c)** The test beam is placed on two fixed rods. The load is applied from the top at the centre of the beam. The Bragg grating sensor is placed close to the top surface of the beam, the applied strain is in compression. Therefore, the Bragg grating wavelength shift is negative. **(d)** Close view of the centre of the beam showing where the Bragg grating is inscribed.[145]

In the initial experiment depicted in Figure 5.10, a load is centrally applied to a horizontal beam supported by two fixed rods. The expression for the bending moment is as follows:

$$M(x) = \frac{F}{2}x \qquad x \in \left[0; \frac{L}{2}\right] \tag{5.3}$$

Here, $F$ represents the load at the centre of the beam, $x$ denotes the position from one fixed point, and $L$ is the distance between the two fixed points. The force is applied using a stainless steel cantilever beam secured to a vertically translating stage. To precisely apply the load to the glass beam, a ceramic ball is fixed to the tip of this cantilever beam.

Two Keyence LC-2440 laser displacement sensors measure the displacement of the vertical stage ($f_1$) and the depth at the ball's location ($f_2$). The stiffness of the stainless steel cantilever beam ($K$) is determined experimentally. This calibration process involves placing a fixed, high-precision scale (OHAUS YA102) beneath the ceramic ball and translating the vertical stage to apply the load.

$$K = \frac{F_{\text{scale}}}{f_1} \tag{5.4}$$

Then, the load applied to the glass beam can be expressed as:

$$F = K(f_1 - f_2) \tag{5.5}$$

The Bragg grating is positioned at the horizontal midpoint of the beam, specifically at $x = \frac{L}{2}$, and is located at a distance of 83 µm from the neutral axis. Given that its length is significantly smaller than the total length of the beam (30 mm), we can make the assumption:

$$\epsilon = \frac{KLy}{4EI}(f_1 - f_2) \tag{5.6}$$

Here, $I$ represent the inertia of the considered beam section. To assess the sensitivity of the Bragg grating to both tensile and compressive strains, the plate can be inverted, placing the Bragg grating in the opposite direction relative to the neutral axis.To characterise this Bragg grating, it is crucial to consider that the distance between the surface and the Bragg grating significantly influences its sensitivity. However, the design shape poses several challenges in modifying the waveguide location. To bring the waveguide as close as possible to the surface, three possibilities exist. First, a curved waveguide could be implemented to bring the signal in proximity to the surface. Alternatively, the waveguide can be positioned at the centre of the surface, with the option of excavating into the silica glass plate until reaching the upper part of the waveguide. The last option involves elevating the entrance of the optical fibre to a higher level, but this introduces a limitation of 70 µm due to the required cavity, measuring a square of 126 µm.

We have chosen to adjust the level of insertion of the optical fibre for several reasons. Firstly, the bending of the latter, as discussed in the optical results chapter, led to a noticeable degradation in signal quality. As a result, we have ruled out the bent waveguide as a viable method for bringing the waveguide closer to the surface. Additionally, we attempted to bring the surface closer to the waveguide but it resulted in a noticeable change in the spectrum quality compared to the initial waveguide configuration. In conclusion, after exploring various options for altering the waveguide location, we have determined that adjusting the level of insertion remains the most favourable and effective approach.

We consider $d$ the distance between the surface and the external part of the waveguide/core into the silica glass plate.

We aim to search if there is an optimal localisation for the centre of the optical fibre for the characterisation with mechanical flexures. It means that the distance between the neutral axis and the Bragg grating can be written as follows :

$$y = \frac{h}{2} - d \tag{5.7}$$

Then by using the Euler-Bernoulli equation, the evolution of the strain as a function of the location of the Bragg grating can be written :

$$\epsilon(y) = \frac{L(y) - L_0}{L_0} = \frac{y}{\rho} = \frac{My}{EI} = \frac{\sigma(y)}{E} \tag{5.8}$$

To optimize the strain, $x$ should align with the boundary conditions to maximize $M(x)$, and simultaneously, the parameter $d$ should be minimized. It is essential to note that, owing to manufacturing constraints, $d$ cannot be reduced to zero, as the Bragg grating must be positioned slightly below the surface rather than precisely at the surface. Consequently, the function $f(h)$ is anticipated to exhibit a maximum, signifying the compromise between maximizing $M(x)$ and adhering to manufacturing limitations. The first derivative of $f$ concerning $h$ leads to the value of this optimum.

$$h_{\text{opt}} = 3d \tag{5.9}$$

Considering that the thickness of the glass plate is 500 µm, the ideal position for the core of the waveguide is 167 µm. In the following experiments, we investigated the impact of waveguide depth on sensitivity to applied mechanical strain. Two depths were tested: the first at 167 µm from the center of the waveguide, and the second at 117 µm. The results of these experiments are depicted in Figure 5.11. Here $s_{\lambda\text{Bragg}}$ is the sensibility to the wavelength of the system and $s_{\epsilon\text{Bragg}}$ is the sensibility to the strain of the system.

In Figure 5.11, two characterisations based on the three-point mechanical flexure are presented. Figure 5.11a exhibits a characterisation with a sensitivity of 1.26 pm/$\mu\epsilon$, while Figure 5.11b shows a sensitivity of 1.27 pm/$\mu\epsilon$. Despite the difference, this is probably attributed to variations in material sensitivity or analyzer characteristics. It is noteworthy, that the curve profiles exhibit significant variations upon the depth of the waveguide. For a 167 µm waveguide, the experimental results demonstrate linearity throughout the measurement range. In contrast, for the 117 µm waveguide, the data exhibit linearity at small strains, whether negative or positive. Nevertheless, as strain levels increase, a divergence in linearity becomes evident, impacting sensitivity in these instances. The observed variation in the characterisations can be attributed to either a lack of precision in the spectrum, leading to imprecise characterisations, or a sensitivity limitation due to proximity to the surface, where the Bragg grating might struggle with higher strains. Given the possibility of the primary issue being the lack of precision, considering the problem of optical fibre insertion, we have chosen to explore the capability of the set-up to endure higher mechanical strain. This investigation is illustrated in Figure 5.12.
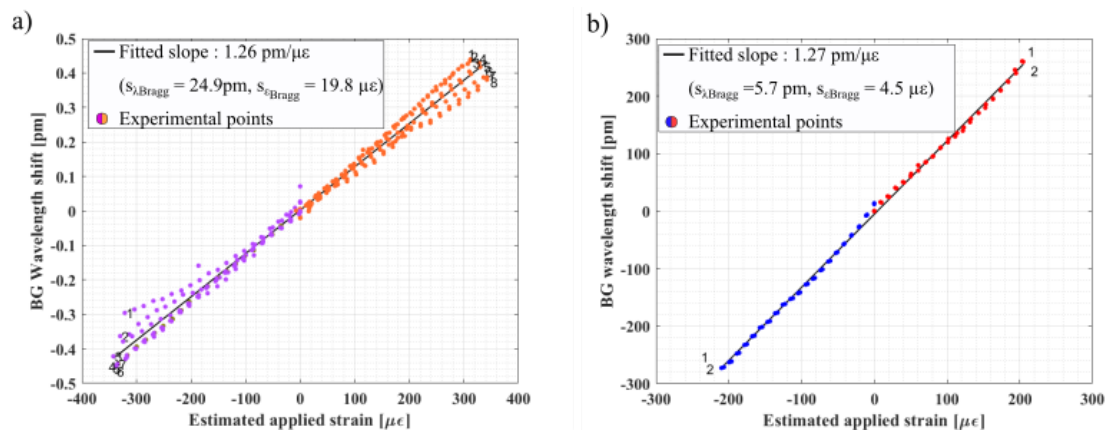
Figure 5.11: **(a)** Bragg wavelength shift evolution subject to the three-point Bragg grating when the waveguide is centred at 117 µm from the surface **(b)** Bragg wavelength shift of the evolution of the three points Bragg grating when the waveguide is centred at 167 µm from the surface.
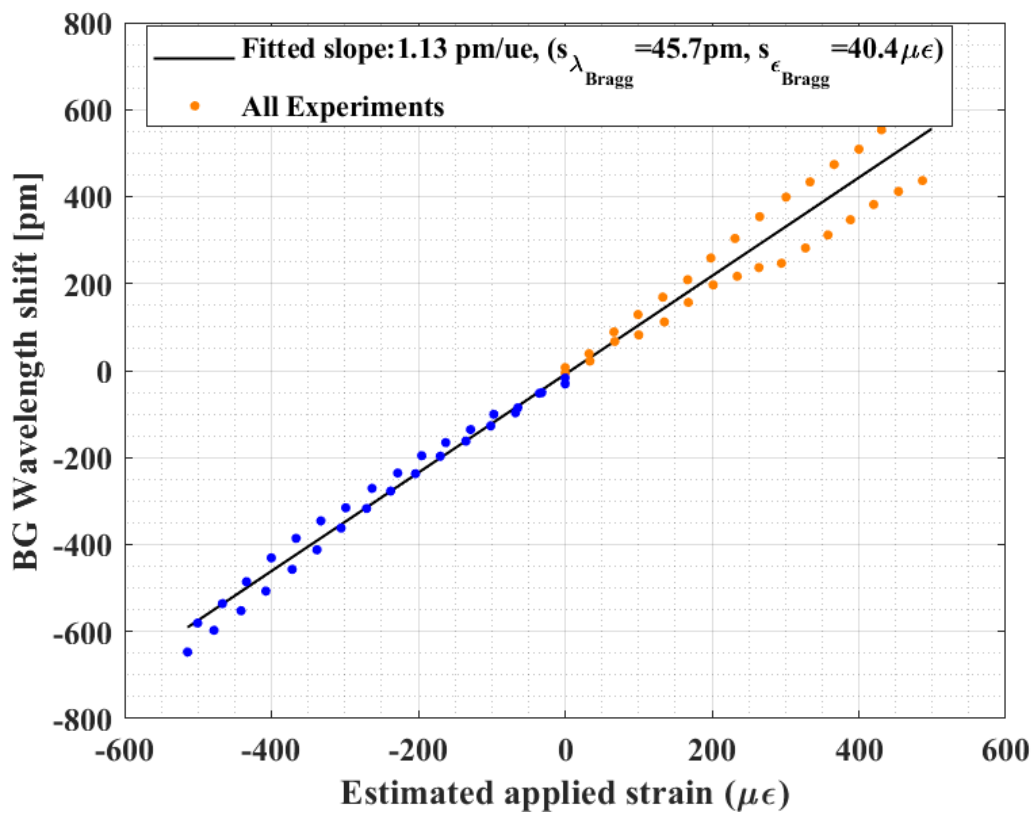


Figure 5.12: Representation of the evolution of the three-point characterisation under mechanical strain when the waveguide is located at 117 µm from the surface
.

Observations reveal a noticeable deviation from linearity in the characterisation beyond a strain of 200 µɛ. This deviation is particularly conspicuous for the 116 µm case and is likely associated with the height placement, potentially being too close to the surface. Such proximity may lead to a degradation in signal quality. Throughout this section, we have conducted an initial characterisation of the three-point flexures at various heights. It has been observed that at low strain, a linear and repeatable characterisation is achieved. However, at higher strain levels, there is a sensitivity difference dependent on the depth of the waveguide's core. Therefore, for the subsequent analysis, we will operate at a depth of 167 µm. In the next part, we will develop the same type of characterisation but instead of using a three-point system, we will use a cantilever beam.

## 5.4 Cantilever Beam Characterisation

Following the successful completion of the three-point flexure experiments, our next experimental phase involves using the same Bragg grating for mechanical deformation, now within the framework of a cantilever beam configuration. This phase introduces a comparable level of complexity when contrasted with the preceding three-point experiments. The complexity arises from the need for precise application of a vertical constraint, ensuring the structural integrity of the glass plate remains uncompromised. Consequently, the three-point mechanical characterisation set-up, which was previously employed, will undergo slight modifications to accommodate the cantilever beam configuration. In this section, we want to provide a detailed account of the procedures involved in establishing the cantilever beam set-up and subsequently characterising the obtained results. However, in contrast to being positioned between two metal bars, the glass plate is fixed at one extremity to a metallic structure, with force applied at the opposite extremity. Mechanical deformation in this arrangement is maximized when the structure is closest to the embedding, as depicted in Chapter 2, section 2.4.3. Transitioning to a cantilever beam configuration not only expands the scope of our mechanical deformation analysis but also introduces a new set of challenges and considerations. Through this approach, we aim to garner deeper insights into the nuanced behaviours of the waveguide and Bragg grating under varying conditions, thereby paving the way for a more comprehensive understanding of their mechanical responses.
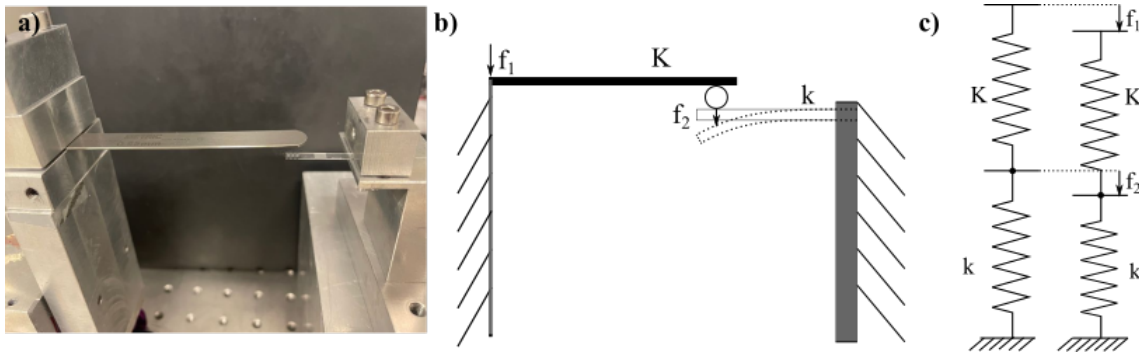
Figure 5.13: Representation of the cantilever beam set-up: Picture of the actual set-up **(a)**, schematical representation **(b)** and mechanical equivalent representation **(c)**.
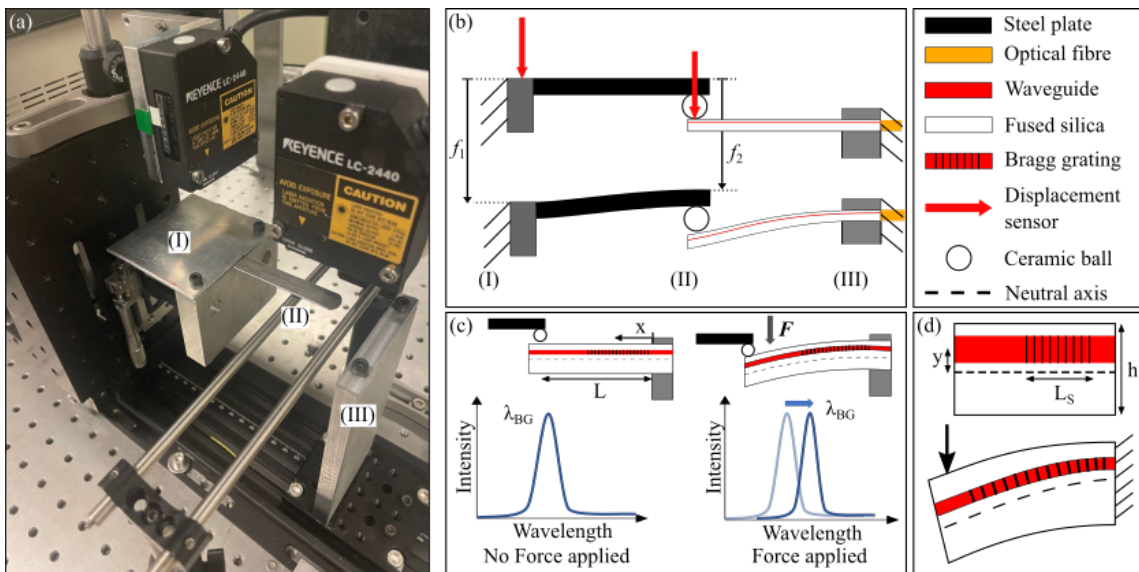


Figure 5.14: **(a)** Glass cantilever beam test bench. **(b)** A stainless steel beam with a ceramic ball is used to load the glass test beam. Two displacement sensors are used to monitor the stainless steel clamped side displacement $f_1$ and its ball end displacement $f_2$. **(c)** The test beam is clamped on the optical fibre side. The load is applied from the top at the tip of the cantilever beam. The Bragg grating sensor is placed close to the top surface of the beam, the applied strain is in compression. Therefore, the Bragg grating wavelength shift is negative. **(d)** Close view of the beam showing where the Bragg grating is inscribed close to the beam clamp position.

The behaviour of the Bragg grating varies depending on its position relative to the neutral axis. When situated below the neutral axis, the Bragg grating experiences compression, resulting in a smaller period and a corresponding shift towards shorter wavelengths. Conversely, when positioned above the neutral axis, the period of the Bragg grating increases, leading to a shift towards longer wavelengths. This means we will have two types of characterisation with the cantilever mechanical flexion. For this characterisation, we have built a set-up represented in Figure 5.13. In the experiment illustrated in Figure 5.14, the load is applied at the tip of the cantilever beam, which is horizontal and clamped on one side. The bending moment can be expressed as:

$$M(x) = F(L - x) \quad \text{for} \quad x \in [0; L] \tag{5.10}$$

Here $F$ represents the loading at the tip of the beam, $x$ denotes the position from the clamp, and $L$ is the distance between the clamp and the position where the load is applied.

The loading is applied in a similar manner to the three-point flexural test. To facilitate the characterisation of the Bragg grating sensitivity to strain in traction and compression, the beam can be reversed so that the Bragg grating is in the opposite direction from the neutral axis. Positioned close to the clamp ($x = 0$) at a distance $y$ from the neutral axis (83 µm), the Bragg grating, with a length much smaller than $L$ (approximately 24 mm), allows for the assumption:

$$\epsilon = \frac{KLy}{EI}(f_1 - f_2) \tag{5.11}$$

Here, $I$ denotes the inertia of the considered beam section, with $I = \frac{bh^3}{12}$, where $b$ represents the beam width (4 mm) and $h$ is the beam thickness (0.5 mm). The characterisation of the cantilever beam involves several crucial steps, with the initial consideration being the placement of the Bragg grating and the fibre. As elucidated in the preceding section, our observations indicated a tendency for less linearity in the results at high strain when positioned at a height of 117 µm. In the next section, the centre of the waveguide will be maintained at the same height as before, precisely at 167 µm. This decision is driven by the aim to enhance the linearity of results, particularly at higher strain levels, thus ensuring a more reliable characterisation of the cantilever beam. During the characterisation research, the initial challenge encountered was a lack of repeatability concerning sensitivity and linearity. It was subsequently identified that this issue was associated with the optical fibre, which was experiencing pressure from the clamp. This pressure, in turn, led to a disturbance in the signal as observed in Figure 5.15.

Figure 5.15 encompasses various crucial pieces of information, with the primary focus being on the influence of the clamping on the Bragg wavelength shift. In the initial design, clamping was initially applied directly on the interface between the optical fibre and the glass plate, the Bragg grating being at the beginning of the waveguide it was resulting in a modification of the incoming light and consequently affecting
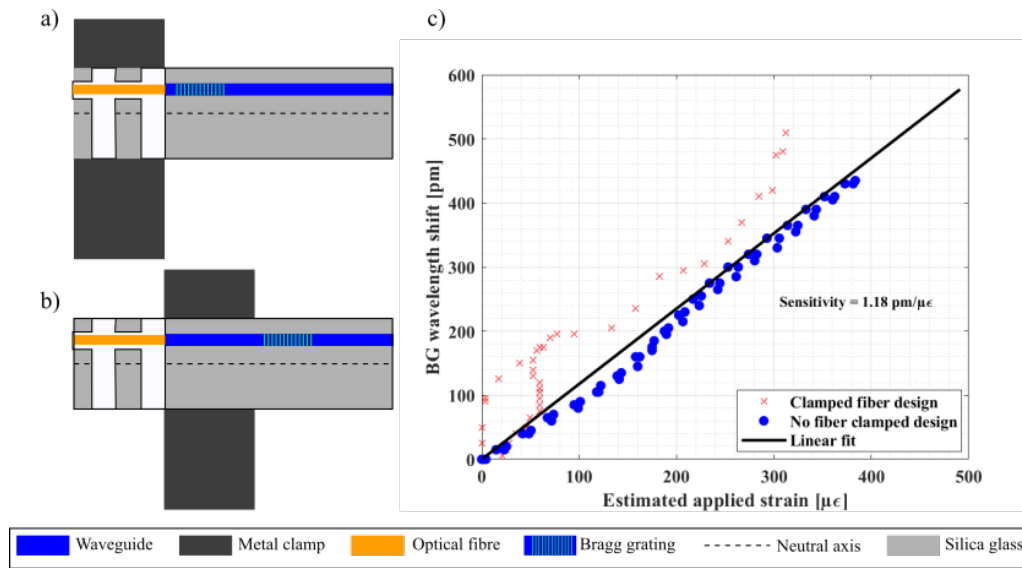
Figure 5.15: **(a)** Schematical representation of the first design of the cantilever beam **(b)** Schematical representation of the improved design of the cantilever beam where the fibre junction is outside of the clamping area **(c)** Results of characterisation representing the impact of the clamp.

the signal. In contrast, the second design opted for leaving a space between the end of the optical fibre and the beginning of the Bragg grating. This deliberate space was introduced to minimize the impact of clamping on the Bragg grating inducing an irregularity on the period and the overall characterisation, as illustrated in the "improved design". The next phase involves the characterisation of both faces of the glass plate to impart positive and negative mechanical strain. The detailed depiction of the cantilever beam characterisation is illustrated in Figure 5.16.
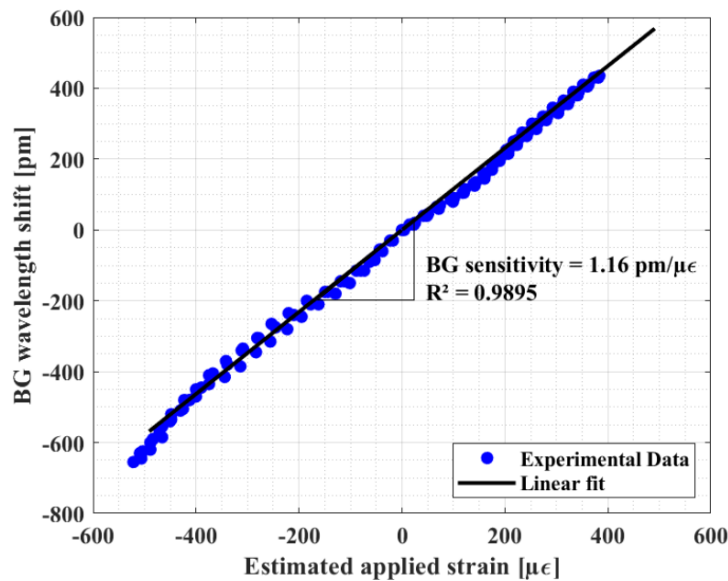


Figure 5.16: Results of characterisation of the cantilever beam.

The significance of Figure 5.16 lies in its portrayal of diverse outcomes derived from the cantilever beam experimentation. The graphical representation highlights the linear progression of the Bragg wavelength concerning strain; however, the observed sensitivity is found to be lower than anticipated.

In the preceding section, we investigated the constraints of the Femtoprint machine. This examination involved the fabrication of various optical structures, including the optical waveguide, which underwent characterisation in terms of dimension, mode, and birefringence. Additionally, a Bragg grating was developed and successfully demonstrated to be printable with varying periods at distinct locations along the optical waveguide, affirming the machine's capability to achieve this without compromising the quality of the waveguide.

This section is dedicated to leveraging the previously developed Bragg grating as a sensor for monitoring both temperature variations and the diverse mechanical deformations, namely pure traction, three-point flexion, and flexural cantilever beam deformations.

Subsequently, we undertook the characterisation steps, encountering distinct challenges in each scenario. Our initial focus was on temperature, deemed the most straightforward parameter to commence with due to its uncomplicated set-up and the absence of modifications required on the glass plate itself. However, the primary challenge in this context pertained to ensuring the precision of temperature measurements, leading us to employ two thermocouples to cross-verify the temperature readings at different points.

Regarding the various flexure mechanisms, we systematically characterised each—pure traction, three-point flexure, and cantilever beam—employing distinct set-ups. Notably, the sensitivities exhibited variations attributable to the unique characteristics of each set-up, including differing resolutions. Nevertheless, the diverse datasets illustrate a consistent sensitivity across the curves, as illustrated in Figure 5.17.
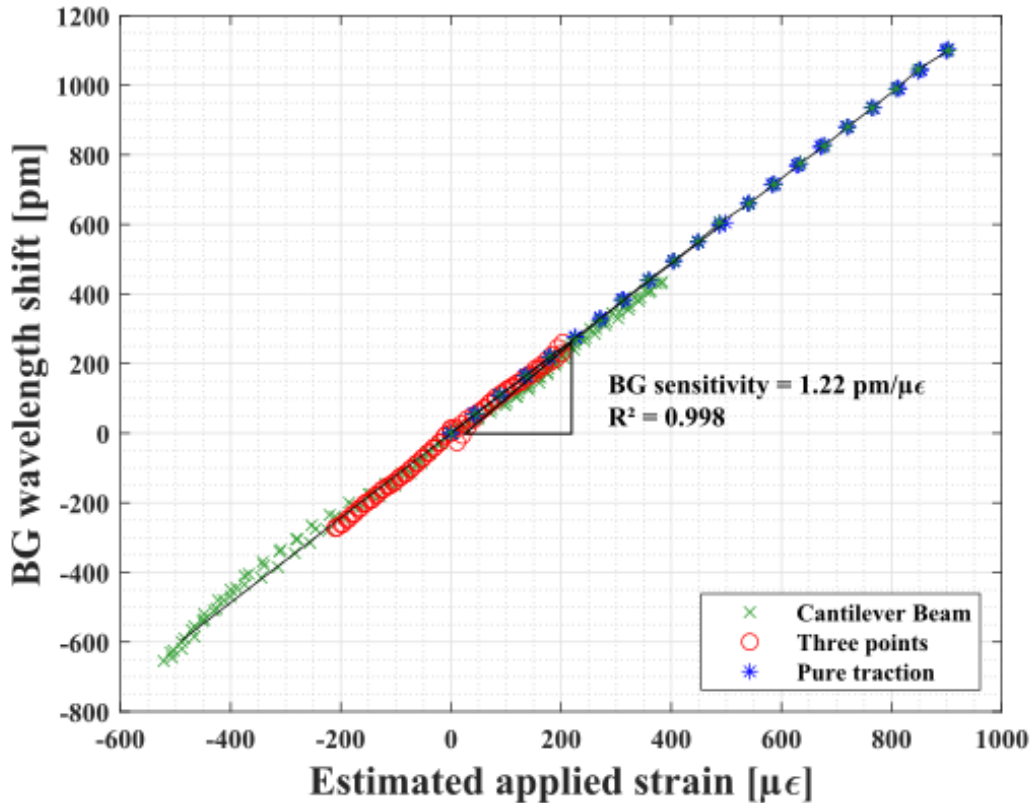
Figure 5.17: Results of the characterised Bragg grating sensitivity to strain for the three specimen designs that are detailed in previous Figures. Each experiment has been performed 4 times.

Given the theoretical sensitivity of approximately 1.24 pm/µε, it is notable that the observed sensitivities of the mechanical flexures align reasonably well with the existing literature. Any minor discrepancies may be attributed to variations in resolution across different set-ups. In summary, our findings affirm the successful creation of a robust sensor for mechanical flexures within a silica glass plate. This achievement is attributable to the structural modifications implemented, including the integration of an optical fibre and a Bragg grating.

## 5.5　Effect of the Refractive index surrounding environment

Optical fibres are sensitive to the surrounding environment through the inscription of tilted Bragg grating, providing information on the cladding mode and the refractive index of the ambient environment. We therefore attempted to inscribe a tilted Bragg grating into a planar waveguide constructed from a silica glass plate. Unfortunately, no other observable cladding mode or sensitivity to the surrounding environment was detected in our experiments.

Instead of tilting the Bragg grating, we opted for an alternative strategy: the creation of an open cavity going through the entire glass plate through etching. The designed separation between the edge of this cavity and the Bragg grating side, as determined by the Alphacam software, is 4 µm. However, it is essential to account for the passive etching effect during the seven-hour KOH etching process, which may potentially reduce this distance. We expect to identify the presence of a Bragg grating and explore the possibility of the modification of the evanescent wave based on the surrounding refractive index variations. The depth of the evanescent wave is estimated to be at 500 nm.

To assess the efficiency of the proposed method, the system was used in different developed solutions each possessing distinct refractive indices ranging from 1.35 to 1.40. These solutions were formulated using Lithium Chloride (LiCl), with the concentration C (g/mL) of LiCl in water determined by the following equation experimentally defined at the University of Mons :

$$RIU = 0.1963 \times C + 1.3332 \tag{5.12}$$

50 mL volume of solution was used to immerse the system with the highest refractive index. This immersion impacted the signal of the Bragg grating. In response to the negative impact on the Bragg grating signal during immersion, a modification to the test bench methodology was implemented. Rather than immersing the plate into the liquid, a horizontal configuration was adopted. The glass plate was positioned on a flat surface, and a micro pipette system was employed for the controlled addition and removal of the liquid, as represented in Figure 5.18.
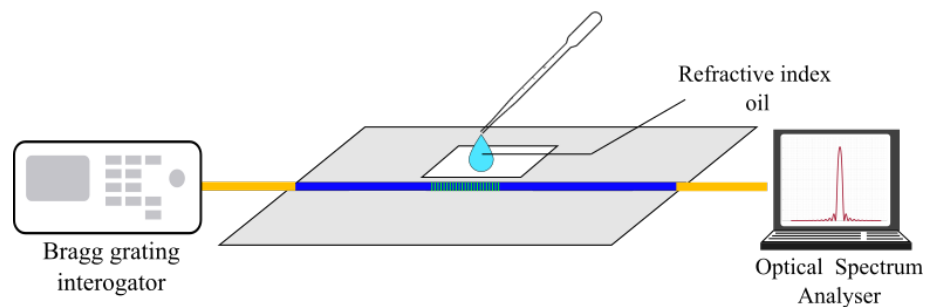


Figure 5.18: Graphical representation of the set-up used for the evolution of the Bragg wavelength as a function of different refractive index.

This adjustment aimed to mitigate the detrimental effects on the Bragg grating signal, providing a more controlled and non-immersive environment for accurate observations depicted in Figure 5.19.
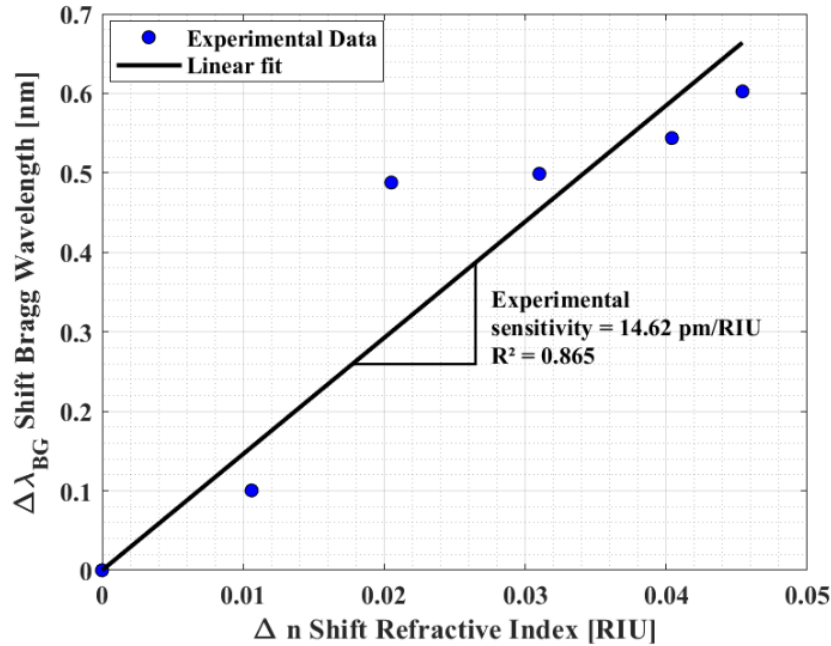
Figure 5.19: Graphical representation of the evolution of the Bragg wavelength as a function of the different refractive index.

Even if Figure 5.19 indicates a sensitivity of the Bragg grating to modification in the refractive index, it is essential to note that this observation has not been replicated sufficiently to obtain conclusive characterisation. We have tried to repeat the result several times but the results in terms of sensitivity were too different each time. This is due to the capacity of sensing the evanescent wave that was too short. We also believe that the space between the Bragg grating and the surrounding environment was too small to detect the evanescent wave. These results suggest to make attempts towards the characterisation of the refractive index sensitivity. It was not possible in the course of the thesis.

## 5.6   Conclusion

In this section, we want to summarise the different results that were obtained during the characterisation of the Bragg grating. After the creation of the fibre insertion, we made a waveguide and a Bragg grating directly within a silica glass plate with a femtosecond laser pulse.

The initial test we conducted aimed to assess the sensitivity of both the Bragg grating and the glass plate to ambient temperature variations. To achieve this, we heated the silica glass plate containing the waveguide and Bragg grating. Then, we tracked the changes in the Bragg wavelength as the temperature varied. This allowed us to deduce a global sensitivity of 10.51 pm/°C. Comparing this with the theoretical sensitivity, which is approximately 10 pm/°C, we observed that we are within the expected order of magnitude.

We have also performed three distinct structural characterisations to evaluate mechanical flexibility. The first utilized a flexible structure to examine traction characteristics. In the second, we employed a flexible structure within a three-point setup for characterisation. Lastly, the third characterisation involved the use of a flexible structure to assess mechanical flexibility through a cantilever beam structure. Then for each of these structures, we characterised its sensitivity to the strain applied with an optical response induced by the shift of the Bragg wavelength. We have obtained a global sensitivity of 1.22 pm/$\mu\epsilon$, which is a good result considering that the theoretical sensitivity was about 1.24 pm/$\mu\epsilon$.

In conclusion, we have successfully fabricated a monolithic structure using a femtosecond laser in a single process. Within this structure, we have incorporated both a waveguide and a Bragg grating, with optical fibre insertions following each component. Through precise characterisation involving temperature and mechanical strain, we determined a sensitivity of 10.51 pm/°C and 1.22 pm/$\mu\epsilon$ respectively. These findings represent a significant milestone towards potential future applications within the sensing domain. The flat glass sensor is preferred for applications requiring high sensitivity and specificity in a controlled environment, thanks to its stable and large surface. In contrast, the optical fibre sensor is ideal for remote, flexible, and robust monitoring in challenging environment, due to its small size and capability for long-distance measurements.

# Chapter 6

# Conclusions and perspectives

## Scientific Questions

In the introduction of our work, we posed several scientific questions that we aimed to address. We will now elaborate on each question and discuss our approach to answering them to the best of our ability.

**Can we successfully inscribe a Bragg grating and an optical waveguide into a silica glass plate ?** We successfully inscribed both a Bragg grating and an optical waveguide directly within a silica glass plate. However, to observe the Bragg grating, precise alignment between the optical fibre and the optical waveguide was necessary. To achieve this alignment, we designed insertion structures for the optical fibre. Once all three structures were in place, we proceeded to test the limitations of each. This development and its evaluation are detailed in Chapter 4 of our study.

**Are we able to accurately characterise the sensitivity of the Bragg grating to its surrounding environment, particularly the effects of temperature and mechanical flexure on the overall structure ?** Throughout this research, we endeavoured to estimate the sensitivity of our structure to various parameters. While our primary focus was on mechanical deformation, investigated through traction, cantilever beam, and three-point flexure tests, we also observed and characterised the sensitivity of the structure to temperature variations and changes in the surrounding refractive index. This characterisation is developed in Chapter 5 of our study.

**Can we identify and leverage this characterisation for future sensor applications ?** We identified several potential applications for our sensor, including its use with significant flexibility or its application as a tensile sensor. However, developing these applications to a high standard would necessitate additional time to enhance the quality of insertion and optimize the optical response. Nonetheless, these possibilities remain intriguing and innovative avenues for future exploration.

# Contributions

**Insertion of an optical fibre**. The primary contribution of this PhD research revolves around the innovative low-loss connection integration of an optical fibre within the structure of a silica glass plate. Initially, we considered directly inserting the optical fibre into ferrules and subsequently creating a holder for these ferrules. However, upon considering the etching time and the size of the ferrules, we realized this was not feasible. Consequently, we opted to explore an alternative approach by directly inserting the optical fibre into the silica glass plate. This accomplishment marks the initial phase of this PhD research, as it is directly inscribed into the silica glass plate. This structure, directly inscribed in silica glass, serves for the alignment of the optical fibre with the optical waveguide. The development of this structure represents a significant advancement for our sensor's creation.

**Creation of Optical Structures**. Throughout this PhD, we started the creation of two structures essential to the project: the waveguide and the Bragg grating.

To create an optical waveguide using a femtosecond laser pulse, it is necessary to slightly increase the refractive index of the silica glass plate. This process requires determining the lowest energy pulse of the laser, which, after thorough study, was identified to be at 130 nJ. However, aside from finding the lowest energy pulse, it is also crucial to identify the most optimal parameters for other inscription variables, such as the writing speed, laser path design, polarization, and repetition rate. Based on various studies conducted, we concluded that the optimal inscription parameters for an optical waveguide include a repetition rate of 1 MHz, a writing speed of 20 mm/min, perpendicular polarization, and a planar design of the laser path with a spacing of 0.5 µm between them. This inscription process enabled the formation of both straight and bent waveguides, a crucial aspect for future applications, especially in interferometry or surface sensing.

Subsequently, we aimed to inscribe Bragg gratings within the core of the silica glass waveguide. Initially, attempts were made to inscribe the Bragg gratings within the core of an optical fibre. These Bragg gratings were inscribed in a plane-by-plane manner, utilizing an energy of 150 nJ per pulse, a repetition rate of 1 MHz, and an inscription speed of 15 mm/min. However, a limitation encountered in this process was the resolution induced by the machine on the period of the Bragg grating. Nonetheless, we successfully created both second-order and fourth-order Bragg gratings. Additionally, efforts were made to inscribe both types of Bragg gratings within the same waveguide, and despite differences in intensity, both signals were detected and appeared on the optical spectrum. These optical parameters played a crucial role in characterising the developed structures.

**Characterisation of the Optical Waveguide**. Our study also centred on the fabrication and comprehensive characterisation of femtosecond laser-inscribed waveguides in silica glass. We explored various aspects of the optical waveguide characterisation. Initially, we examined them from an overhead perspective using a microscope and subsequently observed the output shape of the system using an infrared camera.

Additionally, we investigated the effect of waveguide birefringence on the signal by systematically analyzing its behaviour under two distinct polarization conditions during inscription. This investigation unveiled the interaction between laser polarization and resulting birefringence, highlighting notable variations in the optical properties of the waveguide.

**Characterisation of the Bragg Grating**. In the final phase of our study, we focused on investigating the behaviour of Bragg grating responses to variations in its surrounding environment. Specifically, we examined its response to temperature changes and various mechanical deformations. The sensitivity of the Bragg grating to temperature was estimated to be 10.51 pm/°C. Subsequently, we modified the shape of the silica glass plate to characterise the reaction of the Bragg sensing under mechanical deformations, including three-point flexure, cantilever beam bending, and pure traction. From these studies, we obtained a global sensitivity of 1.22 pm/µε. Through experimentation, we aimed to elucidate how these environmental factors influenced the performance and stability of the Bragg grating, leading to the deduction of a specific sensitivity.

# Perspectives

**Improvement of the insertion of the optical fibre**. Despite the enhancements in signal quality and optical fibre stability achieved through various insertions, the current system can still be improved. This limitation primarily comes from the rectangular shape of the optical fibre insertions, which does not align well with the circular design of the optical fibre itself. Due to the constraints of the Femtoprint technology available at the time, we were unable to develop a technique using a conical design. However, with the advent of new design capabilities, we are now able to explore and implement this operation, paving the way for improved system performance. One possibility would be to realise a more conical insertion instead of a rectangular one. This strongly improves the quality of the insertion because like this we would not have the possible damages on the surface of the optical fibre that may induce optical losses.

**Quality of the waveguide**. To enhance the quality of the waveguide, we could consider implementing a polishing technique. Currently, the chemical etching process leaves the surface at the end of the optical fibre unsuitable for optical coupling. This is why we choose to use a matching gel index to improve signal quality. However, an alternative approach could involve polishing the edge of the etched section. This polishing step has the potential to improve the quality of the transmitted signal by ensuring smoother and more precise surface characteristics. This polishing cannot be made with classical manual polishing techniques due to the small size of the cavities, so we have to find another way to produce it.

**Different possible characterisation**. In this manuscript, we extensively developed the sensitivity of the Bragg grating to mechanical deformations such as flexure and bending. However, one significant mechanical deformation that we have yet to investigate is torsion.

Torsion presents a compelling avenue for further characterisation of the Bragg grating within silica glass, offering potential insights into its behaviour under rotational stress. Integrating torsional deformation into our analysis would contribute valuable knowledge to our understanding of the Bragg grating's mechanical response. Although torsion is an important aspect of mechanical deformation, it can be challenging to characterise. When a straight waveguide is implemented, regardless of its orientation, the applied torsion should remain consistent, resulting in a larger period of the Bragg grating. One potential solution to induce a smaller period of the Bragg grating in silica glass during torsion is to create a helical waveguide. With a helical waveguide, torsion applied in the opposite direction of the waveguide's spiral will lead to a reduction in the period.

Another significant contribution that we were not able to reach was the development of biosensors. Our objective was to achieve a notable sensitivity to changes in the surrounding refractive index, a crucial requirement for creating effective biosensors. Once this sensitivity was achieved, our objective was to integrate a layer of gold at the surface of the refractometer, thereby inducing a possible plasmon and having precise information on the surface of the glass plate. While this goal remained beyond the scope of the current project, it represents a promising avenue for future research and applications of planar waveguides with Bragg gratings. By exploring this aspect further, we could potentially unlock new opportunities for biosensing technologies with enhanced performance and versatility.

If we had to summarize everything that we have done so far starting from a silica glass plate, we were able to inscribe an insertion for the optical fibre and align it. We have created an optical waveguide and a Bragg grating directly within this glass plate. This waveguide and this Bragg grating have been characterised in terms of birefringence as a function of the polarization of the inscription laser. They have also been characterised according to their sensitivity to the temperature (10.51 pm/°C) and to the mechanical deformation (1.22 pm/$\mu\epsilon$). The list of objectives that were reached is represented in Figure 6.1

Figure 6.1: Scheme summarizing the different objectives that were achieved during the Infuse project. It is important to take into account that the underline part has been realised by the other worker of the PhD project.

# Appendix A

# Further information about the glass

In this appendix, we will offer supplementary details concerning the theoretical framework of the manuscript. Specifically, we will contextualise our work within the existing literature, comparing various types of glass to the fused silica utilised throughout this PhD research in Figure A.1.

| Type of Glass | Chemical composition | Application | References |
|---|---|---|---|
| **Borosilicate Glass** | 74%$SiO_2$<br>1%$Al_2O_3$<br>15%$B_2O_3$<br>4%$Na_2O$<br>6%$PbO$ | Lens<br>Mirrors<br>Laboratory ware | [146] |
| **Ceramic Glass** | $SiO_2$<br>$Al_2O_3$<br>$B_2O_3$ | Stove window glass<br>Photosensitive applications | [147, 148] |
| *Silica glass* | $SiO_2$ | Vehicle window, Thermal barrier coatings | [106] |
| **Soda-lime glass** | 73%$SiO_2$<br>1%$Al_2O_3$<br>17%$Na_2O$<br>4%$MgO$<br>5%$CaO$ | Bottles<br>Containers | [149] |

Table A.1: List of the different types of glass.

Silica Glass: Also known as fused quartz or fused silica, silica glass is one of the most abundant types of glass. It is characterized by its high purity and excellent optical transparency in the ultraviolet, visible, and infrared regions. Silica glass is extensively used in optics, semiconductor manufacturing, and laboratory equipment.

Borosilicate Glass: Borosilicate glass contains boron trioxide, which imparts high thermal resistance and low thermal expansion properties. It is commonly used in laboratory glassware, cookware, and lighting applications. Borosilicate glass is known for its durability and resistance to chemical corrosion.

Soda-Lime Glass: Soda-lime glass is the most common type of glass, composed of silica, sodium oxide, and calcium oxide. It is used in various everyday items such as windows, bottles, and glass containers. Soda-lime glass is relatively inexpensive and easy to manufacture.

Ceramic glass, also known as vitroceramic or glass-ceramic, is a type of glass that has been heat-treated to induce crystallization. This process results in a material with properties of both glass and ceramics, such as high strength, thermal resistance, and chemical durability. Ceramic glass is commonly used in cookware, fireplace doors, and high-temperature applications.

Understanding the characteristics and applications of different types of glass is essential for selecting the most suitable material for a given purpose. Each type of glass offers distinct advantages and limitations, allowing for a wide range of practical and innovative uses.

It is important to take into account that if we would like to carry out the same operations as this PhD but with a different type of glass, the parameters for inscribing the optical waveguide, the Bragg grating, or creating nanograting would not be the same due to the chemical composition of the different types of glass. The etching time for the glass will also be different.

# Appendix B

# Optical Method

This appendix is dedicated to the presentation of the optical method and results for characterising the Bragg gratings. It plays a critical role in various fields such as telecommunications, sensing, and optical fibre technology. In this appendix, we will provide an overview of the different optical parameters and different spectra of Bragg grating with different lengths in silica glass in Table B.1.

## B.1 List of the Different Parameters for the Femtoprint Machine

In this section, we want to detail the list of parameters used for the inscription of optical waveguide and Bragg grating. But also the parameters used for the mechanical inscriptions such as the creation of nanograting and the parameters linked to the chemical etching.

| | | |
|---|---|---|
| Waveguide | Energy pulse | 130 nJ |
| | Writing Speed | 20 mm/min |
| | Repetition rate | 1000 kHz |
| | Polarization | Perpendicular |
| Bragg Grating | Energy pulse | 150 nJ |
| | Writing Speed | 15 mm/min |
| | Repetition rate | 1000 kHz |
| | Polarization | Perpendicular |
| Nanograting | Energy pulse | 230 nJ |
| | Writing Speed | 950 mm/min |
| | Repetition rate | 1000 kHz |
| | Polarization | Perpendicular |
| Etching parameter | Etching speed (radiated part) | 130 µm/h |
| | Etching speed (non-radiated part) | 0.7 µm/h |

Table B.1: List different parameters Femtoprint for the objective x20.

## B.2   Influence of the Width of the Bragg Grating and the Waveguide on the Signal

In this appendix we can find several measurements of different Bragg grating. The goal is to test if it is possible to reduce the width of the Bragg grating within the core of a 10 µm Waveguide. By reducing the width of the Bragg grating the goal is to progressively obtain a line by line Bragg grating and see how it answer in the current pattern of creation of the optical Bragg grating. The different examples of Bragg grating width are represented in Figure B.1
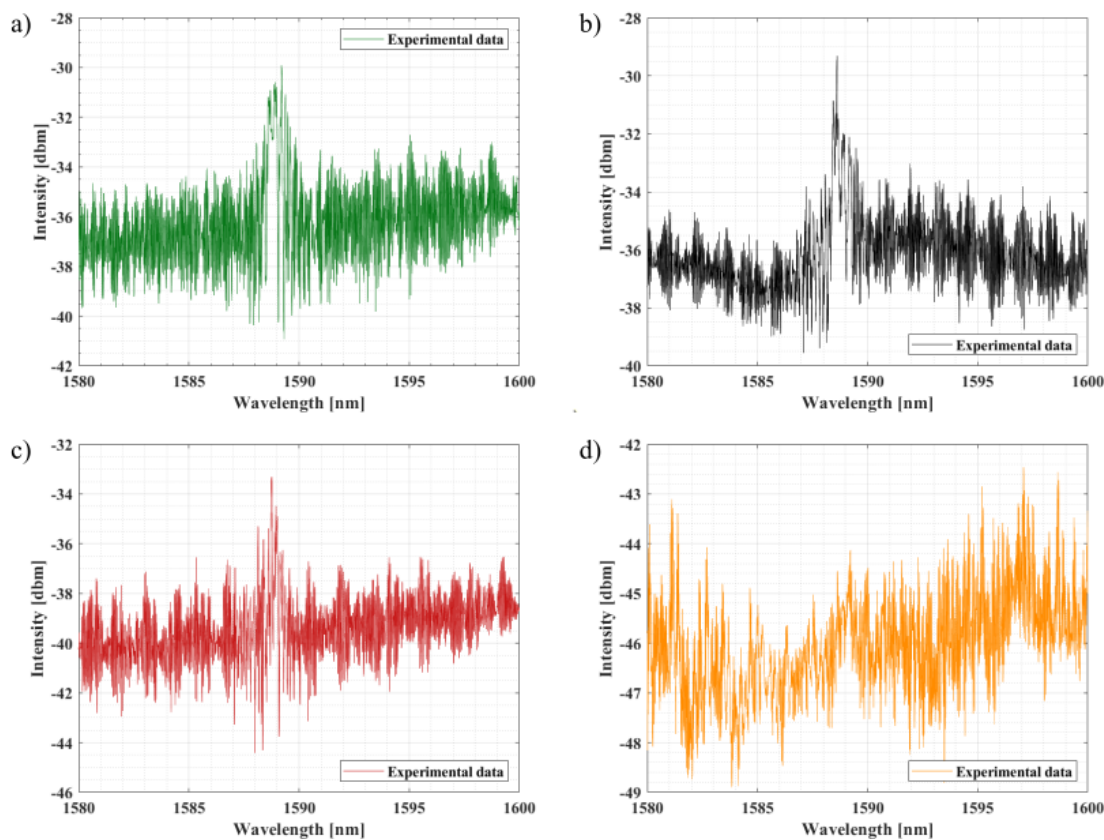


Figure B.1: Four different spectra obtained from a decrease of the size of the Bragg grating but keeping the same size of the waveguide. **(a)** 8µm Bragg grating. **(b)** 6 µm Bragg grating. **(c)** 3 µm Bragg grating. **(d)** 1 µm Bragg grating.

We represented several Bragg gratings, and we can see that the quality of the signal is not acceptable in all of them. However, in Figure B.1 (a), (b), and (c), we can observe a signal, whereas in Figure B.1 (d), there is no sign of any Bragg peak. Considering the width is 1 µm (which is the width of the voxel), it is the closest Bragg grating to a line-by-line design. The goal of this graph is to prove that we attempted to create a line-by-line design, but no signal with sufficient quality was observed. Considering the results and the quality of the signal obtained, we decided to stick with a plane-by-plane type of Bragg grating. In Figure B.2, we attempted

to reduce the size of both the waveguide and the Bragg grating within. We obtained a Bragg peak in every situation, indicating that the plane-by-plane method is the most efficient way to obtain a signal on the spectrum in our case. However, due to the shape and quality of the signal, we decided to maintain the size of 10 µm for the creation of the optical waveguide and the plane by plane Bragg grating.
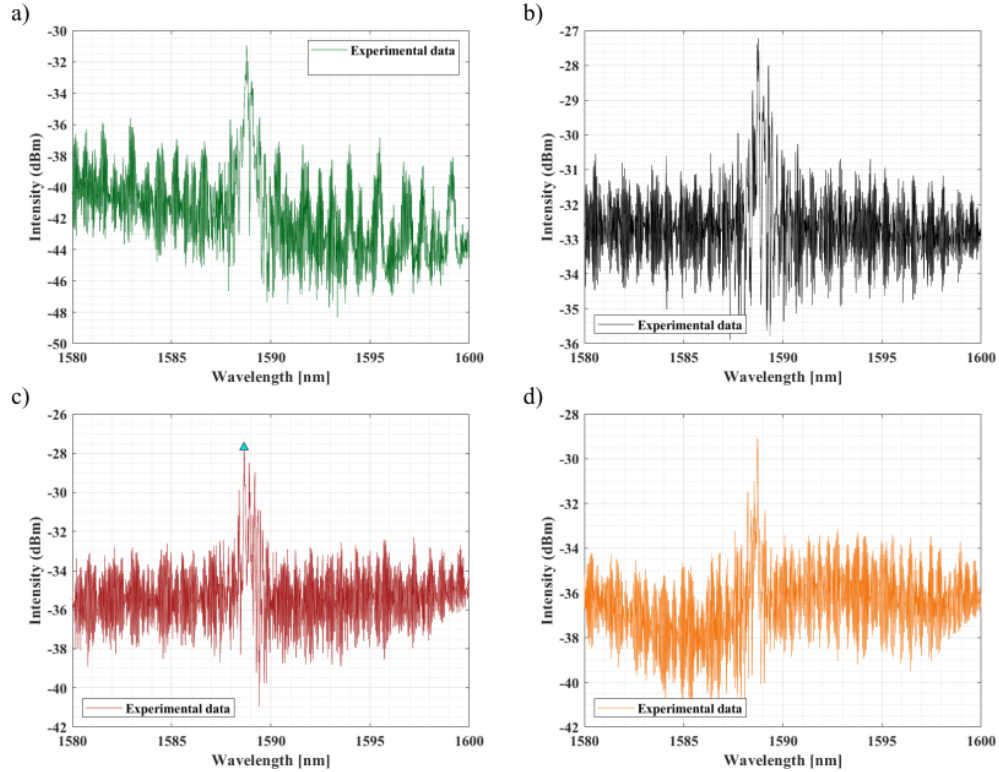


Figure B.2: Four different spectra obtained from a decrease of the size of the Bragg grating but also a decrease of the waveguide. **(a)** 8µm waveguide and 8µm Bragg grating **(b)** 6 µm waveguide and 6 µm Bragg grating **(c)** 4 µm waveguide and 4 µm Bragg grating **(d)** 2 µm waveguide and 2 µm Bragg grating.

The primary objective of this appendix is to explain why we decided to stick with the plane-by-plane Bragg grating instead of the line-by-line design. The experimental results and data to support our decision, highlighting the advantages and limitations of the line by line Bragg grating.

# Appendix C

# Characterisation

This appendix is dedicated to the presentation of codes and calibration used for Bragg grating mechanical characterisation. Bragg gratings play a critical role in various fields such as telecommunications, sensing, and optical fibre technology. Understanding the codes and calibration methods associated with Bragg grating characterisati is essential for assessing their performance and understanding results in applications. In this appendix, we will provide an overview of the different codes used and the calibration techniques employed to characterize Bragg gratings effectively.

**Calibration Three point setup**

To calibrate the experimental setup and determine the experimental stiffness of the material, we employed a unique approach. Instead of applying pressure directly to the silica glass, we opted to apply pressure to a weight balance. This allowed us to measure the difference in displacement between the two Keyence lasers, as depicted in the setup of the experimental chapter. By applying weight to the balance, we could deduce the overall force exerted by the setup. With this force known, we could then calculate the experimental stiffness constant of the material. This method provided a reliable means of characterizing the material's stiffness, which is crucial for understanding its mechanical properties and behaviour under different conditions. Following is an example of data for a calibration of a three-point flexure setup.

| X | Y | M | F | Δ | c |
|---|---|---|---|---|---|
| mm | mm | g | N | m | N/m |
| 0 | 0,051 | 0 | 0 | 0 | |
| 0,024 | 0,344 | 16,8 | 0,164808 | 0,000269 | 612,7 |
| 0,028 | 0,389 | 20,4 | 0,200124 | 0,00031 | 645,6 |
| 0,037 | 0,514 | 31,1 | 0,305091 | 0,000426 | 716,2 |
| 0,05 | 0,687 | 42,1 | 0,413001 | 0,000586 | 704,8 |
| 0,062 | 0,958 | 57,2 | 0,561132 | 0,000845 | 664,1 |
| 0,085 | 1,207 | 71,3 | 0,699453 | 0,001071 | 653,1 |
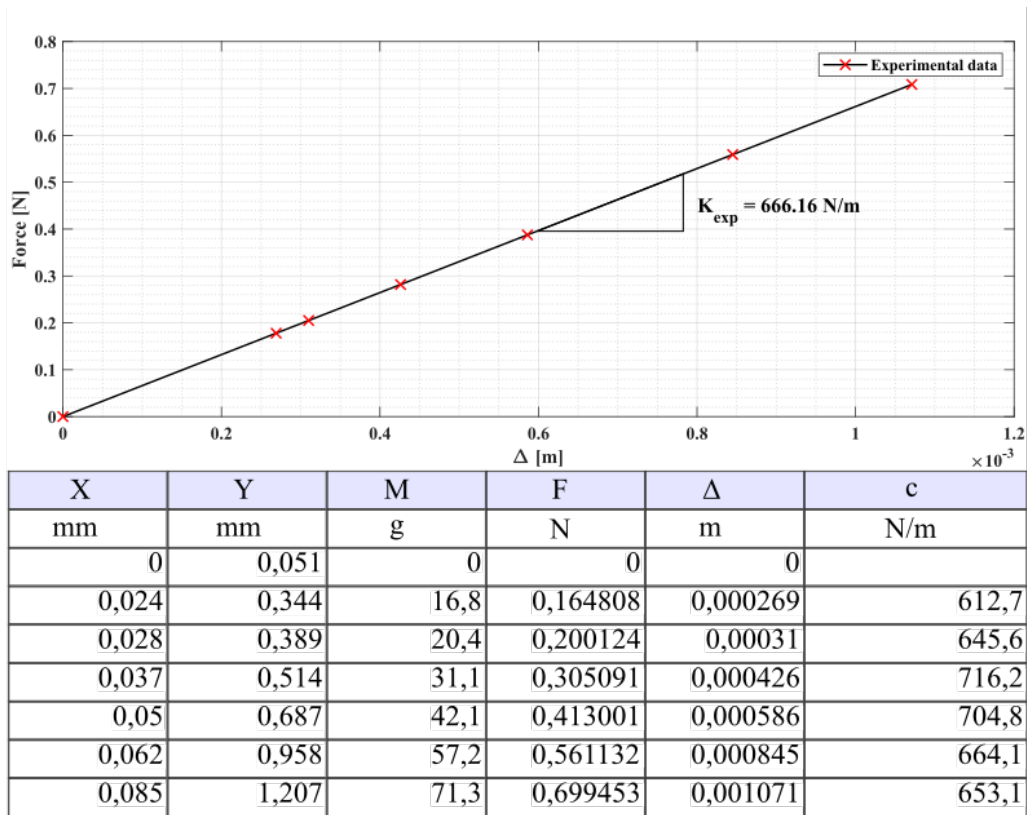
$$F = \frac{M \cdot 9{,}81}{1000}$$

Figure C.1: Data example calibration for a measurement of a three points flexure.

## C.1  characterisation programs

For the different characterisation, we have used several types of code that I will try to summarize in the next few lines. There were fours main important codes for the characterisation

**Bragg Wavelength Code**

The first code was used to deduce the Bragg Wavelength calculate the wavelength center of a Bragg grating reflected spectrum.

Input Values :

-Spectrum: The spectrum magnitude in dB.
-Noise: Noise level close to the spectrum of interest.
-Noise fine: Noise level for the second loop, usually set to 0 to prevent suppressing part of the Bragg reflected spectrum.
-Resolution: Wavelength resolution of the spectrum data.
-Window: Wavelength-reduced window, slightly larger than the expected Bragg re-

flected spectrum width.

It operates in two loops:

-First Loop: Integrates the spectrum with a given noise level (noise). It iterates through each point in the spectrum (Spectrum) and calculates the weighted sum (num) and the sum of weights (div) to find the center of gravity (CoG) of the spectrum.

-Second Loop (Optional): Integrates the spectrum in a wavelength-reduced window around the previously found Bragg grating (BG) center wavelength. This loop is activated if the window argument is greater than 0. It refines the CoG calculation in a narrower window (window is typically set slightly larger than the expected BG spectrum width). This refinement is to improve accuracy, especially in cases where the spectrum might be noisy.

The output of the function represent the index of the wavelength center of the Bragg grating reflected spectrum.

**Three Point Flexure Code** This code is performing data analysis and plotting based on experimental data. Let's break down what each part of the script is doing.

Input Values :

-$k_{metal}$: stiffness of the system in charge
-L: Length of the silica glass plate
-h: the thickness of the silica glass plate.
-b: Width of the silica glass plate
-d: position of the center of the waveguide
-E: in Pa, Young Modulus of glass
-delta: Difference between the location of the fixed and the flexible part
-lambdaBragg: The reflected wavelength

The first loop iterates through each element of the structure. Inside the loop, several calculations are performed using the fields of each element:

In each element there is a calculation of delta, F, I, sigma, fractionsigmamax, Fth, sigmaBragg, and strainBragg based on the inputs.

Then the script proceeds to plot data. Three different plots are generated:

Plot of Strain vs. Wavelength: The script plots strainBragg against lambdaBragg. It also fits a line to the data and displays the fit parameters and standard deviations.

Plot of Force vs. Absolute Strain: Similar to the previous plot, but now plotting force against the absolute value of strain.

Plot of Strain vs. Wavelength with Data Labels: This plot is similar to the first one, but it also labels each data point with the corresponding index i. The script analyze

experimental data related to strain and wavelength and generate plots to visualize the relationships between these variables

**Strain of the cantilever beam**

This code is performing data analysis and plotting based on experimental data obtained from the cantilever anaylisis.

Input Values :

-kmetal: stiffness of the system in charge
-L: Length of the silica glass plate
-h: the thickness of the silica glass plate.
-b: Width of the silica glass plate
-d: position of the center of the waveguide
-E: in Pa, Young Modulus of glass
-delta: Difference between the location of the fixed and the flexible part
-lambdaBragg: The reflected wavelength


This code is composed of a loop which calculates force F using a given constant kmetal.

Computes the angle Teta using the arctangent function, and computes the moment of inertia I.

Finally, it calculates strain epsilon based on F, L, E, and I, converting the result to microstrain. The commented-out code suggests further calculations related to stress and strain.

From this we are able to deduce the plot of the evolution of the Bragg wavelength as a function of the strain.

# Appendix D

# List of Scientific Production

## Journal Papers

**M. Tunon de Lara**, L. Amez Droz, K . Chah, P. Lambert, C. Collette, C. Caucheteur "Femtosecond pulse laser-engineered glass flexible structures instrumented with an in-built Bragg grating sensor." Optics Express 31.18 (2023): 29730.

L. Amez-Droz, **M. Tunon de Lara**, C. Collette, C. Caucheteur, P. Lambert. "Instrumented Flexible Glass Structure: A Bragg Grating Inscribed with Femtosecond Laser Used as a Bending Sensor." Sensors 23.19 (2023): 8018.

## Conference Proceedings

Production of an Optical Waveguide in Planar Glass Substrate Fabricated with Femtoprint. **M. Tunon de Lara**, K. Chah, L. Amez-Droz, P. Lambert, C. Collette, C. Caucheteur. SPIE Photonics Europe - Strasbourg April 2022

Synthesis of an optical waveguide in bulk silica with a femtosecond laser inscription and wet etching treatment. **M. Tunon de Lara Ramos**, L. Amez Droz, K. Chah, P. Lambert, C. Collette, C. Caucheteur. IEEE Photonics Society Benelux Chapter - Eindhoven - November 2022.

Bragg grating manufacturing in planar silica substrates. **M. Tunon de Lara**, K. Chah, L. Amez-Droz, P. Lambert, C. Collette, C. Caucheteur. SPIE Optics + Electronics, Prague - April 2023.

Femtosecond Laser Micro/Nano-Machining of Silica Glass Planar Substrates for the Production of Bragg Gratings. **M. Tunon de Lara**, K. Chah, L. Amez-Droz, P. Lambert, C. Collette, C. Caucheteur. European Workshop on Optical Fibre Sensors - Mons - May 2023.

Characterisation of optical waveguides engraved in silica planar substrates with a femtosecond laser process. **M. Tunon de Lara**, L. Amez Droz, K. Chah, P. Lambert, C. Collette, C. Caucheteur. IEEE Photonics Society Benelux Chapter - Gand - November 2023.

Fabrication of Bragg Gratings in Flat Silica Substrates Using the Femtoprint Device and Use for Sensing. **M. Tunon de Lara**, L. Amez-Droz, K. Chah, P. Lambert, C. Collette, C. Caucheteur. SPIE Photonic Europe - Strasbourg April 2024.

# Conference Presentation

## Oral presentation

**M. Tunon de Lara**, K. Chah, L. Amez-Droz, P. Lambert, C. Collette, C. Caucheteur. "Fabrication of optical waveguide using the femtoprint process", IEEE Photonics Society Benelux Chapter - Mons - November 2021.

**M. Tunon de Lara**, K. Chah, L. Amez-Droz, P. Lambert, C. Collette, C. Caucheteur. Bragg grating manufacturing in planar silica substrates. SPIE Optics Electronics - Prague - April 2023

**M. Tunon de Lara**, K. Chah, L. Amez-Droz, P. Lambert, C. Collette, C. Caucheteur. Fabrication of Bragg Gratings in Flat Silica Substrates Using the Femtoprint Device and Use for Sensing. SPIE Photonics Europe - Strasbourg - April 2024

## Posters

**M. Tunon de Lara**, K. Chah, L. Amez-Droz, P. Lambert, C. Collette, C. Caucheteur. Creation of optical structure in planar glass substrate fabricated with Femtoprint. Spie Photonics Europe - Strasbourg - April 2022

**M. Tunon de Lara**, K. Chah, L. Amez-Droz, P. Lambert, C. Collette, C. Caucheteur. Creation of optical structure in silica glass fabricated with Femtoprint. BePom-Bruxelles - September 2022

**M. Tunon de Lara**, K. Chah, L. Amez-Droz, P. Lambert, C. Collette, C. Caucheteur. Synthesis of an optical waveguide in bulk silica with a femtosecond laser inscription and wet etching treatment. IEEE Photonics Society Benelux Chapter - Eindhoven - November 2022

**M. Tunon de Lara**, K. Chah, L. Amez-Droz, P. Lambert, C. Collette, C. Caucheteur. Femtosecond laser pulses waveguide bragg grating silica glass wet. etching. EWOFS - Mons - May 2023

**M. Tunon de Lara**, K. Chah, L. Amez-Droz, P. Lambert, C. Collette, C. Caucheteur. Characterization of optical waveguides engraved in silica planar substrates with a femtosecond laser process. IEEE Photonics Society Benelux Chapter - Gand - November 2023

# Bibliography

[1] T. Juhasz, F. H. Loesel, R. M. Kurtz, C. Horvath, J. F. Bille, and G. Mourou, "Corneal refractive surgery with femtosecond lasers," *IEEE journal of selected topics in quantum electronics*, vol. 5, no. 4, pp. 902–910, 1999.

[2] W. Sekundo, K. Bönicke, P. Mattausch, and W. Wiegand, "Six-year follow-up of laser in situ keratomileusis for moderate and extreme myopia using a first-generation excimer laser and microkeratome," *Journal of Cataract & Refractive Surgery*, vol. 29, no. 6, pp. 1152–1158, 2003.

[3] T. A. Labutin, V. N. Lednev, A. A. Ilyin, and A. M. Popov, "Femtosecond laser-induced breakdown spectroscopy," *Journal of Analytical Atomic Spectrometry*, vol. 31, no. 1, pp. 90–118, 2016.

[4] Y. Bellouard, A. Champion, B. Lenssen, M. Matteucci, A. Schaap, M. Beresna, C. Corbari, M. Gecevičius, P. Kazansky, O. Chappuis, *et al.*, "The femtoprint project," *Journal of Laser Micro/Nanoengineering*, vol. 7, no. 1, pp. 1–10, 2012.

[5] C. Rulliere *et al.*, *Femtosecond laser pulses*. Springer, 2005.

[6] G. Keiser, *Optical fiber communications*, vol. 2. McGraw-Hill New York, 2000.

[7] M. Börner, "Mehrstufiges übertragungssystem für in pulscodemodulation dargestellte nachrichten," *Telefunken Patentverwertungsgesellschaft mbH*, vol. 11, 1967.

[8] F. Idachaba, D. U. Ike, and O. Hope, "Future trends in fiber optics communication," in *Proceedings of the World Congress on Engineering*, vol. 1, pp. 2–4, WCE London, UK, 2014.

[9] S. Miller, *Optical fiber telecommunications*. Elsevier, 2012.

[10] J. Li, D. R. Alexander, H. Zhang, U. Parali, D. W. Doerr, J. C. Bruce III, and H. Wang, "Propagation of ultrashort laser pulses through water," *Optics Express*, vol. 15, no. 4, pp. 1939–1945, 2007.

[11] R. Figueira, J. De Almeida, B. Ferreira, L. Coelho, and C. Silva, "Optical fiber sensors based on sol-gel materials: Design, fabrication and application in concrete structures," *Materials Advances*, vol. 2, 10 2021.

[12] E. Marcatili, "Extrapolation of snell's law to optical fibers," *JOSA*, vol. 63, no. 11, pp. 1372–1373, 1973.

[13] A. K. Ghatak and K. Thyagarajan, *An introduction to fiber optics.* Cambridge university press, 1998.

[14] E. Friebele, D. Griscom, and G. Sigel Jr, "Defect centers in a germanium-doped silica-core optical fiber," *Journal of Applied Physics*, vol. 45, no. 8, pp. 3424–3428, 1974.

[15] J. N. Brittingham, "Focus waves modes in homogeneous maxwell's equations: Transverse electric mode," *Journal of Applied Physics*, vol. 54, no. 3, pp. 1179–1189, 1983.

[16] W. A. Strauss, *Nonlinear wave equations.* No. 73, American Mathematical Soc., 1990.

[17] R. A. Pearson and A. F. Yee, "Toughening mechanisms in elastomer-modified epoxies: Part 2 microscopy studies," *Journal of materials science*, vol. 21, pp. 2475–2488, 1986.

[18] A. Rogers, Y. Zhou, and V. Handerek, "Computational polarization-optical time domain reflectometry for measurement of the spatial distribution of pmd in optical fibers," *Proceedings OFMC'97*, 1997.

[19] K. O. Hill and G. Meltz, "Fiber bragg grating technology fundamentals and overview," *Journal of Lightwave Technology*, vol. 15, no. 8, pp. 1263–1276, 1997.

[20] A. Othonos, "Fiber bragg gratings," *Review of scientific instruments*, vol. 68, no. 12, pp. 4309–4341, 1997.

[21] G. D. Marshall, M. Ams, and M. J. Withford, "Direct laser written waveguide-bragg gratings in bulk fused silica," *Optics Letters*, vol. 31, no. 18, pp. 2690–2691, 2006.

[22] T. Erdogan, "Fiber grating spectra," *Journal of lightwave technology*, vol. 15, no. 8, pp. 1277–1294, 1997.

[23] H. A. Haus and W. Huang, "Coupled-mode theory," *Proceedings of the IEEE*, vol. 79, no. 10, pp. 1505–1518, 1991.

[24] S. Ugale and V. Mishra, "Fiber bragg grating modeling, characterization and optimization with different index profiles," *International Journal of Engineering Science and Technology*, vol. 2, no. 9, pp. 4463–4468, 2010.

[25] A. Martinez, I. Y. Khrushchev, and I. Bennion, "Direct inscription of Bragg gratings in coated fibers by an infrared femtosecond laser," *Optics Letters*, vol. 31, no. 11, pp. 1603–1605, 2006.

[26] K. Chah, D. Kinet, M. Wuilpart, P. Mégret, and C. Caucheteur, "Femtosecond-laser-induced highly birefringent bragg gratings in standard optical fiber," *Optics Letters*, vol. 38, no. 4, pp. 594–596, 2013.

[27] K. Zhou, M. Dubov, C. Mou, L. Zhang, V. K. Mezentsev, and I. Bennion, "Line-by-line fiber bragg grating made by femtosecond laser," *IEEE Photonics Technology Letters*, vol. 22, no. 16, pp. 1190–1192, 2010.

[28] A. Theodosiou, A. Lacraz, A. Stassis, C. Koutsides, M. Komodromos, and K. Kalli, "Plane-by-plane femtosecond laser inscription method for single-peak bragg gratings in multimode cytop polymer optical fiber," *Journal of Lightwave Technology*, vol. 35, no. 24, pp. 5404–5410, 2017.

[29] G. Laffont, R. Cotillard, N. Roussel, R. Desmarchelier, and S. Rougeault, "Temperature resistant fiber bragg gratings for on-line and structural health monitoring of the next-generation of nuclear reactors," *Sensors*, vol. 18, no. 6, p. 1791, 2018.

[30] S. J. Mihailov, D. Grobnic, C. Hnatovsky, R. B. Walker, P. Lu, D. Coulas, and H. Ding, "Extreme environment sensing using femtosecond laser-inscribed fiber bragg gratings," *Sensors*, vol. 17, no. 12, p. 2909, 2017.

[31] C.-E. Athanasiou and Y. Bellouard, "A monolithic micro-tensile tester for investigating silicon dioxide polymorph micromechanics, fabricated and operated using a femtosecond laser," *Micromachines*, vol. 6, no. 9, pp. 1365–1386, 2015.

[32] X. Wang, H. Yu, P. Li, Y. Zhang, Y. Wen, Y. Qiu, Z. Liu, Y. Li, and L. Liu, "Femtosecond laser-based processing methods and their applications in optical device manufacturing: A review," *Optics & Laser Technology*, vol. 135, p. 106687, 2021.

[33] M. Malinauskas, A. Žukauskas, S. Hasegawa, Y. Hayasaki, V. Mizeikis, R. Buividas, and S. Juodkazis, "Ultrafast laser processing of materials: from science to industry," *Light: Science & Applications*, vol. 5, no. 8, pp. e16133–e16133, 2016.

[34] C. Hnatovsky, R. S. Taylor, P. P. Rajeev, E. Simova, V. R. Bhardwaj, D. M. Rayner, and P. B. Corkum, "Pulse duration dependence of femtosecond-laser-fabricated nanogratings in fused silica," *Applied Physics Letters*, vol. 87, p. 014104, 06 2005.

[35] A.-C. Tien, S. Backus, H. Kapteyn, M. Murnane, and G. Mourou, "Short-pulse laser damage in transparent materials as a function of pulse duration," *Physical Review Letters*, vol. 82, no. 19, p. 3883, 1999.

[36] M. Sakakura, Y. Lei, L. Wang, Y.-H. Yu, and P. G. Kazansky, "Ultralow-loss geometric phase and polarization shaping by ultrafast laser writing in silica glass," *Light: Science & Applications*, vol. 9, no. 1, pp. 1–10, 2020.

[37] M. Thiel, G. Flachenecker, and W. Schade, "Femtosecond laser writing of bragg grating waveguide bundles in bulk glass," *Optics Letters*, vol. 40, no. 7, pp. 1266–1269, 2015.

[38] K. O. Hill, Y. Fujii, D. C. Johnson, and B. S. Kawasaki, "Photosensitivity in optical fiber waveguides: Application to reflection filter fabrication," *Applied Physics Letters*, vol. 32, no. 10, pp. 647–649, 1978.

[39] G. Meltz, W. W. Morey, and W. H. Glenn, "Formation of bragg gratings in optical fibers by a transverse holographic method," *Optics letters*, vol. 14, no. 15, pp. 823–825, 1989.

[40] B. E. Saleh and M. C. Teich, "Fundamentals of photonics john wiley & sons," *Inc., Hoboken NJ*, vol. 2, 1991.

[41] K. O. Hill, B. Malo, F. Bilodeau, D. Johnson, and J. Albert, "Bragg gratings fabricated in monomode photosensitive optical fiber by uv exposure through a phase mask," *Applied Physics Letters*, vol. 62, no. 10, pp. 1035–1037, 1993.

[42] W. Yang, "Design of electrical capacitance tomography sensors," *Measurement science and technology*, vol. 21, no. 4, p. 042001, 2010.

[43] V. Schroeder, S. Savagatrup, M. He, S. Lin, and T. M. Swager, "Carbon nanotube chemical sensors," *Chemical reviews*, vol. 119, no. 1, pp. 599–663, 2018.

[44] D. W. Domaille, E. L. Que, and C. J. Chang, "Synthetic fluorescent sensors for studying the cell biology of metals," *Nature chemical biology*, vol. 4, no. 3, pp. 168–175, 2008.

[45] J. Cheon and J.-H. Lee, "Synergistically integrated nanoparticles as multi-modal probes for nanobiotechnology," *Accounts of chemical research*, vol. 41, no. 12, pp. 1630–1640, 2008.

[46] L. C. Clark Jr and C. Lyons, "Electrode systems for continuous monitoring in cardiovascular surgery," *Annals of the New York Academy of sciences*, vol. 102, no. 1, pp. 29–45, 1962.

[47] V. K. Khanna, *Nanosensors: physical, chemical, and biological.* CRC press, 2021.

[48] S. A. Abid, A. A. Muneer, I. M. Al-Kadmy, A. A. Sattar, A. M. Beshbishy, G. E.-S. Batiha, and H. F. Hetta, "Biosensors as a future diagnostic approach for covid-19," *Life sciences*, vol. 273, p. 119117, 2021.

[49] J. K. Sahota, N. Gupta, and D. Dhawan, "Fiber bragg grating sensors for monitoring of physical parameters: A comprehensive review," *Optical Engineering*, vol. 59, no. 6, pp. 060901–060901, 2020.

[50] S. J. Mihailov, "Fiber bragg grating sensors for harsh environments," *Sensors*, vol. 12, no. 2, pp. 1898–1918, 2012.

[51] A. Othonos, K. Kalli, D. Pureur, and A. Mugnier, "Fibre bragg gratings," in *Wavelength Filters in Fibre Optics*, pp. 189–269, Springer, 2006.

[52] O. A. Bauchau and J. I. Craig, "Euler-bernoulli beam theory," in *Structural analysis*, pp. 173–221, Springer, 2009.

[53] M. A. Hopcroft, W. D. Nix, and T. W. Kenny, "What is the young's modulus of silicon?," *Journal of microelectromechanical systems*, vol. 19, no. 2, pp. 229–238, 2010.

[54] J. Rychlewski, "On hooke's law," *Journal of Applied Mathematics and Mechanics*, vol. 48, no. 3, pp. 303–314, 1984.

[55] L. L. Howell, "Compliant mechanisms," in *21st Century Kinematics: The 2012 NSF Workshop*, pp. 189–216, Springer, 2013.

[56] A. Yariv and P. Yeh, *Optical waves in crystals*, vol. 5. Wiley New York, 1984.

[57] J. F. Bauters, M. J. Heck, D. D. John, J. S. Barton, C. M. Bruinink, A. Leinse, R. G. Heideman, D. J. Blumenthal, and J. E. Bowers, "Planar waveguides with less than 0.1 db/m propagation loss fabricated with wafer bonding," *Optics express*, vol. 19, no. 24, pp. 24090–24101, 2011.

[58] M. Bozzi, A. Georgiadis, and K. Wu, "Review of substrate-integrated waveguide circuits and antennas," *IET Microwaves, Antennas & Propagation*, vol. 5, no. 8, pp. 909–920, 2011.

[59] K. M. Davis, K. Miura, N. Sugimoto, and K. Hirao, "Writing waveguides in glass with a femtosecond laser," *Optics letters*, vol. 21, no. 21, pp. 1729–1731, 1996.

[60] H. Ma, A.-Y. Jen, and L. R. Dalton, "Polymer-based optical waveguides: materials, processing, and devices," *Advanced materials*, vol. 14, no. 19, pp. 1339–1365, 2002.

[61] S. Wang, V. Vaidyanathan, and B. Borden, "Polymer optical channel waveguide components fabricated by using a laser direct writing system," *Journal of Applied Science & Engineering Technology*, vol. 3, 2009.

[62] V. Kozlov, V. Bulović, P. Burrows, and S. Forrest, "Laser action in organic semiconductor waveguide and double-heterostructure devices," *Nature*, vol. 389, no. 6649, pp. 362–364, 1997.

[63] M. Ferrera, L. Razzari, D. Duchesne, R. Morandotti, Z. Yang, M. Liscidini, J. Sipe, S. Chu, B. E. Little, and D. J. Moss, "Low-power continuous-wave nonlinear optics in doped silica glass integrated waveguide structures," *Nature photonics*, vol. 2, no. 12, pp. 737–740, 2008.

[64] Y. Bellouard, A. Said, M. Dugan, and P. Bado, "Fabrication of high-aspect ratio, micro-fluidic channels and tunnels using femtosecond laser pulses and chemical etching," *Optics Express*, vol. 12, no. 10, pp. 2120–2129, 2004.

[65] Y. Bellouard, "On the bending strength of fused silica flexures fabricated by ultrafast lasers," *Optical Materials Express*, vol. 1, no. 5, pp. 816–831, 2011.

[66] M. Beresna, M. Gecevičius, and P. G. Kazansky, "Ultrafast laser direct writing and nanostructuring in transparent materials," *Advances in Optics and Photonics*, vol. 6, no. 3, pp. 293–339, 2014.

[67] S. Rajesh and Y. Bellouard, "Towards fast femtosecond laser micromachining of fused silica: The effect of deposited energy.," *Optics Express*, vol. 18, no. 20, pp. 21490–21497, 2010.

[68] K. Sugioka and Y. Cheng, "Femtosecond laser three-dimensional micro-and nanofabrication," *Applied Physics Reviews*, vol. 1, no. 4, p. 041303, 2014.

[69] D. Krol, "Femtosecond laser modification of glass," *Journal of Non-Crystalline Solids*, vol. 354, no. 2-9, pp. 416–424, 2008.

[70] E. Güler, G. Uğur, Ş. Uğur, and M. Güler, "A theoretical study for the band gap energies of the most common silica polymorphs," *Chinese Journal of Physics*, vol. 65, pp. 472–480, 2020.

[71] I. Choi, S. Min, J.-I. Shim, and D.-S. Shin, "Understanding and evaluating the mean photon energy and the external quantum efficiency of light-emitting diodes," *IET Optoelectronics*, vol. 17, no. 1, pp. 32–37, 2023.

[72] G. S. He, L.-S. Tan, Q. Zheng, and P. N. Prasad, "Multiphoton absorbing materials: molecular designs, characterizations, and applications," *Chemical reviews*, vol. 108, no. 4, pp. 1245–1330, 2008.

[73] A. P. Joglekar, H.-h. Liu, G. Spooner, E. Meyhöfer, G. Mourou, and A. Hunt, "A study of the deterministic character of optical damage by femtosecond laser pulses and applications to nanomachining," *Applied Physics B*, vol. 77, no. 1, pp. 25–30, 2003.

[74] M. Will, S. Nolte, B. N. Chichkov, and A. Tünnermann, "Optical properties of waveguides fabricated in fused silica by femtosecond laser pulses," *Applied Optics*, vol. 41, no. 21, pp. 4360–4364, 2002.

[75] J. Canning, M. Lancry, K. Cook, A. Weickman, F. Brisset, and B. Poumellec, "Anatomy of a femtosecond laser processed silica waveguide," *Optical Materials Express*, vol. 1, no. 5, pp. 998–1008, 2011.

[76] R. R. Gattass and E. Mazur, "Femtosecond laser micromachining in transparent materials," *Nature Photonics*, vol. 2, no. 4, pp. 219–225, 2008.

[77] X. Liu, D. Du, and G. Mourou, "Laser ablation and micromachining with ultrashort laser pulses," *IEEE Journal of Quantum Electronics*, vol. 33, no. 10, pp. 1706–1716, 1997.

[78] R. S. Taylor, C. Hnatovsky, E. Simova, D. M. Rayner, M. Mehandale, V. Bhardwaj, and P. Corkum, "Ultra-high resolution index of refraction profiles of femtosecond laser modified silica structures," *Optics Express*, vol. 11, no. 7, pp. 775–781, 2003.

[79] S. Kiyama, S. Matsuo, S. Hashimoto, and Y. Morihira, "Examination of etching agent and etching mechanism on femotosecond laser microfabrication of channels inside vitreous silica substrates," *The Journal of Physical Chemistry C*, vol. 113, no. 27, pp. 11560–11566, 2009.

[80] A. Marcinkevičius, S. Juodkazis, M. Watanabe, M. Miwa, S. Matsuo, H. Misawa, and J. Nishii, "Femtosecond laser-assisted three-dimensional microfabrication in silica," *Optics letters*, vol. 26, no. 5, pp. 277–279, 2001.

[81] E. Casamenti, S. Pollonghini, and Y. Bellouard, "Few pulses femtosecond laser exposure for high efficiency 3d glass micromachining," *Optics Express*, vol. 29, no. 22, pp. 35054–35066, 2021.

[82] A. Plech, V. Kotaidis, M. Lorenc, and J. Boneberg, "Femtosecond laser near-field ablation from gold nanoparticles," *Nature Physics*, vol. 2, no. 1, pp. 44–47, 2006.

[83] D. S. Correa, M. R. Cardoso, V. Tribuzi, L. Misoguti, and C. R. Mendonca, "Femtosecond laser in polymeric materials: microfabrication of doped structures and micromachining," *IEEE Journal of Selected Topics in Quantum Electronics*, vol. 18, no. 1, pp. 176–186, 2011.

[84] L. Li, W. Kong, and F. Chen, "Femtosecond laser-inscribed optical waveguides in dielectric crystals: a concise review and recent advances," *Advanced Photonics*, vol. 4, no. 2, p. 024002, 2022.

[85] G.-L. Roth, S. Hessler, S. Kefer, M. Girschikofsky, C. Esen, and R. Hellmann, "Femtosecond laser inscription of waveguides and bragg gratings in transparent cyclic olefin copolymers," *Optics Express*, vol. 28, no. 12, pp. 18077–18084, 2020.

[86] E. Ippen, C. Shank, and A. Dienes, "Passive mode locking of the cw dye laser," *Applied Physics Letters*, vol. 21, no. 8, pp. 348–350, 1972.

[87] C. V. Shank, "Physics of dye lasers," *Reviews of Modern Physics*, vol. 47, no. 3, p. 649, 1975.

[88] D. Strickland and G. Mourou, "Compression of amplified chirped optical pulses," *Optics communications*, vol. 55, no. 6, pp. 447–449, 1985.

[89] G. A. Mourou, C. P. Barry, and M. D. Perry, "Ultrahigh-intensity lasers: Physics of the extreme on a tabletop," *Physics today*, vol. 51, no. 1, pp. 22–28, 1998.

[90] F. Duarte and A. Costela, "Lasers | dye lasers," in *Encyclopedia of Modern Optics* (R. D. Guenther, ed.), pp. 400–414, Oxford: Elsevier, 2005.

[91] C. Zhou, "Chirped pulse amplification: review and prospective from diffractive optics," *Chinese Optics Letters*, vol. 18, no. 11, p. 110502, 2020.

[92] B. N. Chichkov, C. Momma, S. Nolte, F. Von Alvensleben, and A. Tünnermann, "Femtosecond, picosecond and nanosecond laser ablation of solids," *Applied physics A*, vol. 63, pp. 109–115, 1996.

[93] Z. Lin and M. Hong, "Femtosecond laser precision engineering: from micron, submicron, to nanoscale," *Ultrafast Science*, vol. 2021, 2021.

[94] P. Pronko, S. Dutta, J. Squier, J. Rudd, D. Du, and G. Mourou, "Machining of sub-micron holes using a femtosecond laser at 800 nm," *Optics communications*, vol. 114, no. 1-2, pp. 106–110, 1995.

[95] S. Preuss, A. Demchuk, and M. Stuke, "Sub-picosecond uv laser ablation of metals," *Applied physics A*, vol. 61, pp. 33–37, 1995.

[96] W. Kautek and J. Krüger, "Femtosecond pulse laser ablation of metallic, semiconducting, ceramic, and biological materials," in *Laser materials processing: industrial and microelectronics applications*, vol. 2207, pp. 600–611, SPIE, 1994.

[97] S. Noël, J. Hermann, and T. Itina, "Investigation of nanoparticle generation during femtosecond laser ablation of metals," *Applied Surface Science*, vol. 253, no. 15, pp. 6310–6315, 2007.

[98] A. Y. Vorobyev and C. Guo, "Direct femtosecond laser surface nano/microstructuring and its applications," *Laser & Photonics Reviews*, vol. 7, no. 3, pp. 385–407, 2013.

[99] Y. Bellouard, E. Barthel, A. Said, M. Dugan, and P. Bado, "Scanning thermal microscopy and raman analysis of bulk fused silica exposed to low-energy femtosecond laser pulses," *Optics Express*, vol. 16, no. 24, pp. 19520–19534, 2008.

[100] T. Uchino, Y. Kitagawa, and T. Yoko, "Structure, energies, and vibrational properties of silica rings in sio 2 glass," *Physical Review B*, vol. 61, no. 1, p. 234, 2000.

[101] D. Tan, Z. Wang, B. Xu, and J. Qiu, "Photonic circuits written by femtosecond laser in glass: improved fabrication and recent progress in photonic devices," *Advanced Photonics*, vol. 3, no. 2, pp. 024002–024002, 2021.

[102] V. Apostolopoulos, L. Laversenne, T. Colomb, C. Depeursinge, R. Salathé, M. Pollnau, R. Osellame, G. Cerullo, and P. Laporta, "Femtosecond-irradiation-induced refractive-index changes and channel waveguiding in bulk ti3+: Sapphire," *Applied Physics Letters*, vol. 85, no. 7, pp. 1122–1124, 2004.

[103] C.-H. Lin, L. Jiang, Y. Chai, H. Xiao, S.-J. Chen, and H. Tsai, "Fabrication of microlens arrays in photosensitive glass by femtosecond laser direct writing," *Applied Physics A*, vol. 97, pp. 751–757, 2009.

[104] A. Szameit, D. Blömer, J. Burghoff, T. Schreiber, T. Pertsch, S. Nolte, A. Tünnermann, and F. Lederer, "Discrete nonlinear localization in femtosecond laser written waveguides in fused silica," *Optics express*, vol. 13, no. 26, pp. 10552–10557, 2005.

[105] R. R. Thomson, H. T. Bookey, N. Psaila, S. Campbell, D. T. Reid, S. Shen, A. Jha, and A. K. Kar, "Internal gain from an erbium-doped oxyfluoride-silicate glass waveguide fabricated using femtosecond waveguide inscription," *IEEE Photonics Technology Letters*, vol. 18, no. 14, pp. 1515–1517, 2006.

[106] M. Tunon de Lara, K. Chah, L. Amez-Droz, P. Lambert, C. Collette, *et al.*, "Production of optical waveguide in planar glass substrate fabricated with femtoprint," in *Proc. of SPIE Vol*, vol. 12142, pp. 121421K–1, 2022.

[107] J. R. Grenier, L. A. Fernandes, and P. R. Herman, "Femtosecond laser writing of optical edge filters in fused silica optical waveguides," *Optics express*, vol. 21, no. 4, pp. 4493–4502, 2013.

[108] F. Chen and J. V. de Aldana, "Optical waveguides in crystalline dielectric materials produced by femtosecond-laser micromachining," *Laser & Photonics Reviews*, vol. 8, no. 2, pp. 251–275, 2014.

[109] V. De Michele, M. Royon, E. Marin, A. Alessi, A. Morana, A. Boukenter, M. Cannas, S. Girard, and Y. Ouerdane, "Near-ir-and uv-femtosecond laser waveguide inscription in silica glasses," *Optical Materials Express*, vol. 9, no. 12, pp. 4624–4633, 2019.

[110] R. M. Vazquez, R. Osellame, D. Nolli, C. Dongre, H. van den Vlekkert, R. Ramponi, M. Pollnau, and G. Cerullo, "Integration of femtosecond laser written optical waveguides in a lab-on-chip," *Lab on a Chip*, vol. 9, no. 1, pp. 91–96, 2009.

[111] J. W. Chan, T. R. Huser, S. Risbud, and D. Krol, "Modification of the fused silica glass network associated with waveguide fabrication using femtosecond laser pulses," *Applied Physics A*, vol. 76, pp. 367–372, 2003.

[112] R. Osellame, S. Taccheo, M. Marangoni, R. Ramponi, P. Laporta, D. Polli, S. De Silvestri, and G. Cerullo, "Femtosecond writing of active optical waveguides with astigmatically shaped beams," *JOSA B*, vol. 20, no. 7, pp. 1559–1567, 2003.

[113] K. Tung, W. Wong, and E. Pun, "Polymeric optical waveguides using direct ultraviolet photolithography process," *Applied Physics A*, vol. 80, pp. 621–626, 2005.

[114] S. Sowa, W. Watanabe, T. Tamaki, J. Nishii, and K. Itoh, "Symmetric waveguides in poly (methyl methacrylate) fabricated by femtosecond laser pulses," *Optics Express*, vol. 14, no. 1, pp. 291–297, 2006.

[115] G. D. Marshall, R. J. Williams, N. Jovanovic, M. Steel, and M. J. Withford, "Point-by-point written fiber-bragg gratings and their application in complex grating designs," *Optics Express*, vol. 18, no. 19, pp. 19844–19859, 2010.

[116] T. Guo, F. Liu, B.-O. Guan, and J. Albert, "Tilted fiber grating mechanical and biochemical sensors," *Optics & Laser Technology*, vol. 78, pp. 19–33, 2016.

[117] D. Tosi, "Review of chirped fiber bragg grating (cfbg) fiber-optic sensors and their applications," *Sensors*, vol. 18, no. 7, p. 2147, 2018.

[118] R. Wang, J. Si, T. Chen, L. Yan, H. Cao, X. Pham, and X. Hou, "Fabrication of high-temperature tilted fiber bragg gratings using a femtosecond laser," *Optics Express*, vol. 25, no. 20, pp. 23684–23689, 2017.

[119] I. Fanderlik, *Silica glass and its application.* Elsevier, 2013.

[120] J. Tomlinson, M. Heynes, and J. Bockris, "The structure of liquid silicates. part 2.—molar volumes and expansivities," *Transactions of the Faraday Society*, vol. 54, pp. 1822–1833, 1958.

[121] Y. Bellouard, A. A. Said, and P. Bado, "Integrating optics and micro-mechanics in a single substrate: a step toward monolithic integration in fused silica," *Optics Express*, vol. 13, no. 17, pp. 6635–6644, 2005.

[122] Y. Bellouard, A. A. Said, and P. Bado, "Integrating optics and micro-mechanics in a single substrate: a step toward monolithic integration in fused silica.," *Optics Express*, vol. 13, no. 17, pp. 6635–6644, 2005.

[123] B. Lenssen and Y. Bellouard, "Optically transparent glass micro-actuator fabricated by femtosecond laser exposure and chemical etching," *Applied Physics Letters*, vol. 101, no. 10, p. 103503, 2012.

[124] S. I. Nazir and Y. Bellouard, "Contactless optical packaging concept for laser to fiber coupling," *IEEE Transactions on Components, Packaging and Manufacturing Technology*, vol. 11, no. 6, pp. 1035–1043, 2021.

[125] S. I. Nazir, C. E. Athanasiou, and Y. Bellouard, "On the behavior of uniaxial static stress loaded micro-scale fused silica beams at room temperature," *Journal of Non-Crystalline Solids: X*, vol. 14, 2022.

[126] M. Zanaty, T. Fussinger, A. Rogg, A. Lovera, D. Lambelet, I. Vardi, T. J. Wolfensberger, C. Baur, and S. Henein, "Programmable multistable mechanisms for safe surgical puncturing," *Journal of Medical Devices*, vol. 13, no. 2, 2019.

[127] L. Tissot-Daguette, C. Baur, A. Bertholds, P. Llosas, and S. Henein, "Design and modelling of a compliant constant-force surgical tool for objective assessment of ossicular chain mobility," in *2021 21st International Conference on Solid-State Sensors, Actuators and Microsystems (Transducers)*, pp. 1299–1302, IEEE, 2021.

[128] D. Yao, P. Nagarajan, L. Li, and A. Y. Yi, "A two-station embossing process for rapid fabrication of surface microstructures on thermoplastic polymers," *Polymer Engineering & Science*, vol. 47, no. 4, pp. 530–539, 2007.

[129] C.-Y. Chang, S.-Y. Yang, L.-S. Huang, and K.-H. Hsieh, "Fabrication of polymer microlens arrays using capillary forming with a soft mold of micro-holes array and uv-curable polymer," *Optics Express*, vol. 14, no. 13, pp. 6253–6258, 2006.

[130] K. Kalli, C. Riziotis, A. Posporis, C. Markos, C. Koutsides, S. Ambran, A. S. Webb, C. Holmes, J. C. Gates, J. K. Sahu, *et al.*, "Flat fibre and femtosecond laser technology as a novel photonic integration platform for optofluidic based biosensing devices and lab-on-chip applications: Current results and future

perspectives," *Sensors and Actuators B: Chemical*, vol. 209, pp. 1030–1040, 2015.

[131] M. O'Keefe and L. Nolan, "Lasik surgery in children," *British journal of ophthalmology*, vol. 88, no. 1, pp. 19–21, 2004.

[132] D. Tulli, D. Janner, and V. Pruneri, "Room temperature direct bonding of linbo3 crystal layers and its application to high-voltage optical sensing," *Journal of Micromechanics and Microengineering*, vol. 21, no. 8, p. 085025, 2011.

[133] T. Young, "Iii. an essay on the cohesion of fluids," *Philosophical transactions of the royal society of London*, no. 95, pp. 65–87, 1805.

[134] A. Y. Vorobyev and C. Guo, "Femtosecond laser nanostructuring of metals," *Optics express*, vol. 14, no. 6, pp. 2164–2169, 2006.

[135] W. Barthlott and C. Neinhuis, "Purity of the sacred lotus, or escape from contamination in biological surfaces," *Planta*, vol. 202, pp. 1–8, 1997.

[136] W. Barthlott, M. Mail, and C. Neinhuis, "Superhydrophobic hierarchically structured surfaces in biology: evolution, structural principles and biomimetic applications," *Philosophical Transactions of the Royal Society A: Mathematical, Physical and Engineering Sciences*, vol. 374, no. 2073, p. 20160191, 2016.

[137] G. C. Righini and A. Chiappini, "Glass optical waveguides: a review of fabrication techniques," *Optical Engineering*, vol. 53, no. 7, p. 071819, 2014.

[138] S. Alberti and J. Jágerská, "Sol-gel thin film processing for integrated waveguide sensors," *Frontiers in Materials*, vol. 8, p. 629822, 2021.

[139] M. A. Butt, C. Tyszkiewicz, P. Karasiński, M. Zięba, A. Kaźmierczak, M. Zdończyk, Ł. Duda, M. Guzik, J. Olszewski, T. Martynkien, *et al.*, "Optical thin films fabrication techniques—towards a low-cost solution for the integrated photonic platform: A review of the current status," *Materials*, vol. 15, no. 13, p. 4591, 2022.

[140] A. M. Streltsov and N. F. Borrelli, "Study of femtosecond-laser-written waveguides in glasses," *JOSA B*, vol. 19, no. 10, pp. 2496–2504, 2002.

[141] J. Liu, Z. Zhang, S. Chang, C. Flueraru, and C. P. Grover, "Directly writing of 1-to-n optical waveguide power splitters in fused silica glass using a femtosecond laser," *Optics communications*, vol. 253, no. 4-6, pp. 315–319, 2005.

[142] J. Lapointe, *Fonctionnalisation des écrans de téléphones mobiles: des premiers dispositifs invisibles à l'amélioration de l'écriture par laser.* Ecole Polytechnique, Montreal (Canada), 2017.

[143] N. A. Issa, "High numerical aperture in multimode microstructured optical fibers," *Applied Optics*, vol. 43, no. 33, pp. 6191–6197, 2004.

[144] M. Tunon de Lara, L. Amez-Droz, K. Chah, P. Lambert, C. Collette, and C. Caucheteur, "Femtosecond pulse laser-engineered glass flexible structures

instrumented with an in-built bragg grating sensor.," *Optics Express*, vol. 31, no. 18, pp. 29730–29743, 2023.

[145] L. Amez-Droz, M. Tunon de Lara, C. Collette, C. Caucheteur, and P. Lambert, "Instrumented flexible glass structure: A bragg grating inscribed with femtosecond laser used as a bending sensor," *Sensors*, vol. 23, no. 19, p. 8018, 2023.

[146] D. W. Richerson and W. E. Lee, *Modern ceramic engineering: properties, processing, and use in design.* CRC press, 2018.

[147] L. C. Bank, *Composites for construction: structural design with FRP materials.* John Wiley & Sons, 2006.

[148] J. Xue, X. Wang, J. H. Jeong, and X. Yan, "Fabrication, photoluminescence and applications of quantum dots embedded glass ceramics," *Chemical Engineering Journal*, vol. 383, p. 123082, 2020.

[149] M. Sufian, S. Ullah, K. A. Ostrowski, A. Ahmad, A. Zia, K. Śliwa-Wieczorek, M. Siddiq, and A. A. Awan, "An experimental and empirical study on the use of waste marble powder in construction material," *Materials*, vol. 14, no. 14, p. 3829, 2021.